UNIVERSITY of CALIFORNIA
Santa Barbara

Phosphors for laser lighting applications: structural evolution, dense monoliths, and thermally stable composites

A Dissertation submitted in partial satisfaction of the

requirements for the degree

Doctor of Philosophy

in

Materials

by

Clayton Joseph Cozzan

Committee in charge:

Professor Ram Seshadri, Chair
Professor Stephen Wilson
Professor David Weld
Professor Stephen P. DenBaars
Professor Shuji Nakamura

September 2018

The dissertation of Clayton Joseph Cozzan is approved.

Professor Stephen Wilson

Professor David Weld

Professor Stephen P. DenBaars

Professor Shuji Nakamura

Professor Ram Seshadri, Committee Chair

June 2018

Phosphors for laser lighting applications: structural evolution, dense monoliths, and thermally stable composites

by

Clayton Joseph Cozzan

to my wife

Acknowledgments

I would first like to thank Ram Seshadri for welcoming me into his group and for the support and guidance over the years. Thanks also to my committee for their support. Stephen Wilson and David Weld have been extremely supportive and helpful, both pushing me to better understand the science at its most fundamental level, as well as offering guidance to help with a successful graduate career. Steven DenBaars and Shuji Nakamura have also been essential to my education. Their scientific accomplishments and hard work enable the partnerships that support and comprise the Solid State Lighting and Energy Electronics Center. This unique and world-class partnership gives all of the participating students the opportunity to perform fundamental research with direct commercial impact. Steve and Shuji have the special ability to see the potential and future of solid state lighting, and they play an enormous role in making this future a reality. I have been lucky to interact with them.

Ram has fostered a research group of collaborative and supportive students, enabling an environment where we can rely both on our advisor and each other for scientific guidance. I hope for the sake of graduate students everywhere that this is the norm, and I am deeply grateful for being a member of the Seshadri group. Ram can cater his mentoring style to each student, allowing

a diverse group of student researchers to thrive. It is in this way that Ram prioritizes our work, always having time and making time to meet with us. His depth of knowledge and insight in the field of materials science and materials chemistry (and almost any topic, scientific or otherwise), is truly enjoyable, and I always learn something new from our conversations and from his research talks. Thanks to his eclectic research interests, the group studies many different topics, which I think is one of the greatest assets to the collaborative environment. Thanks Ram for ensuring the success of all students by cultivating a climate of support instead of competition, which speaks both to the wealth of different topics explored by his students as well as the great people I have been lucky enough to work with these past few years. To this end, a special thanks to Kent Griffith from the University of Cambridge. I met Kent when he was visiting UCSB for a few weeks. Kent, with his expertise interpreting complex NMR data through computation, was immediately very interested in some experimental data collected earlier in my graduate work at UCSB on a class of materials known as SiAlONs. Thanks to his hard work and being very generous with his time, the project took a new direction that enhanced the depth and understanding of the chemistry of SiAlONs. The final project is detailed in Chapter 2 of the present dissertation.

This culture of support is a staple of the UCSB Materials Department, and

I owe great gratitude for the many researchers at UCSB conducting their work altruistically. A former UCSB graduate student told me that it is easy to do research here. That is not to say research itself is easy, but that the amazing staff and faculty supporting the myriad of labs and facilities make learning a new technique and performing new experiments within reach without bureaucracy. I would like to thank Amanda Strom for running our home lab and teaching me many techniques critical to my graduate work. I would also like to thank Deryck Stave for running the Materials Processing Lab, teaching me many new techniques, helping me establish equipment in different labs, and for being a friend. There are numerous other staff and students that make the facilities at UCSB truly world class, including Youli Li running the X-ray facilities, Alex Mikhailovsky for his expertise in the optical characterization facilities, and Jerry Hu running the NMR facilities with Jaya Nolt and Shamon Walker, that have helped my PhD experience move along as smoothly as it did. I would be remiss if I did not also thank Professors Jacob L. Jones, Scott Perry, and Jennifer Andrew for inspiring me to continue on this career path.

A large focus of the Materials Research Lab is outreach, and I would like to thank Dotti Pak, Julie Standish, Claudia Gutierrez-Mazzotti, and Frank Kinnaman for all that they do in support of educational outreach. Working with them has been an important and meaningful part of my own education,

and I am forever grateful. The MRL runs as well as it does thanks to Ram's leadership and the support of all the participating faculty and staff. I would like to thank Craig Hawker, Sara Bard, Rachel Behrens, Samantha Cardillo, Mike Craig, Mary McGuan, Sara Sorensen, and Sylvia Vogel for all that they do. Part of my work has been supported by the Solid State Lighting and Energy Electronics Center, and I would like to thank Claude Weisbuch, Dan Cohen, Daniel Beccera, Guillaume Lheureux, Caroline Reilly, and the rest of our team for teaching me about lasers and optics both directly and via osmosis. Additional thanks to Fukiko Miyazaki, Tara Owens, Yukina Warner, and Jocelyn Guzman for all their hard work behind the scenes to keep the department running smoothly. I have been lucky enough to get to know Dr. Tal Margalith over the years as well, and appreciate his role as both a mentor and a friend.

There are many reasons why working at the MRL has been enjoyable over the last few years. From meeting graduate students in student organizations in the building, to the waves in winter that grace Campus Point, Santa Barbara is truly a special place to go to school. The list of fellow graduate students to acknowledge is far too long, and for that, I am extremely lucky. Thanks to the students in GSDS, the people I have worked with in lab including Emily Levin, Dr. Geneva Laurita, Changmin Lee, my interns Courtney Schwartz, Marcus Cohen, Linus Halgund, Michael Brady, and Nick O'Dea, my fellow teaching

assistants, and my friends outside of work. Finally, a very special thank you to my family and my wife Margarita. Without their support, I would not be the person I am today.

This work was supported by a National Science Foundation Graduate Research Fellowship, the Solid State Lighting and Energy Electronics Center at UCSB, the Mitsubishi Chemical Center for Advanced Materials, and the Advanced Research Projects Agency-Energy. The MRL Shared Experimental Facilities are supported by the MRSEC Program of the NSF under Award No. DMR 1720256; a member of the NSF-funded Materials Research Facilities Network (www.mrfn.org).

Curriculum Vitae

Clayton Joseph Cozzan

Education

2014–2018 Ph.D. in Materials, University of California, Santa Barbara
Advisor: Professor Ram Seshadri

2010–2014 B.S. Materials Science and Engineering, University of Florida
Magna Cum Laude, Advisor: Professor Jennifer S. Andrew

Publications

12. C. Cozzan, G. Lheureaux, N. O'Dea, E. E. Levin, J. Graser, T. D. Sparks, S. Nakamura, S. P. DenBaars, C. Weisbuch, and R. Seshadri, Stable, heat conducting phosphor composites for high-power laser lighting, *ACS Applied Materials & Interfaces* **10** (2018) 5673–5681. [**doi**]

11. C. Cozzan, G. Laurita, M. W. Gaultois, M. Cohen, A. A. Mikhailovsky, M. Balasubramanian, and R. Seshadri, Understanding the links between composition, polyhedral distortion, and luminescence properties in green-emitting β-$Si_{6-z}Al_zO_zN_{8-z}$:Eu^{2+} phosphor, *Journal of Materials Chemistry C* **5** (2017) 10039–10046. [**doi**]

10. C. Lee, C. Shen, C. Cozzan, R. F. Farrell, J. S. Speck, S. Nakamura, B. S. Ooi, and S. P. DenBaars, Gigabit-per-second white light-based visible light

communication using near-ultraviolet laser diode and RGB phosphors, *Optics Express* **25** (2017) 17480–17487. [**doi**]

9. N. George, J. Brgoch, A. Pell, C. Cozzan, A. Jaffe, G. Dantelle, A. Llobet, G. Pintacuda, R. Seshadri, and B. Chmelka, Correlating local compositions and structures with the macroscopic optical properties of Ce^{3+}-doped $CaSc_2O_4$, an efficient green-emitting phosphor, *Chemistry of Materials* **29** (2017) 3538–3546. [**doi**]

8. C. Cozzan, K. J. Griffith, G. Laurita, J. G. Hu, C. P. Grey, and R. Seshadri, Structural evolution and atom clustering in β-SiAlON: β-$Si_{6-z}Al_zO_zN_{8-z}$, *Inorganic Chemistry* **54** (2017) 2153–2158. [**doi**]

7. C. Cozzan, M. J. Brady, N. O'Dea, E. E. Levin, S. Nakamura, S. P. DenBaars, and R. Seshadri, Monolithic translucent $BaMgAl_{10}O_{17}$:Eu^{2+} phosphors for laser-driven solid state lighting, *AIP Advances* **6** (2016) 105005. [**doi**]

6. E. Secret, C. Leonard, S. Kelly, A. Uhl, C. Cozzan, and J. Andrew, Size control of porous silicon-based nanoparticles via pore wall thinning, *Langmuir* **32** (2016) 1166–1170. [**doi**]

5. A. Birkel, N. A. DeCino, C. Cozzan, A. Mikhailovsky, B.-C. Hong, and R. Seshadri, A single-phase full-color phosphor based on $Ba_3MgSi_2O_{10}$

co-activated with Eu^{2+}, Tb^{3+}, and Mn^{2+}, *Solid State Sciences* **48** (2015) 82–89. [**doi**]

4. J. L. Jones, J. M. LeBeau, J. Nikkel, A. A. Oni, J. H. Dycus, C. Cozzan, F.-Y. Lin, A. Chernatynskiy, J. C. Nino, S. B. Sinnott, S. Mhin, G. L. Brennecka, and J. Ihlefeld, Combined experimental and computational methods reveal the evolution of buried interfaces during synthesis of ferroelectric thin films, *Advanced Materials Interfaces* **2** (2015) 1500181. [**doi**]

3. S. Mhin, K. Nittala, C. Cozzan, K. Kim, D. S. Robinson, L. M. Sanchez, R. G. Polcawich, and J. L. Jones, Role of the $PbTiO_3$ seed layer on the crystallization of PZT thin films, *Journal of the American Ceramic Society* **98** (2015) 1407–1412. [**doi**]

2. J. E. Daniels, C. Cozzan, S. Ukritnukun, G. Tutuncu, J. Andrieux, J. Glaum, C. Dosch, W. Jo, and J. L. Jones, Two-step polarization reversal in biased ferroelectrics, *Journal of Applied Physics* **115** (2014) 224104. [**doi**]

1. S. Mhin, C. Cozzan, K. Nittala, P. Wanninkhof, J. F. Ihlefeld, G. L. Brennecka, and J. L. Jones, Effect of switching atmospheric conditions during crystallization on the phase evolution of solution-derived lead zirconate titanate thin films, *Journal of the American Ceramic Society* **96**

(2013) 2706–2709. [**doi**]

Intellectual Property

2. C. Cozzan, S. P. DenBaars, and R. Seshadri, Monolithic translucent $BaMgAl_{10}O_{17}:Eu^{2+}$ phosphors for laser-driven solid state lighting, *patent pending*.

1. C. Cozzan, S. P. DenBaars, and R. Seshadri, Ce:YAG/Al_2O_3 composites for laser-excited solid-state white lighting, *patent pending*.

Abstract

Phosphors for laser lighting applications: structural evolution, dense monoliths, and thermally stable composites

by

Clayton Joseph Cozzan

Inorganic phosphor materials play a crucial role in the creation of white light from blue and near-UV solid-state sources, and understanding the intricacies of phosphor structure is key to set the stage for improved, more efficient functionality. The following dissertation begins with an introduction to the fundamentals of solid state lighting, phosphors, and a summary of some recent advances in the field. This is followed by a study to understand structural ordering in the framework of the commercial green-emitting phosphor material, β-$Si_{6-z}Al_zO_zN_{8-z}$, as a function of Al content. SiAlON ceramics, solid solutions based on the Si_3N_4 structure, are important, lightweight structural materials with intrinsically high strength, high hardness, and high thermal and chemical stability. Described by the chemical formula β-$Si_{6-z}Al_zO_zN_{8-z}$, from a compositional viewpoint, these materials can be regarded as solid solutions

between Si_3N_4 and Al_3O_3N. A key aspect of the structural evolution with increasing Al and O (z in the formula) is to understand how these elements are distributed on the β-Si_3N_4 framework. The average and local structure evolution of highly phase-pure samples of β-$Si_{6-z}Al_zO_zN_{8-z}$ with z = 0.050, 0.075, and 0.125 are studied using a combination of X-ray diffraction, nuclear magnetic resonance studies, and density functional theory calculations. Synchrotron X-ray diffraction establish sample purity and indicate subtle changes in average structure with increasing Al content in these compounds. ^{27}Al solid-state magic angle spinning nuclear magnetic resonance (NMR) experiments, coupled with detailed *ab initio* calculations of NMR spectra of Al in different AlO_qN_{4-q} tetrahedra ($0 \leq q \leq 4$), reveal a tendency of Al and O to cluster in these materials, more specifically, a high propensity for $AlON_3$ tetrahedral motifs to be distributed on the SiAlON framework. Independently, the calculations suggest an energetic preference for Al–O bond formation, instead of a random distribution, in the β-SiAlON system.

Next, an average structure and coordination environment analysis of the robust and efficient green-emitting phosphor, β-SiAlON:Eu^{2+} (β-$Si_{6-z}Al_zO_zN_{8-z}Eu_{0.009}$), is combined with a range of property measurements to elucidate the role of Al content (z) on luminescence properties, including the red shift of emission and the thermal quenching of luminescence as a

function of increasing Al content z. Average structure techniques reveal changes in polyhedral distortion with increasing z for the 9-coordinate Eu site in β-SiAlON:Eu^{2+}. X-ray absorption near edge structure (XANES) is used to confirm that the majority of the activator Eu is in the Eu^{2+} state, exhibiting the symmetry-allowed and efficient $4f^7 5d^0 \longrightarrow 4f^6 5d^1$ transitions. Room temperature and temperature-dependent luminescence indicate an curious increase in thermal stability with increasing z over a small range due to an increasing barrier for thermal ionization, which is correlated to an increase in the quantum yield of the phosphor. The works shows that specific emission properties can be targeted via compositional tuning, such as narrower emission β-SiAlON:Eu^{2+} (low z) for lower temperature operation, or maximum quantum yield and improved thermal stability (higher z up to 0.125) for high flux and/or high temperature operation.

With some fundamentals of phosphor structure-property relationships elucidated, we can now take steps to engineer these materials into useful morphologies. High power light emitting diodes (LEDs) and laser diodes (LDs) are being explored for white light generation and visible light communication, and thermally stable encapsulation schemes for color-converting inorganic phosphors are essential to their success. In the first example of thermally robust phosphors for laser-based lighting in the current thesis, the canonical

blue-emitting phosphor, high purity Eu-doped $BaMgAl_{10}O_{17}$ (BAM:Eu^{2+}), has been prepared using microwave-assisted heating (25 min) and densified into a ceramic phosphor using spark plasma sintering (30 min), resulting in translucent samples that emit blue light when incident with a UV laser diode. Results of the refinement on synchrotron X-ray diffraction data demonstrate the viability of microwave assisted heating for faster preparation of phase pure $BaMgAl_{10}O_{17}$:Eu^{2+}. The emission properties of the initial powder and the translucent sample have been studied using both a xenon lamp and a violet LD, and reveal the quantum yield of the starting powder does not change from densification into a translucent sample, and could likely be improved using optimized starting powders. Results indicate promise for uses of this blue phosphor in laser-based applications, as well as demonstrating a viable and fast way to prepare dense monolithic phosphors for laser light conversion.

As eluded to, a higher flux from high power LEDs and laser sources results in more conversion and therefore more conversion losses in the phosphor. This generates self-heating, surpassing the stability of current encapsulation strategies used for light-emitting diodes, usually based on silicones. Therefore, encapsulation-free phosphor ceramics are one solution to replace temperature limitations of resins and glasses and support the next generation of laser-based white lighting. In the next section of the dissertation, we again utilize spark

plasma sintering (SPS), this time for preparing ceramic phosphor composites of the canonical yellow-emitting phosphor Ce-doped yttrium aluminum garnet (Ce:YAG) combined with a chemically compatible and thermally stable oxide, α-Al_2O_3. SPS allows for compositional modulation and control of density. Phase fraction, microstructure, and luminescent properties of ceramic composites with varying compositions are studied here in detail. The relationship between density, thermal conductivity, and temperature rise during laser-driven phosphor conversion is elucidated, showing that only modest densities are required to mitigate thermal quenching in phosphor composites. Additionally, the scattering nature of the ceramic composites makes them ideal candidates for laser-driven white lighting in a reflection geometry, where Lambertian scattering of blue light offers great color uniformity. Furthermore, a luminous flux $>$1000 lumens is generated using a single commercial LD coupled to a single phosphor element. With increased light output, drastically lower operating temperatures, and white color points, these composites offer an advantage over the exemplary phosphor material alone. To ensure the widespread commercial adoption of these devices, warm white emitters must be developed by including some red or amber emission in a device, for example. This will be achieved through advances in lasers and phosphors, and some of the challenges and preliminary work conducted at UCSB will be discussed.

Finally, a brief comparison of single crystal emitters and phosphor powders is conducted to clarify the origin of thermal quenching in phosphors and to elucidate the difference between the intrinsic role of composition versus the ability to dissipate heat. The canonical yellow phosphor, Ce:YAG, has high thermal stability due to a high quenching temperature (>700 K) for low (<1% Ce) doping. In the present work, temperature dependent emission and photoluminescent lifetime measurements show nearly identical lifetime behavior from 77 K to 503 K for a single crystal and a powder derived from grinding the single crystal, reminding us that the thermal quenching temperature is primarily dictated by composition and not form. The results demonstrate the discrepancy between temperature dependent emission and lifetime measurements. In the present study, the quenching temperature of the Ce:YAG is observed to be a result of low activator doping regardless of whether it is in single crystal or powder in silicone form. The present results suggest that doping, which is an intrinsic materials property that dictates thermal quenching onset temperature and the intensity of emission for a given temperature, and thermal conductivity, which will dictate the operating temperature of the phosphor and is therefore an engineering consideration, must be understood for a given system. As seen presently, the phosphor in silicone and single crystal differ in thermal conductivity by two orders of magnitude, but display

nearly identical quenching behavior. With Ce:YAG single crystals being explored for transmission LD-based white lighting, the complex interplay between absorption, thermally conductivity, and the thermally quenching temperature, must be optimized.

Contents

List of Figures

List of Tables

Chapter 1

Introduction to phosphors for solid state lighting

1.1 Brief introduction to fundamental concepts

When light is absorbed in certain materials, the interaction of absorbed photons with electrons can promote electrons to higher energy states. These excited electrons will revert back to lower energy states by either emitting light or by dissipating heat. The process of emitting light from a high energy electron to a lower energy is called luminescence. If the electrons are excited by heat energy, such as for candles and incandescent light bulbs, the process is

known as thermoluminescence. The most energy-efficient lighting today utilizes a solid state semiconductor to generate light via electroluminescence, which is the emission of light resulting from an applied voltage or electric field.[1] By itself, these semiconductor light emitters radiate a single color, usually blue or violet, and must be either mixed or converted to other colors in a ratio that mixes to render white light. To convert the solid state light to other colors, inorganic phosphor materials are used. Phosphors exhibit photoluminescence, or the emission of lower energy light from absorption of higher energy photons, and they have reached ubiquity in solid-state lighting devices. The most optimized phosphors have high efficiencies, stable light emission with increasing temperature, and are much simpler to manufacture than the solid state emitters. In principle, the solid state source can be a light emitting diode (LED) or a laser diode (LD), and the differences in using one source over the other will be discussed as it is a central motivation of the current thesis. In order to understand the engineering requirements for phosphors under excitation by different light sources, we first need to understand the fundamentals of LEDs and LDs, how phosphors operate, and some fundamentals on quantifying color.

1.1.1 Physics of phosphors for light conversion

Phosphors are inorganic materials consisting of a host crystal structure with activator ions that undergo optical transitions doped into the host in small amounts, replacing atoms of similar size or sitting in a void of appropriate size.[2] The optical absorption and emission of a single dopant in a host is localized and is classified by the electronic transitions that can occur.[3] The current thesis will focus on host phosphors doped with activators undergoing the broad $4f^n \rightleftharpoons 4f^{n-1}5d$ transitions, where absorption occurs in the $4f^n$ state and visible light emission occurs from $4f^{n-1}5d^0$ transitions. This describes the two canonical dopant ions for solid-state lighting, Ce^{3+} (n=1) and Eu^{2+} (n=7), which both have broad band emission due to these *f-d* transitions.[2] For Ce^{3+}, energy transfer from $5d^1$ to the nearest level ($^2F_{7/2}$) is large enough that this transition emits light at an energy strongly dependent on the host crystal structure and the crystal field splitting of the $5d$ state.[2–4] With increasing crystal field strength that is largely dominated by electron-electron repulsion, emission bands shift to lower energies (longer wavelengths).[3]

1.1.2 Phosphor and color metrics

For measuring phosphor performance, the quantum yield (QY), or the number of photons emitted by the phosphor to the number of photons absorbed, is an important metric to know both at room temperature and as a function of temperature.[2] Phosphors for solid state lighting are down-conversion phosphors, meaning absorption occurs at a shorter wavelength of higher energy and emission at a longer wavelength of lower energy. This energy difference between the absorbed energy and the emitted energy is called the Stokes shift and is an inherent energy loss in all phosphors. Energy lost from both the Stokes shift and non-perfect quantum yield results in heat generation that can lead to lead to self heating to temperatures where thermal quenching of emission can occur.[5]

There are standardized measurements of color that will be referenced in the current work. The color points (x, y) of a phosphor or device can be defined in a CIE 1931 chromaticity diagram (Figure 1.1(a)), where monochromatic colors are located on the perimeter and colors become saturated in the middle near the white point (1/3, 1/3).[2] Another way to quantify color is the correlated color temperature (CCT, given in K) which relates color to the temperature of a black body as first derived by Planck in 1900.[6] CCT values are represented on

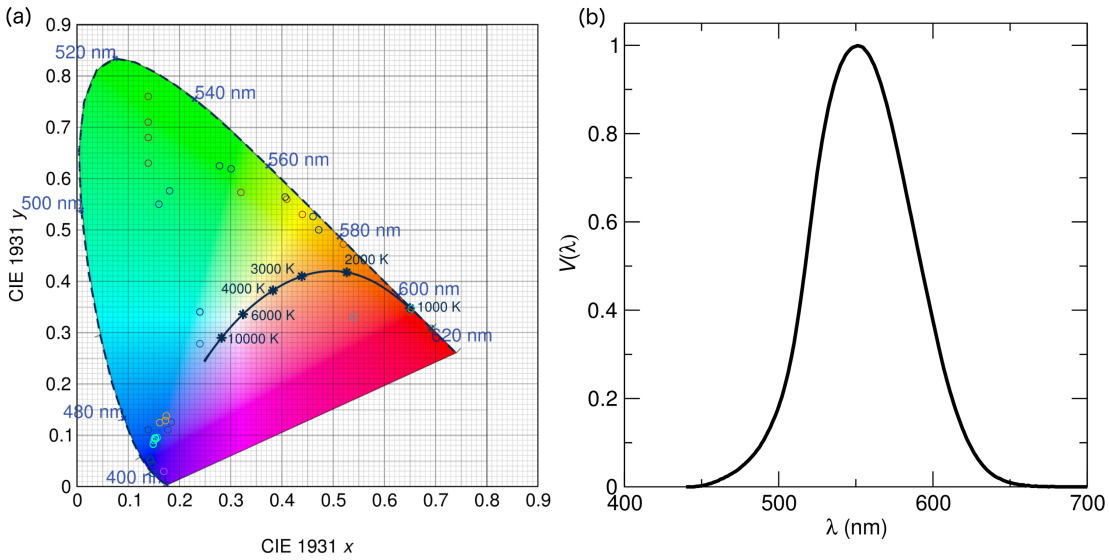

Figure 1.1: CIE 1931 diagram shows the swath of colors for canonical phosphors from the literature collected via a data-gathering exercise here at UCSB. Planckian locus shows CCT ranging from red to saturated white with the white point of (1/3, 1/3). Luminosity function shows that the human eye responds most sensitively to 555 nm light (b).

the CIE 1931 chromaticity diagram on a line called the Planckian locus.[7] For comparison, daylight is 6500 K and an incandescent source is typically around 2856 K.[6] Recent work elucidates the role and practical use of CCT in more detail.[8]

For measuring the amount of light output from a device, the luminous flux (Φ_{lum}) is the light power of a white light emitting device as perceived by the human eye, and is given as follows:

$$\Phi_{\mathrm{lum}} = 683 \frac{\mathrm{lum}}{\mathrm{W}} \int_{\lambda} V(\lambda) S(\lambda) d\lambda \tag{1.1}$$

where 683 lm/W is a normalization factor representing the maximum for monochromatic 555 nm light, $S(\lambda)$ is the power spectral distribution measured experimentally, and ($V(\lambda)$) is the eye response function which represents the intensity of color perception (shown in Figure 1.1(b)). The SI unit for luminous flux is the lumen (lm). The luminous efficacy is the ability of the radiation to produce visible light is calculated by dividing the flux by the eye response function, and the luminous efficiency is calculated by dividing the flux by the input power of the solid state emitter.[7] For comparison, compact bulbs and fluorescent light tubes have luminous efficiencies around 50 lm/W–80 lm/W.[6] High luminous efficiency values for LEDs have been achieved but with low

luminous flux and low input powers due to the thermal droop of LEDs at high carrier concentrations.[9] Laser-based lighting promises high luminous flux with high current densities.

1.1.3 Physics of light emitting diodes and laser diodes

Spontaneous light emission occurs in LEDs, which emit phase incoherent and polychromatic light in a wide range of angles. In LASERS (light amplification by stimulated emission of radiation), an excited electron can stimulate a different, excited electron to also revert back to a lower energy state that will then vibrate in phase with the first electron.[1] Stimulated emission therefore occurs when an incident beam forces electrons to add more photons to the same beam, which is accomplished using a device architecture known as a laser cavity with mirrors to aid and amplify the stimulated emission. The light emitted is highly monochromatic due to the very narrow difference in energy between the states and is highly collimated due to the very narrow physical window in which the light escapes. For a semiconductor laser, pumping of electrons to higher energy states occurs by direct injection of electrons and holes in the region with no mobile charge carriers (depletion layer) of this $p-n$ junction-based device. Lasers are much smaller than LEDs and can be further

miniaturized using multiple quantum wells, which is accomplished by placing a small band gap material between two larger gap materials, resulting in high potential barriers that confine particles. The results of such a geometry include a reduced threshold current density, a reduction in the number of carriers needed to establish more electrons residing in the higher energy state than the lower (population inversion), and increased amplification or gain. Lasers at low pumping current density emit spontaneously, just like LEDs, until the value reaches a threshold current density where population inversion can occur. Above this threshold, lasers operate much more efficiently than below threshold. Additionally, lasers can operate at current densities much higher than LEDs, enabling their exploration as high power light sources for solid state lighting.

1.1.4 Development of laser-based white lighting

Solid state lighting is rapidly replacing incandescent and fluorescent sources,[10] and advances in semi-polar and non-polar substrates for light emitting diodes (LEDs) have pushed current densities beyond 1000 A/cm^2.[11] Contrary to LEDs, laser diodes (LDs) operate under stimulated emission leading to quasi-monochromatic, highly directional, and coherent emission.[12] Moreover, when lasing, the carrier density is clamped at its threshold value,

meaning there is no droop at high current density in the same way that LEDs droop.[13] This results in peak efficiencies in LDs occurring for much higher current densities than LEDs. For example, power conversion efficiencies of state of the art blue LDs at threshold (4 kW/cm^2) greatly exceed that of LEDs (3 W/cm^2).[13] The development of a 417 nm InGaN multi-quantum well LD[14] kicked off research worldwide that has culminated in commercially available high power blue LDs,[13] with increases in both efficiency and power output being explored.[15–17]

For both LED and LD generated white light, inorganic phosphors are used to absorb the spectrally narrow solid state device excitation and emit a broader spectrum at longer wavelengths, allowing for color mixing to produce white light.[2] Two common strategies are utilized for white light generation. Either a blue LED or LD can be used in conjunction with a yellow-converting inorganic phosphor to generate a cool white light, or a near-UV/violet LED or LD can be used to excite blue, green, and red emitting inorganic phosphors to generate a warm white light.[2, 18] Despite improvements in monochromatic LEDs and LDs, inorganic phosphors will likely always be used in solid-state white lighting due to their well-known and understood high thermal stability of emission behavior, ease to manufacture,[19] low cost, and high efficiencies.[2] Drawbacks include the use of rare earth atoms[20] and lower efficiencies

at elevated temperatures for higher activator concentrations.[5] An all LED- or LD-based option however presents its own problems; arranging multiple emission color LEDs or LDs requires multiple drivers for each emitter, feedback control for color tuning,[9] and stable solid state emitters for all colors. Simpler and cheaper geometries can be obtained through the use of inorganic phosphors.

As stated above, both LEDs and LDs are being explored as viable options for phosphor-converted white light.[21, 22] LEDs emit diffuse light which requires that the phosphor powder be encapsulated, typically in silicone, and placed directly on the emitting device.[2] More power in LDs means more flux than LED-based systems,[9, 21] rendering phosphor in silicone inadequate due to the low thermal conductivity of silicone. Therefore, the high intensity light generated creates new engineering requirements for the color-converting phosphors used, which is a large focus in the present thesis. Any phosphor morphology used must have high enough thermal conductivity to dissipate heat generated from self-heating due to Stokes loss and QY losses, which can both quench the phosphor emission and carbonize the silicone typically used for phosphor encapsulation.[23] In recent years, many different strategies have been explored to replace silicone, which has a low thermally conductivity (0.18 W/(m·K)) and can turn from transparent to yellow or brown around typical operating temperatures of LEDs.[24–26] Phosphor-in-glass, a

strategy involving the mixture of phosphor powders with glass frit at low temperatures ($<$1000 °C), shows an order of magnitude increase in thermally conductivity (2.18 W/(m·K)), which is higher than the soda lime glass itself (0.97 W/(m·K)).[25] However, in use, it was reported that reflection losses of the excitation light led to a lower luminous efficacy than commercial white LEDs. The current dissertation will reference and study two promising phosphor candidates, single crystal emitters and dense ceramic monoliths, which both display high thermal conductivities and high quantum yields.

As discussed, the advantages of LD emitted light can be leveraged for generating white light at higher current densities and without droop. In 2002, Murota and colleagues demonstrated that with a YAG:Ce single crystal and a blue LD, the overlap integral of the emission and the eye response function showed a maximum luminous efficacy of 470 lm/W.[27] More recently, the company BMW has been utilizing laser-based high beam boosters to achieve the maximum tolerable visibility range as set by regulations (344 lm·m^2).[28] To have a point of comparison for some of the results shown in the present thesis, their LD-based headlight utilizes a 1 W–1.5 W blue laser with collimating/finite conjugate lenses as primary optics, coupled a fiber optic cable that runs the laser light to a heat sunk phosphor in reflection mode, and secondary optics to focus the light in the far-field. The headlight displays a total optical output of

741 lm at 25 °C (500 lm at 80 °C). These developments increased the distance of illumination of the farthest reaching light ray to 600 m, but to make further progress, BMW calls on further advances in fundamental research on blue LDs to increase laser efficiency and decrease cost.

1.2 Summary of progress on stable phosphors for high power lighting

1.2.1 Role of dopant concentration and thermal conductivity

Single crystals of Ce:YAG are being explored as a viable option for high power LED and LD generated light, with one of the first demonstrations in 2002.[27]. In this work, the authors explored the conversion efficiency limits of a YAG:Ce single crystal (0.05 at.%–0.10 at.%) with a blue LD, knowing that LDs would likely replace LEDs upon wide adoption of both technologies due to better coupling of the source and converter material when using LDs. More recent work studying single crystals (phase pure for 0.22 at.% Ce but polycrystalline for >0.5 at.%Ce) for white lighting has explored the color points and observed high emission intensity at elevated temperatures using LEDs.[24, 29, 30] The reason for the high emission intensity was attributed to the

thermal conductivity of the single crystal phosphor plate (9.2 W/(m·K) at room temperature and 5.6 W/(m·K) at 200 °C), which exceeded the 0.2 W/(m·K) (at room temperature) of typical organic resins typically used to encapsulate phosphors.[24] In separate work by the same group, the thermal quenching temperature of the crystals were measured using lifetime decay measurements, and a quenching temperature of 632 K was reported,[30] which agrees with previous work on Ce:YAG powders with very low doping amounts.[5] As thoroughly investigated by Bachmann *et. al.*, the amount of cerium dictates the quenching temperature in Ce:YAG powders.[5] It is likely that the thermal conductivity therefore has the secondary effect of managing phosphor heat from Stokes and quantum yield losses while in operation, which will be further discussed in the Appendix of the present dissertation. Therefore, the development of phosphors for LD light will depend on the inherent quenching behavior dictated firstly by the stoichiometry and secondly by the operating temperature, the later of which is determined by the thermal conductivity of the phosphor, the thermal resistance of the system, and the size of the material to name but a few considerations.

1.2.2 Dense ceramic phosphor composites

Dense ceramic phosphor composites are one way to eliminate binders, such as silicone, that have lower thermal conductivities than the phosphor. This approach also offers design flexibility, as phosphors of any dopant amount can be compressed into dense ceramics, and composites of multiple phosphors with heat dissipating materials, *e.g.*, oxides with high thermal conductivities, can be explored. When compared to phosphor in silicone, polycrystalline ceramics offer control of light scattering via pore size and density, reduce degradation and color angle shifts, can be characterized and binned before use with LEDs in a device, and offer better heat removal.[31] These ceramics can be both chip level and remote,[32] and the thickness can be altered to increase absorption.[5] Compared to phosphor powder in silicone or glass, phosphor ceramics allow for a lower operating temperature at a given device current, which results in high conversion efficiency and higher lumen output due to reduced thermal quenching. This also allows for higher power density without reaching a thermal quenching or degradation regime.[31]

Phosphor ceramics have been successfully utilized in industry. Philips/Lumileds trademarked Lumiramic polycrystalline ceramic tiles are made using a proprietary process involving heating under pressure to melt the

particles at the surface of the pellets, and the resulting ceramics are currently used for automotive forward lighting.[33] The QY of their Ce:YAG ceramic was reported as 96%, no saturation was observed up to 1.7 optical watts of LED irradiation, and a luminous flux of 300 lm at both 25° C and 150° C was reported, which demonstrates the thermal robustness of ceramic phosphors. The process was first disclosed in 2005 in a patent that includes discussion of Ce:YAG/Al_2O_3 composites, photonic structures to increase directionality, shaped phosphors to avoid total internal reflection, graded doping of the activator along the thickness of the sample, heat sinks, and claim processing of YAG, green-emitting phosphor ceramics based on $Lu_3Al_5O_{12}$, and red emitting $Sr_2Si_5N_8$:Eu^{2+} phosphor ceramics.[34] Published work by the same authors on these polycrystalline ceramic plates of Ce:YAG with a blue LED show a luminous efficacy of 326 lm/W, a CCT of 5500 K, and color points of (0.33, 0.35).[35]

It is also important to consider the atomic structure of the materials used in a ceramic phosphor, as they dictate the optical behavior of the material. Later work on Lumiramic™ preparation of triclinic $SrSi_2O_2N_2$:Eu^{2+} phosphors for fully-converted LEDs investigated the relationship between microstructure and optical properties.[36] It is important to know the crystal structure, as non-cubic crystals will be translucent because they are optically anisotropic and the refractive index will therefore change at grain boundaries, scattering both

incoming and converted light in phosphors. In Ce:YAG transparent ceramics, scattering can be introduced to overcome light trapping effects of the high index (n=1.84) Ce:YAG by controlling pore size and amount of pores.[36] In terms of the quantum yield, it is suggested that the grain size can be either large or very small to have highest possible transmittance, but larger crystallites provide the highest quantum yields.[36]

As mentioned in the Lumiramic^{TM} patent, one highly explored demonstration of phosphor composites has been the Ce:YAG/Al_2O_3 eutectic system. The first demonstration utilized the Y_2O_3/Al_2O_3 phase diagram by melting a mixture of Ce:YAG and Al_2O_3 at the eutectic composition and slow cooling from the melt.[37] This is possible because the Y_2O_3/Al_2O_3 phase diagram shows no phases between Al_2O_3 and $Y_3Al_5O_{12}$, therefore any mixture by weight can be explored without impurities. A more recent study of this system explored cylindrical and polished samples ranging in ratios by weight prepared using vacuum sintering (1700° C for 10 h), with the highest luminous efficiency of the phosphor excited by a blue LED was 93 lm/W for a 90 % Ce:YAG ($Y_{2.97}Ce_{0.03}Al_5O_{12}$) and 10 % Al_2O_3 sample (CCT = 4600 K).[38] The samples were then cut and polished down to 16 mm diameter discs with thicknesses ranging from 0.44 mm to 0.64 mm. It was hypothesized that the Al_2O_3 altered light propagation and extraction by introducing additional scattering, whereas

transparent samples waveguide light via total internal reflection. The more variable light propagation increased the extraction efficiency. Importantly to LD-based lighting, Al_2O_3 has a reported thermally conductivity of 33 W/(m·K) ±2,[39] and the thermal conductivity of composites prepared by Tang *et. al.* were not reported.

Ce:YAG/Al_2O_3 composites have also been explored explicitly for solid state laser lighting.[40] Spark plasma sintering (SPS) was used to prepare 60:40 Al_2O_3/Ce:YAG by weight (Ce content not specified) of very high relative density (99.7 %). This was achieved by heating the powder mixture at 300°C/min to 1360 °C with a 5 min soak under constant pressure of 80 MPa. The external QY of the phosphor before and after densification was reported as 75%-76%, and samples were polished to thicknesses between 0.1 mm and 0.6 mm to achieve translucent samples (55% light transmitted at 800 nm). The thermal conductivity of the 89.1% and 99.7% dense ceramic composite were 10.5 W/(m·K) and 18.5 W/(m·K) respectively, which is close to the 21.9 W/(m·K) calculated by the authors using a theoretical Maxwell model. When tested using a 445 nm blue laser diode (power density of 50 W/mm^2), the color points of the 0.40 mm thickness sample in reflection mode with the sample thermally attached to aluminum heat sink using thermal compound were closest to white, measuring (0.32, 0.32) with a CCT of 6270 K. From this

work it can be concluded that SPS can be used to prepare phosphor composite ceramics with higher thermal conductivities than single crystal phosphors with a quantum yield that is unchanged from powder to ceramic.[40] This also opens up the design space to more ratios by weight and to incorporate multiple phosphors. Future work in this area, some of which is explored in the present dissertation, should include *in situ* thermal management studies using infrared imagery, optimization of the Ce:YAG/Al_2O_3 ratio for optimum light output and thermal management, exploration of multiple phosphor composites, and designs of laser-based illumination fixtures incorporating this technology. These research directions offer a good starting point for the development of laser based lighting.

Chapter 2

Structural evolution and atom clustering in β-SiAlON: β-$Si_{6-z}Al_zO_zN_{8-z}$

SiAlON ceramics, solid solutions based on the Si_3N_4 structure, are important, lightweight structural materials with intrinsically high strength, high hardness, and high thermal and chemical stability. Described by the chemical formula β-$Si_{6-z}Al_zO_zN_{8-z}$, from a compositional viewpoint, these materials can be regarded as solid solutions between Si_3N_4 and Al_3O_3N. A key aspect of the

[1]The contents of this chapter have substantially appeared in Reference [41]: C. Cozzan, K. J. Griffith, G. Laurita, J. G. Hu, C. P. Grey, and R. Seshadri, Structural evolution and atom clustering in β-SiAlON: β-$Si_{6-z}Al_zO_zN_{8-z}$, *Inorg. Chem.* **54** (2017) 2153–2158.

structural evolution with increasing Al and O (z in the formula) is to understand how these elements are distributed on the β-Si_3N_4 framework. The average and local structure evolution of highly phase-pure samples of β-$Si_{6-z}Al_zO_zN_{8-z}$ with z = 0.050, 0.075, and 0.125 are studied here, using a combination of X-ray diffraction, nuclear magnetic resonance studies, and density functional theory calculations. Synchrotron X-ray diffraction establish sample purity and indicate subtle changes in average structure with increasing Al content in these compounds. ^{27}Al solid-state magic angle spinning nuclear magnetic resonance (NMR) experiments, coupled with detailed *ab initio* calculations of NMR spectra of Al in different AlO_qN_{4-q} tetrahedra ($0 \leq q \leq 4$), reveal a tendency of Al and O to cluster in these materials. Independently, the calculations suggest an energetic preference for Al–O bond formation, instead of a random distribution, in the β-SiAlON system.

In summary, this chapter will show how high-field ^{27}Al solid-state nuclear magnetic resonance (NMR) studies, coupled with density functional theory calculations of NMR parameters and energetics, suggest that even in samples of the β-SiAlON β-$Si_{6-z}Al_zO_zN_{8-z}$ with small values of z, that Al and O tend to cluster, with a high propensity for $AlON_3$ tetrahedral motifs to be distributed on the SiAlON framework.

2.1 Introduction

SiAlON ceramics can be regarded as solid solutions between the compositions Si_3N_4 and Al_3O_3N. These ceramics are useful for their excellent mechanical properties, such as high hardness, high strength, wear resistance, and resistance to thermal shock.[42] In these systems, Al is substituted for Si, and concomitantly, O for N. In SiAlONs, anion ordering is driven by differences in bonding, size, and charge, and the resultant clustering can have large effects on the behavior of optical SiAlONs.[43] To understand anion ordering in SiAlONs, local structure techniques must be utilized. X-ray diffraction is not sufficient, as the scattering factors of both Si and Al, and O and N are too similar, preventing precise occupancy information from being obtained. Extended X-ray absorption fine structure (EXAFS) suffers the same issues of contrast and is difficult to implement when substituent concentrations are low. The neutron pair distribution function technique could cast light on the problem, but once again, this technique would be limited in utility and scope at the low concentrations of Al and O considered here. Solid-state magic angle spinning nuclear magnetic resonance (MAS NMR) of ^{27}Al offers a potential solution, providing insight into the local coordination environment of the aluminum nucleus.

Early structural investigation of $Si_{6-z}Al_zO_zN_{8-z}$ using MAS NMR observed that ^{27}Al is a sensitive nucleus to coordination and geometry, whereas ^{29}Si is not, with spectra showing Si tetrahedrally coordinated in SiAlON that does not change with increased Al and O substitution.[44, 45] Investigations of SiAlONs using ^{27}Al MAS NMR revealed that rather than a random distribution of Si and Al on metal sites and O and N on non-metal sites or a preference for Al-N and Si-O bonds, there is a preference for Al–O and Si–N bonds.[45–47] This preference has also been verified using Monte Carlo simulations and neutron diffraction on other SiAlON systems.[48] Most early NMR studies suggested the existence of mixed tetrahedra,[49] which was supported by EXAFS showing a decrease of the average bond length for the first coordination sphere of Si with increasing Al and O.[45]

Broadening is observed in ^{27}Al MAS NMR spectra, and is associated with distorted tetrahedra from a range of AlO_qN_{4-q} $(0 \leq q \leq 4)$. It was proposed that the distribution changes with decreasing Al as more of the mixed AlO_3N and AlO_2N_2 are present, which are broader, and the AlN_4 peak intensity decreases with increasing Al due to AlO_3N and AlO_2N_2 formation.[47]. As the composition of SiAlON approaches AlN, the proportion of AlN_4 tetrahedra increases relative to $AlON_3$ tetrahedra.[49, 50] Conversely, in the formula $Si_{3-z}Al_zO_zN_{4-z}$ for $z \approx 0.5$ to 1, it was observed that substitutional O is strictly coupled to $Al(O,N)_4$

tetrahedra with a range of tetrahedral coordinations.[46] These early NMR works observed changes in lineshape as a function of Al–O content, but could not resolve them into distinct coordination environments due to the moderate fields used. More recently, work using X-ray absorption near edge spectroscopy (XANES) and computation showed evidence for Al–O bonds in SiAlON, with pairing of Al and O having an energy benefit of a few tenths of an eV per Al–O pair.[51]

Here, samples of β-$Si_{6-z}Al_zO_zN_{8-z}$ with systematically varying Al content ($z = 0.050$, $z = 0.075$, and $z = 0.125$) are studied. Synchrotron X-ray diffraction was utilized to investigate average structure changes in this system as a function of systematic variation in Al content. Synchrotron X-ray diffraction and prior neutron scattering work on the same samples (to establish composition) confirm phase purity, as well as demonstrate that the actual composition is the nominal composition.[52] *Ab initio* periodic density-functional theory (DFT) based calculations of NMR parameters and structural energetics, along with high-field ^{27}Al MAS NMR measurements were employed to elucidate local structure details of the Al site in the SiAlON structure. Improvements in NMR hardware, coupled with quantum calculations, have enabled the identification and quantification of the aluminum coordination environments. Simulations of quadrupolar NMR lineshapes highlight the inherent inability of previous

moderate field studies to resolve any but the highly symmetric AlO_4/AlN_4 sites. Clustering of Al and O in the SiAlON structure is observed experimentally and is supported independently by DFT enthalpies and comparison of calculated Al environments to experimental spectra collected in the current work. The current work is therefore the first high field NMR study of completely phase pure β-$Si_{6-z}Al_zO_zN_{8-z}$, and is also the first time DFT calculations have been employed to to assign spectra and determine energetics in these systems.

Besides helping to understand the distribution of Al and O in β-SiAlON phases, the present work points to the general utility of employing high-resolution, high-field NMR techniques, in appropriate combination with DFT calculations to unravel the intricate details of local compositional variation in functional materials. Studies such as these could profit a variety of functional material classes where small amounts of dopants are known to have important effects. These include zeolites,[53] phosphors,[52, 54] diluted magnetic semiconductors,[55] and thermoelectric materials.[56]

2.2 Methods

To obtain accurate control over the concentration of Al^{3+} and O^{2-}, a high-pressure and high-temperature synthesis route was used. Powders of

α-Si_3N_4 and Al_2O_3 were ground with nominal stoichiometry $Si_{6-z}Al_zO_zN_{8-z}$ in an alumina pestle. The powders were heated in a boron nitride crucible at 1950 °C for 12 h under N_2 (>99.9995%) at a pressure of 0.92 MPa and annealed in argon for 8 h before being ground into a fine powder and washed using a mixture of HNO_3 and HF.

Synchrotron X-ray powder diffraction was performed at room temperature at the 11-BM beamline at the Advanced Photon Source, Argonne National Laboratory. The calibrated wavelength was $\lambda = 0.459001$ Å for $z = 0.075$ and $\lambda = 0.413194$ Å for $z = 0.050$ and $z = 0.125$. Rietveld refinements were performed using the General Structure Analysis System (GSAS) with EXPGUI.[57, 58] Peak shapes were handled using the pseudo-Voigt profile function, which combines Gaussian and Lorentzian components. The background was handled using a Chebyshev polynomial. The occupancies were left as nominal due to the lack of contrast of scattering between Al and Si and between O and N. The refined structures were visualized using the open-source crystallographic software VESTA.[59]

Solid-state ^{27}Al NMR was conducted at room temperature using a Bruker AVANCE III Ultrashield Plus 800 MHz (18.8 T) narrow bore (54 mm) spectrometer with a 3.2 mm Tri-Gamma HXY triple resonance MAS probe with a transmitter frequency of 208.52 MHz for the 100% naturally abundant ^{27}Al

nuclei. Samples were packed into a 3.2 mm zirconia rotor (Bruker) and spun at 20 kHz for 24 h of data collection due to low Al content. The radio frequency (RF) pulse length (3.6 μs) and power (117.5 W) were chosen to achieve a 15 degree pulse ($\pi/12$) rotation of the net ^{27}Al magnetization for quantitative measurements. Shifts were referenced to 1 M $Al(NO_3)_{3(aq.)}$ at 0 ppm. The resonance frequency for nuclei with non-zero nuclear quadrupolar coupling constants (NQCC, C_Q) is influenced by electronic shielding as well as a quadrupolar term, thus it is correct to refer to shifts, rather than chemical shifts, for quadrupolar nuclei such as ^{27}Al. Data treatment was performed using the SOLA interface in Topspin 3.2. Simulations were performed on the central ($+1/2 \leftrightarrow -1/2$) and satellite transitions ($\pm 1/2 \leftrightarrow 3/2$ and $\pm 3/2 \leftrightarrow 5/2$) with second-order perturbation theory treatment of the quadrupolar interaction. *Ab initio* DFT calculations of enthalpy and NMR parameters were performed in the CASTEP plane-wave code.[60–63] The Perdew–Burke–Ernzerhof (PBE)[64] exchange-correlation functional, a generalized gradient approximation (GGA) functional, was employed. Core electrons were approximated with Vanderbilt "ultrasoft" pseudopotentials generated "on-the-fly" in CASTEP 8.0. The SiAlON system required a basis set of plane waves with energies up to 600 eV and a Monkhorst–Pack[65] grid corresponding to a Brillouin zone sampling finer than $2\pi \times$ 0.05 Å^{-1}. Convergence with respect to the basis set energy and

Brillouin zone sampling was confirmed. Under these conditions, enthalpy, σ_{iso}, and C_Q were converged to within 0.1 eV, 0.1 ppm, and 0.1 MHz, respectively. The reference equation used to convert shielding to shift was determined via linear regression from a series of Al-compounds and is detailed in the following paragraph. Numerical simulations of the quadrupolar NMR lineshapes were performed from the *ab initio* ^{27}Al NMR tensors in the SIMPSON[66] program at 18.8 T and 20 kHz MAS to compare with the spectra collected in this study. The effect of unit cell size in the calculations was evaluated by comparing calculations with the lattice parameters fixed at the values determined from synchrotron diffraction for $z = 0.050$, $z = 0.075$, and $z = 0.125$ as well as when the cell was allowed to relax from the initial values for $z = 0.075$.

The mathematical explanation behind the stochastic model is as follows. The number of configurations *(n.o.c.)* of a given coordination type α *e.g.*, $AlON_3$ is as follows:

$$n.o.c._{\alpha} = \frac{(a+b)!}{(a!)(b!)} \tag{2.1}$$

where a is the number of species *A* in coordination shell *e.g.*, 1 O, and *b* is the number of species *B* in coordination shell *e.g.*, 3 N. Using *n. o. c.*$_{\alpha}$, the probability of that given coordination type (p_{α}) can be calculated as follows:

Table 2.1: Stochastic coordination model for a tetrahedral ion with two coordinating species. The statistical probability for each AlO_qN_{4-q} site is calculated for various dopant concentration in $Si_{6-z}Al_zO_zN_{8-z}$. At the defect concentrations in this study, $z = 0.05$, $z = 0.075$, and $z = 0.125$, a random distribution of atoms would yield AlN_4 tetrahedra with a minor presence of $AlON_3$.

Config.	O	n	$n.o.c.$	$p_{0.050}$ %	$p_{0.075}$ %	$p_{0.125}$ %	$p_{0.50}$ %	p_1 %	p_2 %	p_4 %
AlN_4	0	4	1	97.5	96.3	93.9	77.2	58.6	31.6	6.3
$AlON_3$	1	3	4	2.5	3.6	6	20.6	33.5	42.2	25
AlO_2N_2	2	2	6	0	0.1	0.1	2.1	7.2	21.1	37.5
AlO_3N	3	1	4	0	0	0	0.1	0.7	4.7	25
AlO_4	4	0	1	0	0	0	0	0	0.4	6.3

$$p_\alpha = n.o.c._\alpha([A]^a \cdot [B]^b) \tag{2.2}$$

where [*A*] is the concentration of species *A* *e.g.*, 0.05/8 = 0.00625 and [*B*] is the concentration of species *B* *e.g.*, 7.95/8 = 0.99375. The total probability of all sites

$$p_{\text{total}} = p_\alpha + p_\beta + p_{...} = 1 \tag{2.3}$$

and the sum of all concentrations

$$[A] + [B] + [...] = 1 \tag{2.4}$$

must equal one. The results of the stochastic model for the current work, a tetrahedral ion with two coordination species, are detailed in Table 2.1, with $p_{0.050}$, $p_{0.075}$, and $p_{0.125}$ corresponding to the experimentally observed doping concentrations, $z = 0.050$, $z = 0.075$, and $z = 0.125$, respectively.

In addition to statistical probabilities, energetics for specific dopant amounts were also explored. Table 2.2 provides energy values for defects greater that that measured experimentally, which continues to show energetic preference for $AlON_3$ coordination.

Table 2.2: Defect energies corresponding to Al contents greater than what is investigated experimentally. Energy preference is normalized by the least favorable configuration. Data for 6Al-6O with six AlN_4 and 8 Al-8O with eight AlN_4 are not shown as they did not converge.

Composition	Site (O on N1 or N2)	Energy/enthalpy (eV)	Energy preference (eV/formula unit)
3Al-3O	AlN_4, AlN_4, AlN_4	-26313.26	0
3Al-3O (adjacent tetrahedra)	$AlON_3$ (N1), $AlON_3$ (N2), $AlON_3$ (N1)	-26315.87	-2.61
3Al-3O (isolated tetrahedra)	$AlON_3$ (N1), $AlON_3$ (N2), $AlON_3$ (N1)	-26316.06	-2.8
3Al-3O	AlO_3N (N1, N1, N2), AlN_4, $AlON_3$ (N2)	-26315.98	-2.72
3Al-3O (adjacent tetrahedra)	AlO_3N (N1, N1, N2), AlN_4, AlN_4	-26315.08	-1.82
3Al-3O (isolated tetrahedra)	AlO_3N (N1, N1, N1), AlN_4, AlN_4	-26314.76	-1.5
4Al-4O	AlN_4, AlN_4, AlN_4, AlN_4	-26415.56	0
4Al-4O	AlO_2N_2 (N1, N1), $AlON_3$ (N2), AlO_2N_2 (N1, N1), $AlON_3$ (N1)	-26420.38	-4.81
4Al-4O	$AlON_3$ (N2), AlN_4, AlO_2N_2 (N1, N1), $AlON_3$ (N1)	-26418.88	-3.31
4Al-4O	AlN_4, AlO4 (N1, N1, N1, N2), $AlON_3$ (N1), AlN_4	-26419.11	-3.55
4Al-4O	$AlON_3$ (N1), AlN_4, AlO_3N (N1, N1, N2), $AlON_3$ (N1)	-26419.9	-4.34
4Al-4O	$AlON_3$ (N1), AlN_4, AlO_3N (N1, N1, N1), AlO_2N_2 (N1, N1)	-26420.23	-4.66
6Al-6O (adjacent tetrahedra)	AlO_2N_2 (N1, N1), $AlON_3$ (N2), $AlON_3$ (N1), AlO_2N_2 (N1, N1), $AlON_3$ (N1), $AlON_3$ (N1)	-26628.07	-0.37
6Al-6O (isolated tetrahedra)	AlO_2N_2 (N1, N1), $AlON_3$ (N2), $AlON_3$ (N1), $AlON_3$ (N2), AlO_2N_2 (N1, N1), $AlON_3$ (N1)	-26627.7	0
8Al-8O	AlO_2N_2 (N1, N1), $AlON_3$ (N2), $AlON_3$ (N1), AlO_2N_2 (N1, N1), AlO_3N (N1, N1, N2), AlO_2N_2 (N1, N1), $AlON_3$ (N1), AlN_4	-26835.87	-0.34
8Al-8O	AlO_2N_2 (N1, N1), $AlON_3$ (N2), $AlON_3$ (N1), $AlON_3$ (N1), AlO_2N_2 (N1, N2), AlO_2N_2 (N1, N1), $AlON_3$ (N1), $AlON_3$ (N1)	-26835.52	0

2.3 Results and discussion

β-$Si_{6-z}Al_zO_zN_{8-z}$ consists of densely packed, corner sharing $(Si,Al)(O,N)_4$ tetrahedra with ABAB stacking[46] and crystallizes in the hexagonal space group $P6_3$ (no. 173) with a channel along the c-axis.[52, 67, 68] Rietveld refinements of synchrotron X-ray data indicate phase purity in the β-SiAlON samples. Figure 2.1 shows the room temperature fit and refined structure for $z = 0.075$, with detailed structural refinements of atomic positions and refined atomic displacement parameters (U_{iso}) for all samples shown in Table 2.3.

Small atomic displacement parameters are linked to high structural rigidity.[52, 69] In the present work, the thermal displacement parameters are small, and therefore the rigidity does not change much with small substitution levels. It can be seen that the U_{iso} values for $z = 0.075$ are lowest, but X-ray scattering factors of O and N are too similar, there are not significant differences in any of the U_{iso} values that dictate a clear trend, and differences are in some cases within standard deviation of the refinement. In general, all samples have small atomic displacement parameters, which indicate that the rigidity of the structure is not reduced at small Al substitution levels. Also observed with increasing Al content is the increase in unit cell parameters both in the a and c direction, which leads to an overall increase in the unit cell volume.[46] An

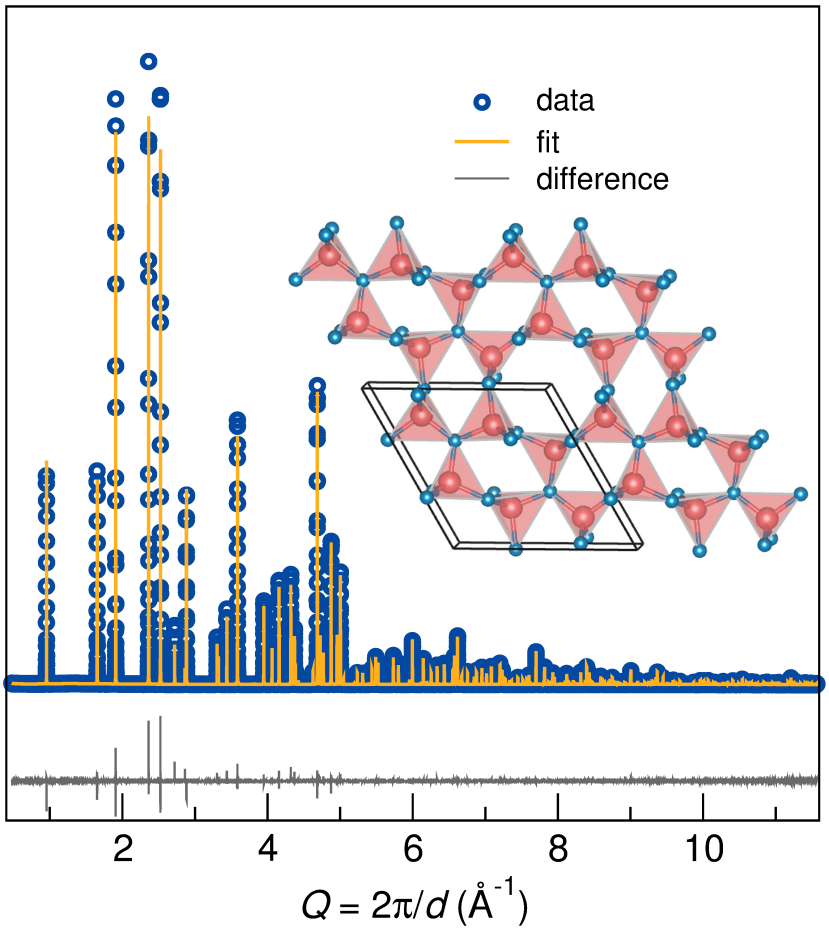

Figure 2.1: Synchrotron X-ray diffraction data (blue circles), refinement (fit, orange), difference between data and fit (gray line), and refined structure as inset, for β-$Si_{6-z}Al_zO_zN_{8-z}$ with $z = 0.075$. © 2017 American Chemical Society.

Table 2.3: Structural data obtained from Rietveld refinements of X-ray synchrotron diffraction data for β-$Si_{6-z}Al_zO_zN_{8-z}$ with $z = 0.075$. Numbers in parentheses show standard deviation on the last number. O1 and N1 are located on the 6c Wyckoff site and O2 and N2 are located on the 2b Wyckoff site in the unit cell.

Al content (z)	0.050	0.075	0.125
Cell a (Å)	7.60584(1)	7.60692(2)	7.60853(2)
Cell c (Å)	2.908444(7)	2.909039(7)	2.910116(7)
Cell V (Å^3)	145.7090(4)	145.7800(5)	145.8960(5)
Si/Al x	0.7685(5)	0.7685(4)	0.7685(2)
Si/Al y	0.1747(5)	0.1747(4)	0.1744(2)
Si/Al z	0.291(5)	0.250(3)	0.290(5)
O1/N1 x	0.0298(4)	0.0296(3)	0.0296(4)
O1/N1 y	0.3292(4)	0.3298(3)	0.3296(5)
O1/N1 z	0.303(4)	0.2670(3)	0.6975(4)
O2/N2 z	0.281(7)	0.238(6)	0.28(5)
Si/Al U_{iso} (Å^2)	0.0030(2)	0.0022(5)	0.0035(2)
O1/N1 U_{iso} (Å^2)	0.0031(4)	0.0023(4)	0.0039(6)
O2/N2 U_{iso} (Å^2)	0.0026(9)	0.0006(8)	0.0022(5)

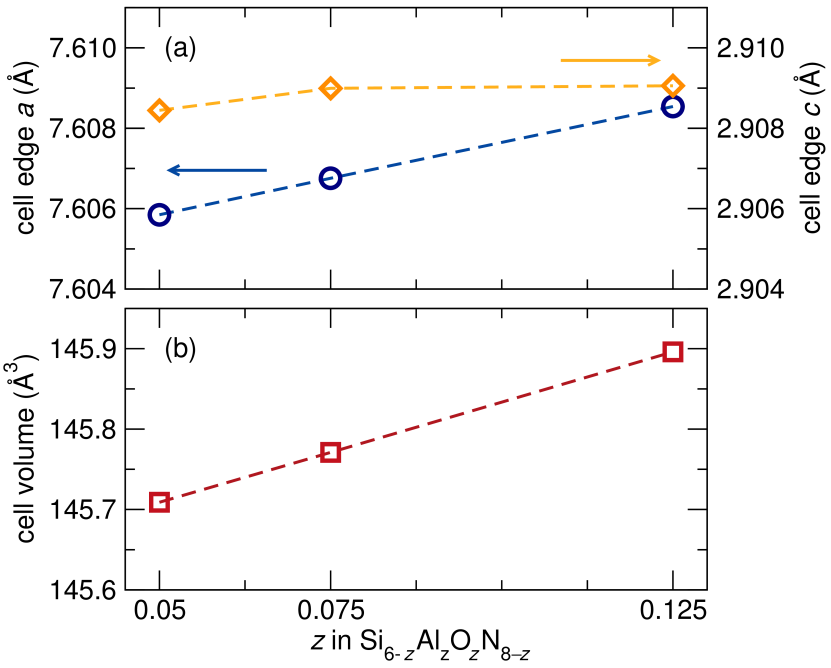

Figure 2.2: (a) Unit cell edges and (b) volume as a function of z determined through synchrotron X-ray diffraction show an increase in all parameters with z. Error bars are contained within the data points. © 2017 American Chemical Society.

ionic radii argument can explain this expansion, as Al^{3+} has a larger radius than Si^{4+} (0.39 Å and 0.26 Å for coordination number CN = 4, respectively).[70] This also involves incorporating O^{2-} to charge balance, which is smaller than N, and therefore would compete with the expansion.

Lattice parameters shown in Table 2.3 highlight the increase in unit cell volume with increasing Al content (visualized in Figure 2.2a). While an increase

in the unit cell volume does not guarantee an increase in these bond distances, the average bond length around this site increases from 2.6698 Å in $z = 0.050$ to 2.6877 Å in $z = 0.125$.

Si_3N_4 crystallizes in a unit cell with six silicon atoms and eight nitrogen atoms (Z = 2). For *ab initio* calculations, in order to study representative Al and O substitution levels, $2\times 2\times 2$ (48 Si/64 N, example defect structures shown in Figure 2.3) and $2\times 2\times 4$ (96 Si/128 N) supercells were created with Al–O pairs swapped into the new cells, representing $z = 0.0625$ for one Al–O pair in the former supercell, to $z = 1$ for eight Al–O pairs in the later supercell in $Si_{6-z}Al_zO_zN_{8-z}$. For calculations of the defect energetics, unit cell parameters were fixed to the experimental values found in this study for the intermediate Al content ($z = 0.075$) and atomic coordinates relaxed to local minima with DFT forces. Bond lengths obtained from diffraction and DFT show that for Si_3N_4, the Si–N bond lengths range from 1.70 Å to 1.77 Å. In low-Al SiAlONs, the Si–N bond lengths show very slight contraction, with bond lengths ranging from 1.68 Å to 1.76 Å. Si–O (1.74 Å to 1.77 Å), Al–N (1.77 Å to 1.83 Å), and Al–O (1.82 Å to 1.88 Å) bond ranges obtained from DFT confirm that Al forms longer bonds than Si, and O forms longer bonds than N; all of which supports the observation of unit cell expansion with increasing z obtained from Rietveld refinements of the diffraction data.

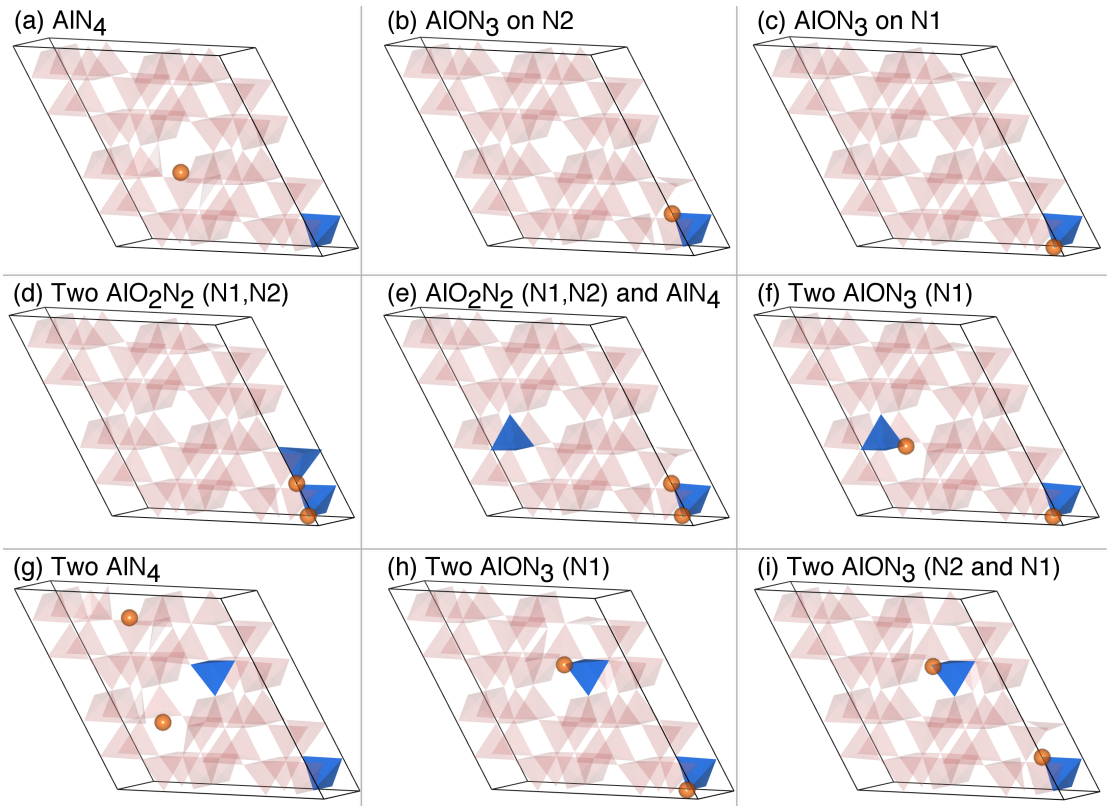

Figure 2.3: Defect structures for $2 \times 2 \times 2$ supercells with composition $Si_{48-x}Al_xN_{64-x}O_x$, where x=1 for (a)–(c) and x=2 for (d)–(i), are shown. Si–N tetrahedra are red, Al tetrahedra are blue, and oxygen atoms are orange and exaggerated in size for visibility. The defects follow the order of Table 2.5 and correspond to (a) AlN_4, (b) $AlON_3$ on the N2 site, (c) $AlON_3$ on the N1 site, (d) AlO_2N_2 (N1, N2) and AlO_2N_2 (N1, N2), (e) AlO_2N_2 (N1, N2) and AlN_4, (f) $AlON_3$ (N1) and $AlON_3$ (N1), (g) AlN_4 and AlN_4, (h) $AlON_3$ (N1) and $AlON_3$ (N1), and (i) $AlON_3$ (N2) and $AlON_3$ (N1). The anions O1 and N1 are located on the 6c Wyckoff site and O2 and N2 are located on the 2b Wyckoff site in the supercell.

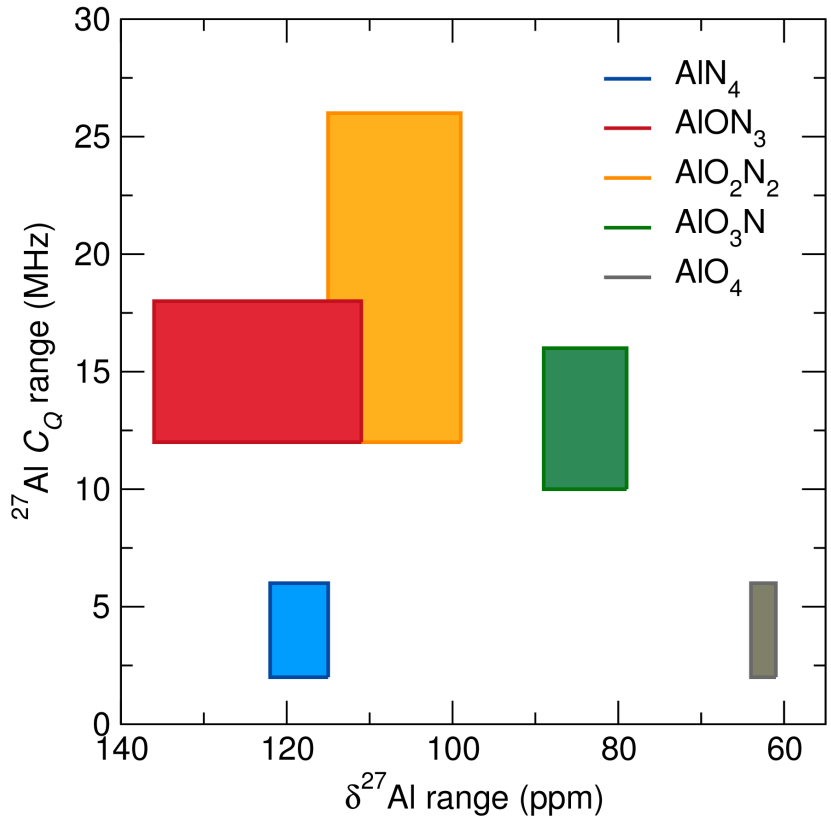

Figure 2.4: Calculated ranges for ^{27}Al C_Q (MHz) and δ (ppm) for various tetrahedral environments. © 2017 American Chemical Society.

Table 2.4: NMR parameters for fits from Figure 2.5 as informed by DFT calculations. Numbers in parentheses show uncertainties.

Site	AlN_4	$AlON_3$	$AlON_3$	AlO_2N_2/AlO_3N
δ^{27}Al shift (ppm)	108(1)	113(5)	116(5)	96(5)
C_Q (MHz)	3.4(0.5)	11.0(0.5)	12.8(0.5)	13.2(0.5)
η_Q	0.50(0.10)	0.80(0.10)	0.90(0.10)	0.40(0.10)

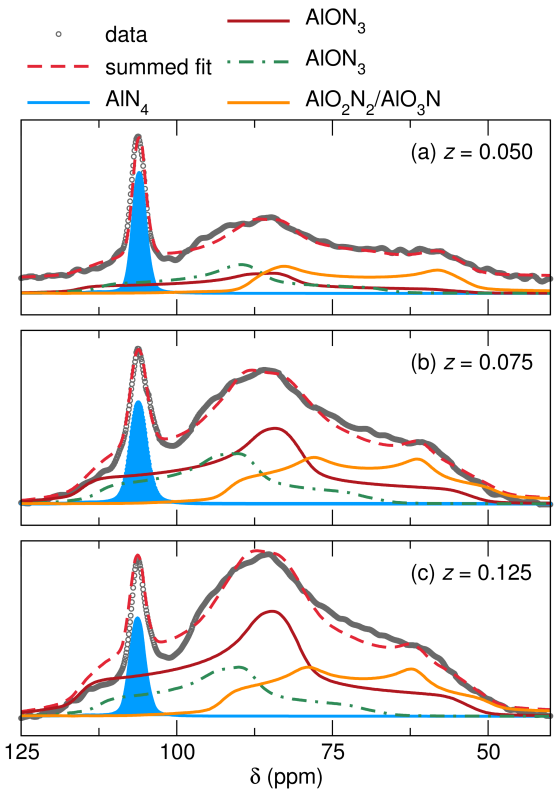

Figure 2.5: ^{27}Al NMR spectra at 18.8 T and 20 kHz MAS for (a) $z = 0.050$, (b) $z = 0.075$, and (c) $z = 0.125$ demonstrate the increase in the contribution from $AlON_3$ as a function of increasing Al. The experimental data (gray circles) are overlaid by the summed fit (red dashed line), which is comprised of an AlN_4 defect (blue line), two different $AlON_3$ environments (maroon and light green line), and AlO_2N_2/AlO_3N (orange line). Fit contributions are separated from data for clarity in (a). © 2017 American Chemical Society.

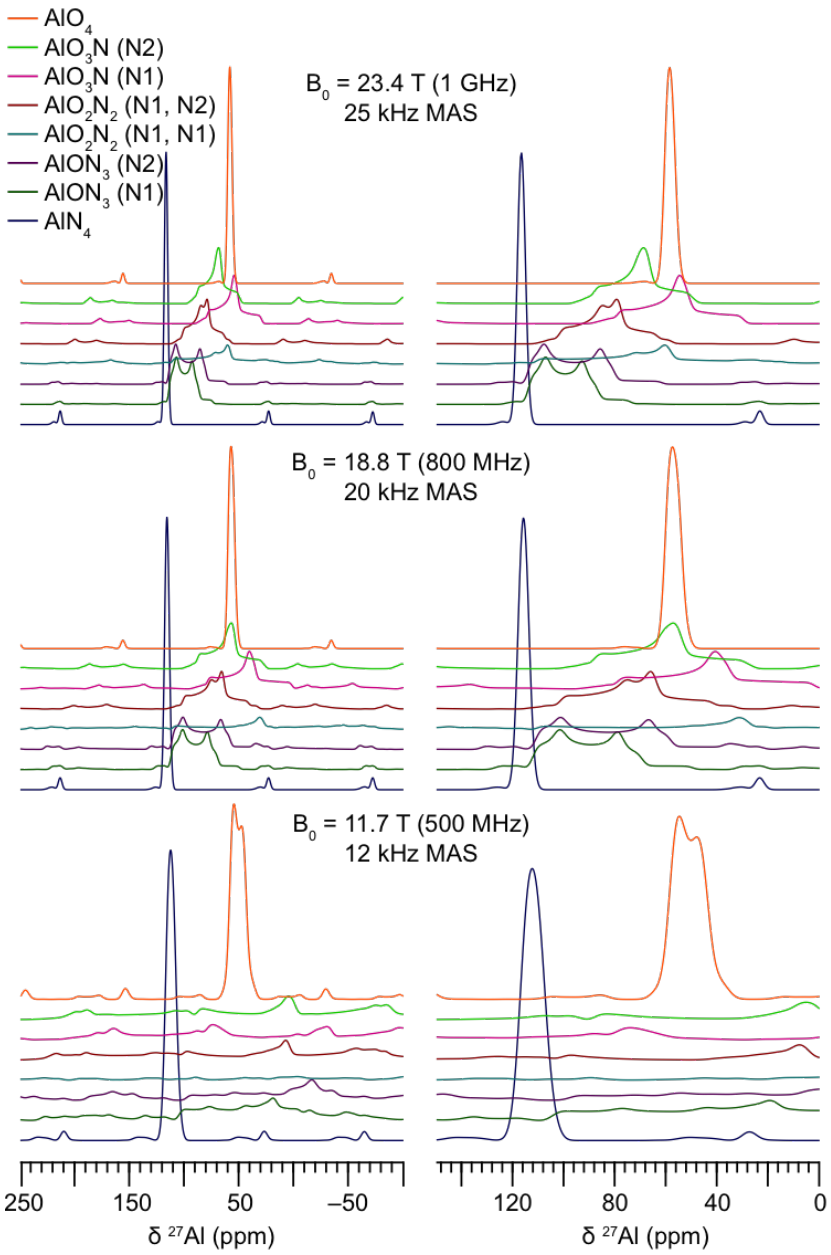

Figure 2.6: Calculations of ^{27}Al MAS NMR spectra of SiAlON for different fields and spinning speeds showing that certain quadrupolar environments can only be resolved with high fields. © 2017 American Chemical Society.

NMR calculations for magnetic shielding, shielding anisotropy, and the electric field gradient (EFG) tensor were performed. ^{27}Al C_Q ranges (MHz) versus δ (^{27}Al) (ppm) ranges computed in this study are shown in Figure 2.4. The fits of the experimental NMR data are shown in Figure 2.5 with parameters shown in Table 2.4. Lineshapes were fit to the data as informed by the range of values for each parameter from the calculations. Only the central line of the experimental spectra was fit. The relatively low intensity of the spinning sidebands as well as baseline distortions, both common issues for small quantities of quadrupolar nuclei, would complicate inclusion of the spinning sideband manifold. Pseudo-Voigt broadening was applied. As the calculations indicate, the NMR parameters are dominated by nearest neighbors but are still significantly affected by next-nearest neighbors and beyond. While to the first coordination shell (one bond, 2.25 Å) there are only five possible local environments for Al (*i.e.,* AlO_qN_{4-q} where $0 \leq q \leq 4$), the number of distinct environments increases rapidly with cluster size. For simplicity, the smallest number of possible sites was used to achieve a satisfactory fit, but it is likely that there are many similar Al sites. C_Q values of 0 were not observed computationally or experimentally for AlO_4 or AlN_4 sites, which is due to the fact that the tetrahedra are distorted, even in the Si_3N_4 structure with no site disorder (via DFT, the EFG tensor is non-zero at the Si nucleus in Si_3N_4, but Si

is an $I=1/2$ nucleus, meaning that cannot be observed experimentally). While the other environments could be axially symmetric with an η value close to 1, this is also not observed. The symmetry is further broken by the presence of long-range defects away from the AlO_4 or AlN_4 sites. In addition, simulations of quadrupolar NMR lineshapes for different fields and spinning rates (Figure 2.6) highlight the requirement for ultrahigh field and high spinning speeds to resolve Al sites in SiAlONs. These data should prove useful for planning and executing future NMR studies of this large family of materials.

Further evidence for the experimentally observed preference for $AlON_3$ formation and its subsequent effects on the population of other tetrahedral environments is observed by comparing the experiment to a statistical model, and is shown in Figure 2.7. From the DFT-informed fits of the experimental NMR data, the ratio of AlN_4:$AlON_3$:AlO_2N_2/AlO_3N is 16:54:30 for $z = 0.050$, 8:64:28 for $z = 0.075$, and 7:69:24 for $z = 0.125$, with an approximate error estimate of 5% due to site overlap. The relative intensities were fit by least squares refinement with the DFT-calculated values used as initial values. A stochastic model (*i.e.*, random, statistical distribution) predicts 97.5%, 96.3%, and 93.9% AlN_4 for samples $z = 0.050$, $z = 0.075$, and $z = 0.125$, respectively, providing further evidence for preferential Al–O bond formation instead of a random distribution of Al and O within the Si_3N_4 structure. For $AlON_3$, the

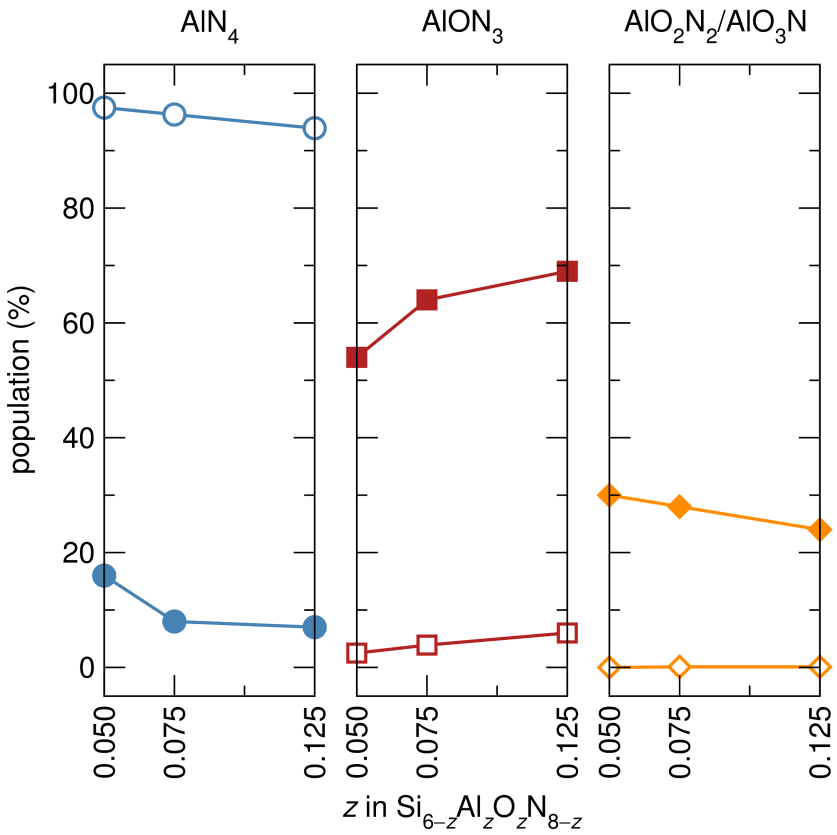

Figure 2.7: Populations obtained from fitting the experimental NMR data (closed shapes) show a definite preference for $AlON_3$ formation and a decrease in AlN_4 and AlO_2N_2/AlO_3N populations. This is in stark contrast to the stochastic model (open shapes), which predicts high population of AlN_4 environments, low population of $AlON_3$ tetrahedra, and virtually no AlO_2N_2/AlO_3N. © 2017 American Chemical Society.

stochastic model predicts 2.5%, 3.6%, and 6.0% for $z = 0.050$, $z = 0.075$, and $z = 0.125$, respectively, and virtually zero (0.0%, 0.1%, and 0.1%) for AlO_2N_2. Thus, there is a definite preference for $AlON_3$ formation experimentally.

DFT calculations of the energies for various tetrahedral environments (Figure 2.3) performed on a $2 \times 2 \times 2$ supercell with relaxed atomic coordinates and $z = 0.075$ lattice parameters are provided in Table 2.5 referenced to the least favorable configuration. Variation of the lattice parameters in the range determined from synchrotron diffraction yielded defect enthalpies within ± 0.04 eV of the intermediate lattice parameters used for enthalpy calculations. Thus, the increase in unit cell size that accompanies increased defect concentration does not significantly affect these calculations. In all defect configurations, the energy decreased as the number of Al–O bonds increased. For each composition, the baseline energy was calculated as the relaxed energy with Al only in AlN_4 tetrahedra and the corresponding number of O as OSi_3 (Figure 2.3a). For a single defect pair (1Al–1O) in the $2 \times 2 \times 2$ supercell (corresponding to $z = 0.125$), the localization of Al–O forms a bond greater than 1 eV more stable than when the defect atoms are separated. In addition, it was discovered that oxygen atoms prefer to sit on the N2 site (0.2 eV–0.3 eV preference in all mixed anion tetrahedral configurations) isolated from the large hexagonal tunnel along the c-axis. Unfortunately, the two $AlON_3$ sites

Table 2.5: Table of energy values for defects show energetic preference for $AlON_3$ bonding in two doping levels closest to that investigated experimentally. A defect is defined as the introduction of one Al–O pair.

Composition	Defect geometry (O on N1 or N2)	eV/defect
1Al-1O	AlN_4	0.00
1Al-1O	$AlON_3$ (N1)	-1.2
1Al-1O	$AlON_3$ (N2)	-1.4
2Al-2O	AlN_4	0.00
	AlN_4	
2Al-2O	AlO_2N_2 (N1, N2)	-1.1
	AlN_4	
2Al-2O	$AlON_3$ (N1)	-1.2
	$AlON_3$ (N1)	
2Al-2O	$AlON_3$ (N2)	-1.4
	$AlON_3$ (N1)	
2Al-2O	AlO_2N_2 (N1, N2)	-1.6
	$AlON_3$ (N2)	

cannot be differentiated based on their NMR parameters, meaning the NMR data cannot be directly related to the energetics of the distinct $AlON_3$ environments. For 2 Al and 2 O, corresponding to $z = 0.25$, two adjacent AlO_2N_2 and $AlON_3$ tetrahedra with corner sharing Al atoms and oxygen corner sharing between three tetrahedra are most energetically favorable. Defects for more than 2 Al and 2 O correspond to Al contents much higher than that studied experimentally in the present work (Table 2.2), where the most energetically favorable tetrahedral configurations are marked by the presence of clustered defects and an increase in the number of corner connected oxygen atoms that are joined to two Al atoms.

Simple electrostatic bond valence arguments can be made to justify the stability of Al–O pairs the β-Si_3N_4 framework. An isolated O defect on an N site would receive three charges from neighboring Si atoms, leading it to possess a net negative charge. An isolated Al defect on an Si site would have four N neighbors, each seeking a positive charge, requiring the Al to possess a net positive charge. These charge defects would annihilate and stabilize when they are nearest neighbors.

In conclusion, we have shown that Al and O have a surprising affinity for one-another in the β-SiAlON structure, despite the high dilution of both Al and O in the framework. High-field ^{27}Al solid-state NMR spectral features have been assigned to different AlO_qN_{4-q} ($0 \leq q \leq 4$) species, employing DFT calculations

to help in the assignment. These results suggest unambiguously that $AlON_3$ with $q = 1$ and AlO_2N_2 with $q = 2$ are found in far greater excess than would be suggested by a stochastic distribution of Al and O on the β-Si_3N_4 framework. DFT calculations of defect energetics on large supercells also suggest extra stabilization associated with Al–O clustering in the unit cell, which can be anticipated by electrostatic bond valence arguments. This work also shows the exquisite details of local compositional fluctuations in crystal structure that can be unravelled by the judicious combination of high-field, high-resolution NMR experiments coupled with DFT calculations.

Chapter 3

Understanding the links between composition, structure, and luminescence properties in green-emitting β-$Si_{6-z}Al_zO_zN_{8-z}$:Eu^{2+} phosphor

[1]The contents of this chapter have substantially appeared in Reference [71]: C. Cozzan, G. Laurita, M. W. Gaultois, M. Cohen, A. A. Mikhailovsky, M. Balasubramanian, and R. Seshadri, Understanding the links between composition, polyhedral distortion, and luminescence properties in green-emitting β-$Si_{6-z}Al_zO_zN_{8-z}$:Eu^{2+} phosphor, *J. Mater. Chem. C* **5** (2017) 10039–10046.

Inorganic phosphor materials play a crucial role in the creation of white light from blue and near-UV solid-state light-emitting diodes. Understanding the intricacies of phosphor structure is key for setting the stage for improved, more efficient functionality. Average structure and coordination environment analysis of the robust and efficient green-emitting phosphor, β-SiAlON:Eu^{2+} (β-$Si_{6-z}Al_zO_zN_{8-z}Eu_{0.009}$), are combined here with a range of property measurements to elucidate the role of Al content (z) on luminescence properties, including the red shift of emission and the thermal quenching of luminescence as a function of increasing Al content z. Average structure techniques reveal changes in polyhedral distortion with increasing z for the 9-coordinate Eu site in β-SiAlON:Eu^{2+}. X-ray absorption near edge structure (XANES) is used to confirm that the majority of the activator Eu is in the Eu^{2+} state, exhibiting the symmetry-allowed and efficient $4f^7 5d^0 \longrightarrow 4f^6 5d^1$ transitions. Room temperature and temperature-dependent luminescence indicate an curious increase in thermal stability with increasing z over a small range due to an increasing barrier for thermal ionization, which is correlated to an increase in the quantum yield of the phosphor.

3.1 Introduction

Since the first development of affordable and efficient blue light-emitting diodes (LEDs) by Nakamura and coworkers,[72] solid-state white lighting is rapidly replacing other types of light sources.[73] Crucial to the success of this technology are inorganic phosphors that partially convert radiation from the solid-state source to longer wavelengths.[2] One of the strategies for creating white light is to use a near-UV or UV source to excite a mixture of red-, green-, and blue-emitting phosphors to render warm white light with high color rendering indices.[18] For this approach, a green-emitting phosphor of particular interest is β-SiAlON:Eu^{2+}. This phosphor displays excitation from the near-UV to blue with high quantum yields[74] due to the rigid parent Si–N tetrahedral framework in this solid solution phosphor.[52] Like other solid solution phosphors, the optical properties can be chemically tuned.[75–77] High lattice rigidity[4, 69] leads to high efficiencies at small Al concentrations (most closely resembling the Si_3N_4 lattice), with rigidity decreasing for more Al substitution.[52, 74] For future high-power lighting applications,[21] the thermal stability and high efficiency of β-SiAlON:Eu^{2+} render it a suitable phosphor for generating light using blue laser diode excitation.[22]

It is well-known that both the host structure and the local coordination

environment of the emission center in phosphors dictate the emission behavior.[2] β-SiAlON:Eu^{2+} crystallizes in the Si_3N_4-type structure (space group $P6_3$, no. 173).[52] A large size mismatch between cations in the structure and the Eu^{2+} cation suggests that the luminescence center (Eu^{2+}) substitutes on an interstitial site, which was confirmed by scanning transmission electron microscopy (STEM)[78] and supported separately by density functional theory (DFT) used in conjunction with Eu L_3 extended X-ray absorption fine structure (EXAFS),[52] which is challenging both due to the difficulty of modeling f-electrons and the inherently low amount of Eu in the system. Both investigations provided evidence that the Eu^{2+} substitutes in the channel on the 2a Wyckoff site with local distortions present.[52, 78] Furthermore, the inclusion of the rare earth necessitates changes in the Si:Al and N:O ratios to maintain charge neutrality, which in turn influences the coordination environment of the rare earth. The consequences on the β-SiAlON structure for small Al/O substitutions were recently investigated experimentally using synchrotron X-ray diffraction and ^{27}Al MAS NMR coupled with DFT calculations of NMR parameters and defect structure energetics.[41] Separately, computational studies predicted effects of Al/O substitution on the properties of β-SiAlON:Eu^{2+} phosphors.[79]

These recent first principles calculations by Wang *et. al.* sought to establish

chemical rules for the β-SiAlON:Eu^{2+} system as well as describe the origins of the high quenching resistance, the emission peak characteristics, and the changes in emission wavelength as a function of z in β-$Si_{6-z}Al_zO_zN_{8-z}Eu^{2+}$ for fixed Eu doping.[79] Using DFT, the authors observed that with increasing z ($z = 0.125$ to $z = 0.167$), the Eu-N/O bond lengths increased and distorted the dopant site, which was assigned a 9-coordinate Eu-N/O_9 polyhedron in the $2a$ Wykcoff position. In their calculations, broadening of the emission peak and a red shift due to a larger crystal field splitting were observed due to these distortions in the Eu^{2+} environment. A slight decrease in band gap was also observed with increasing z, likely also contributing to the red shift. Calculations on the thermal ionization barrier for a fixed Eu amount interestingly observed that the barrier increased from $z = 0.125$ to $z = 0.167$ and then decreased at z values greater than $z = 0.167$ due to an increasing gap between the $5d$ levels and the conduction band of the host lattice. This is the first report of such behavior and offers an interesting compositional range to experimentally target for the highest performing β-SiAlON:Eu^{2+} phosphors.

In the current work, we present the first experimental verification of red shift, emission broadening, and thermal stability increases for small z ranges in phase pure and highly efficient β-$Si_{6-z}Al_zO_zN_{8-z}Eu^{2+}$ phosphors. Samples with fixed nominal Eu content ($Eu_{0.009}$) and systematically varying Al/O content

($z = 0.050$, $z = 0.075$, and $z = 0.125$) were studied. The solubility of rare earth ions in the host lattice is limited by the stability of the cation in the interstitial site,[52, 80] rendering traditional techniques such as X-ray diffraction not capable of direct observation of the precise dopant atom location within the channels. Synchrotron X-ray diffraction[41] can be used to probe average structure and is applied here to investigate any links between average structure changes in the Eu coordination environment location in the crystal and the observed physical properties. X-ray absorption near edge structure (XANES) of the Eu L_3 edge shows the oxidation state of the Eu in the different samples is constant (Eu^{2+}:Eu^{3+} remains the same) across the z range studied presently. It was hypothesized that an optimal Al^{3+}/O^{2-} concentration used to charge balance Eu^{2+} could be targeted to achieve high quantum yield and good thermal stability. Room temperature and temperature dependent photoluminescence measurements were conducted to analyze the photoluminescence quantum yield (PLQY) and thermal stability of the phosphors as a function of z, with the highest luminescence and thermal stability observed for $z = 0.125$. Our work supports the findings of Wang *et. al*,[79] indicating a red shift and broadening of the emission spectra. We find the trend of polyhedral distortion as a function of z varies depending on the assigned location of Eu along the c-axis of the $2a$ site, and bond valence sum calculations suggest this is not in the direct center

of the channel, *i.e.,* a 12-coordinate polyhedral site (distortion is observed for a Eu-N/O_9 polyhedra and not for a Eu-N/O_{12} polyhedron). The current work observes that if the dopant atom resides in the energetically and valency favored Eu-N/O_9 polyhedron, trends in distortion of the luminescent center explain the experimentally observed red shift, emission broadening, and increasing thermal stability as a function of Al content, with quantum yield shown to follow the same trend.

3.2 Methods

Powders of α-Si_3N_4, Al_2O_3, and Eu_2O_3 were ground with nominal stoichiometry $Si_{6-z}Al_zN_{8-z}O_zEu_{0.009}$ ($z = 0.050$, $z = 0.075$, and $z = 0.125$) in an alumina pestle, with charge balancing of the Eu^{2+} achieved via co-substitution of Al^{3+} and O^{2-}. The powders were heated in a boron nitride crucible at 2223 K for 12 h under N_2 (>99.9995%) at a pressure of 0.92 MPa and annealed in argon for 8 h before being ground into a fine powder and washed using a mixture of HNO_3 and HF.

Collection and analysis of synchrotron X-ray diffraction data as related to this work are described elsewhere.[41] The polyhedral distortion index (D) and bond valence sum (BVS) were calculated based on bond lengths as

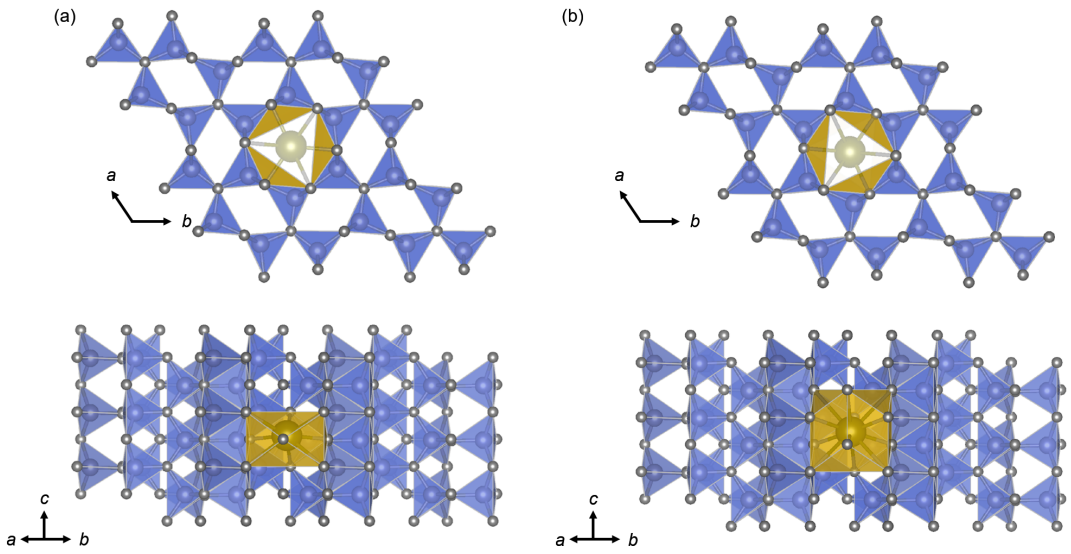

Figure 3.1: Hexagonal $P6_3$ (no. 173) crystal structure of Eu^{2+} doped β-$Si_{6-z}Al_zO_zN_{8-z}$ with the Eu coordination sites highlighted in yellow. (a) Eu environment in the $2a$ Wyckoff site with an atomic position of $(0, 0, \frac{1}{3})$ results in a 9-coordinate site whereas (b) an atomic position of $(0, 0, \frac{1}{2})$ results in a 12-coordinate site. Coordination polyhedra are defined by Eu–O/N bonds under 3.45 Å.

defined by Baur[81] and implemented using the open-source crystallographic software VESTA.[59] Eu L_3 edge spectra were collected using beamline 20-BM at the Advanced Photon Source, Argonne National Laboratory. Samples were irradiated using an unfocused X-ray beam, and fluorescence spectra at 295 K were collected from powder encapsulated in Kapton® tape oriented at 45° using a 13-element Ge detector perpendicular to the incident X-ray beam. The incident photon energy was calibrated using the Fe K absorption energy of Fe metal foil (E_0 = 7112 eV), and monitored throughout the experiments using the Eu L_3 absorption energy of Eu_2O_3 powder (E_0 = 6971 eV) collected concurrently in transmission mode. The instrumental resolution is 1 eV at these energies. Data were processed using the Demeter software suite.[82]

Room temperature photoluminescence spectra and photoluminescence quantum yield (PLQY) were measured using a fluorescence spectrometer (Horiba, Fluoromax 4). Phosphors were thoroughly mixed by 25-wt % in a silicone matrix (Momentive, RTV-615) using a high speed mixing system (FlackTek Inc., DAC 150.1 FVZ-K) at 1500 rpm for 2 min, and subsequently deposited on a 100 mm^2 fused silica substrate (Chemglass) and heated at 398 K for 15 min in a box furnace to accelerate the curing process. Phosphors encapsulated in a silicone matrix were then placed in a 15 cm diameter, Spectralon®-coated integrating sphere (Horiba, Quanta-ϕ) and excited using

light with a wavelength of 405 nm and 450 nm generated by a 150 W continuous output, ozone-free xenon lamp. Slit widths for the excitation and emission monochromaters were held constant at 2.00 nm, and a metallic neutral density filter (Newport) was used. The wavelength spread, or bandpass (nm), is given by the dispersion (4.25 nm for the FluoroMax-4). Quantum yield was calculated based on the work by de Mello *et al.*[83] The temperature dependence of the PLQY was measured from 77 K to 503 K in 30 K increments using a home-built fluorometer with a cryostat sample stage for low temperatures and a heating stage for high temperatures. Samples were prepared in the same manner described for room temperature measurements.

3.3 Results and discussion

Eu^{2+} doped β-$Si_{6-z}Al_zO_zN_{8-z}$ consists of densely packed, corner sharing $(Si,Al)(O,N)_4$ tetrahedra that crystallize in the hexagonal space group $P6_3$ (no. 173) with a channel along the c-axis. The likelihood that the dopant is located in this channel in the 2a Wyckoff site has been experimentally verified through STEM[78] and EXAFS studies.[52] However, this is not a special position, as the 2a site in this space group is located at $(0, 0, c)$, and the precise location of the Eu dopants along the channel has not been experimentally

reported. DFT results indicated that for the (001) plane, the lowest energy region lies in the center of the channel in the a, b direction, and the energy increases as one moves away from the channel.[52] The 2a site is large potential well with the dopant in the $(0, 0, c)$ position. From a chemical standpoint, shifting the atom in the a or b direction results in more over-bonding due to the shorter bonds and a higher BVS, and is therefore less likely than the $(0, 0, c)$ position. Therefore, specific positions along the channel in the $(0, 0, c)$ positions are evaluated in the present work using BVS and D.

In the structure of in β-$Si_{6-z}Al_zO_zN_{8-z}$, Al substitutes on the Si site and O substitutes on the N site. For z contents evaluated presently, oxygen bonds are likely to influence the local dopant environment, which is denoted as Eu-N/O_9 in the present work. The in-channel c position is of importance when defining the polyhedral environment of the Eu, as is illustrated in Figure 3.1. For defined Eu-N/O bond lengths of $<$3.45 Å, an atomic position of $(0, 0, \frac{1}{3})$ results in a 9-coordinate site (Figure 3.1a) whereas an atomic position of $(0, 0, \frac{1}{2})$ results in a 12-coordinate site (Figure 3.1b). Therefore the location within the channel must be considered when discussing the coordination environment of the activator ion.

Our recent analysis on synchrotron X-ray data of β-$Si_{6-z}Al_zO_zN_{8-z}$ ($z = 0.050$, $z = 0.075$, and $z = 0.125$), Rietveld fits shown in Figure 3.2,

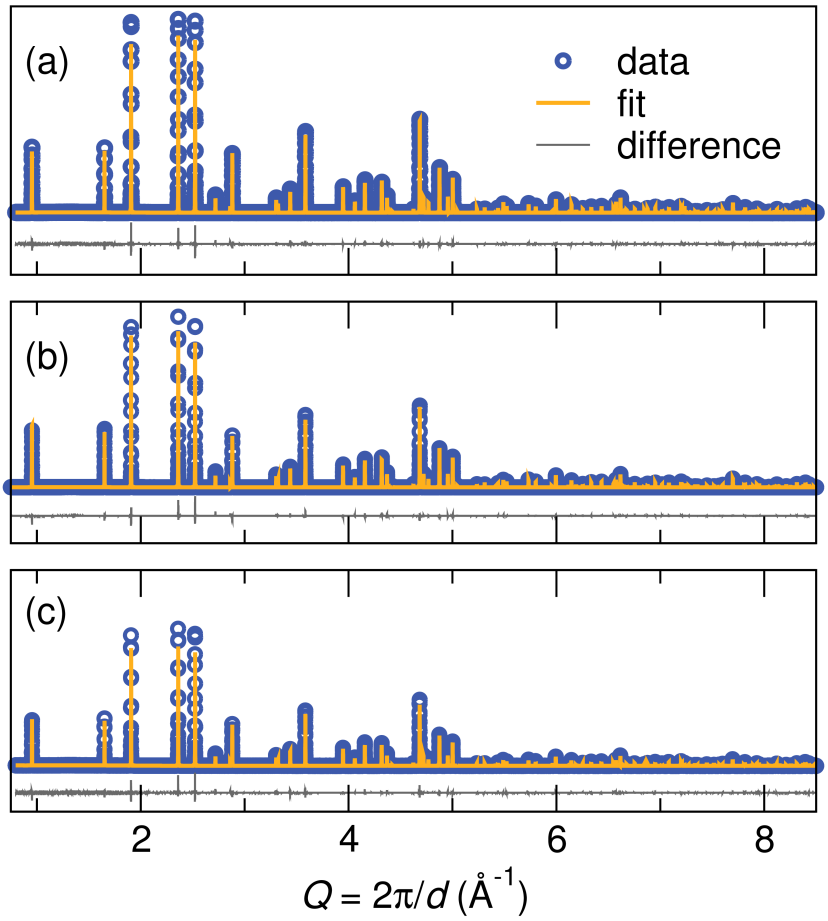

Figure 3.2: Rietveld fits of synchrotron X-ray data reported in Cozzan *et al.*[41] for the series β-$Si_{6-z}Al_zO_zN_{8-z}$ [(a) $z = 0.050$, (b) $z = 0.075$, and (c) $z = 0.125$]. All samples are phase pure and indexed to the $P6_3$ space group. © The Royal Society of Chemistry 2017.

revealed an overall increase in the unit cell volume with increasing z.[41] This was in agreement with the first principles calculations by Wang *et. al.*, where the volume and average bond length increased with increasing z due to longer Al–N and Al–O bonds when compared to Si–N bonds.[79] In addition to an increase in the unit cell volume, the first principles study addressed the effect of the c position of the Eu in the 2a channel, finding changes in the relative energy of the β-$Si_{6-z}Al_zO_zN_{8-z}$ structure as a function of the fractional c coordinate of Eu. Based on this work they determined the lowest-energy structure consists of an Eu dopant that is in the same (000l) plane as the Al and O atoms and determined a polyhedral distortion of the resulting 9-coordinate Eu site with an increase in Al and O substitution. Through this work they outlined three rules for achieving a low-energy β-$Si_{6-z}Al_zO_zN_{8-z}$ structure: (1) All O must occupy the 2c Wyckoff sites, (2) all O must have at least one Al neighbor, and (3) all Al, O, and Eu must be in the same (000l) plane.

In the present work, the average atomic positions calculated from Rietveld refinements have been used to calculate bond distances, polyhedral volumes, and D as a function of Al/O content for chosen positions of $(0, 0, c)$ in the 2a Wyckoff position (Figure 3.3a) in the doped β-$Si_{6-z}Al_zO_zN_{8-z}$ unit cell. The terms Eu site and 2a site are referred to interchangeably in the present work. By studying characteristics of the bonding environment of the dopant site at

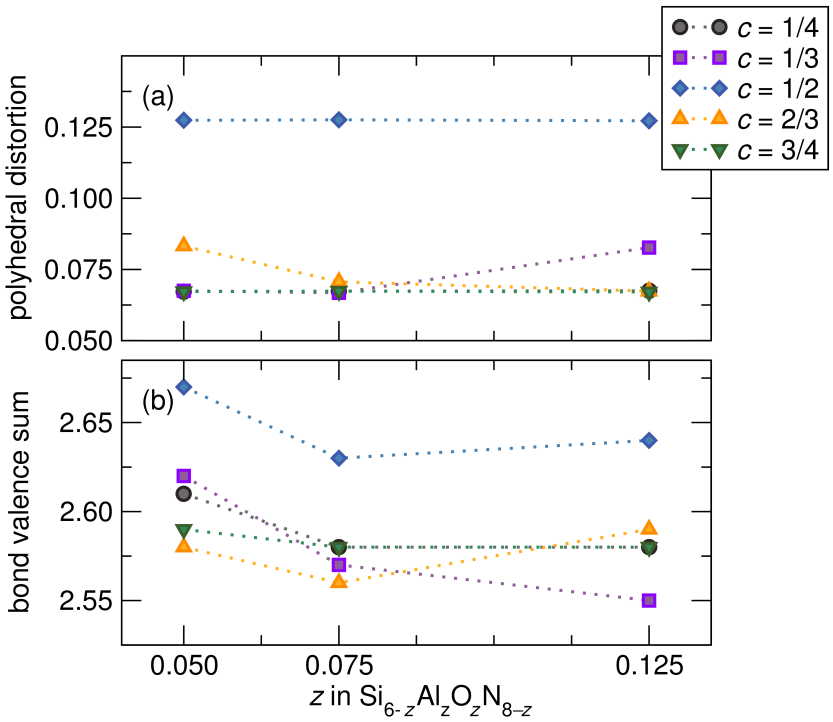

Figure 3.3: (a) Polyhedral distortion of the Eu coordination polyhedra as a function of Al/O content for defined positions of $(0, 0, c)$ in the $2a$ Wyckoff position. Positions of $c{=}\frac{1}{4}$, $c{=}\frac{1}{2}$, and $c{=}\frac{3}{4}$ result in a minimal change in distortion with increasing Al/O content, while $c{=}\frac{1}{3}$ and $c{=}\frac{2}{3}$ result in increasing and decreasing distortion with Al/O content, respectively, highlighting the importance of the in-channel location of the Eu^{2+} activator ion. Bond valence sum (BVS) calculations indicate that for all compositions, a c location off of the center of the channel ($c{=}\frac{1}{2}$) results in Eu^{2+} being closer to the 2+ valency, suggesting Eu does not sit in the center of the site along the c-axis. © The Royal Society of Chemistry 2017.

Table 3.1: Select structural data obtained from Rietveld refinements of X-ray synchrotron diffraction data for β-$Si_{6-z}Al_zO_zN_{8-z}$ with $z = 0.075$ as reported in our previous study.[41] Numbers in parentheses show standard deviation on the last number. Si/Al and O2/N2 c parameters reported to illustrate approximate location of (000l) plane used to estimate the c positional parameter of Eu^{2+} based on guidelines set by Wang *et al.*[79]

Al content (z)	0.050	0.075	0.125
Cell a (Å)	7.60584(1)	7.60692(2)	7.60853(2)
Cell c (Å)	2.90844(3)	2.90903(3)	2.91011(3)
Cell V (Å^3)	145.709(2)	145.780(2)	145.896(2)
Si/Al positional c	0.291(5)	0.250(3)	0.290(5)
O2/N2 positional c	0.281(7)	0.238(6)	0.28(5)

chosen c values, such as coordination number and bond valence sum (BVS), our average structure data allows for an understanding of the most likely position in the channel despite not directly probing the dopant in the material. Eu coordination polyhedra were defined by Eu-N/O bond lengths $<$3.45 Å, resulting in a 9-coordinate site for c=$\frac{1}{4}$, c=$\frac{1}{3}$, c=$\frac{2}{3}$, and c=$\frac{3}{4}$ and a 12-coordinate site for c=$\frac{1}{2}$ in all compositions. It is observed that positions of c=$\frac{1}{4}$, c=$\frac{1}{2}$, and c=$\frac{3}{4}$ result in a minimal change in distortion with increasing Al/O content, while c=$\frac{1}{3}$ and c=$\frac{2}{3}$ result in increasing and decreasing distortion with Al/O content, respectively. To provide more insight on the probable location of the Eu within the channel, BVS as a function of Al/O content were calculated for the defined positions (Figure 3.3b).[84] Previous work using EXAFS demonstrated that a BVS of 2 is obtained when long bond lengths (4 Å) are considered.[52] There is some ambiguity in the precise determination of the local dopant bonding environment due to such low Eu, and the exact position of the Eu along the channel has not yet been directly observed. BVS as utilized in the current work is therefore a guide to understanding the bonding environment of the 2a site on average in structures varying as a function of Al/O content, suggesting which location of the Eu is the least over-bonded. All positions result in over-bonded Eu with BVS above 2.5 (compared to the optimal BVS of 2.0), but this is slightly relieved when Eu does not occupy the center of the channel (c=$\frac{1}{2}$). Deviations

from the ideal BVS of 2 as expected for Eu^{2+} might also arise due to local disorder of the O in the polyhedron that is not captured using crystallographic techniques. Following the Eu positional rules outlined by the previous first principles work,[79] a c position of approximately 0.3 would place Eu in the proper (000l) plane for our refined structures (Table 4.1) with bonds along the plane. This value is closest to the calculated c=$\frac{1}{3}$, suggesting that an increase in the polyhedral distortion of the 9-coordinate Eu site occurs with increasing Al/O content. The current work provides experimental support for investigating Eu-N/O_9 polyhedra, which corroborates recent work by other authors.[79, 85]

XANES of the Eu L_3 edge was collected to observe the valence state of Eu in the phosphors (Figure 3.4). The majority of Eu in the samples is in the optically active, *i.e.*, allowed 4f$\longrightarrow$5d transitions, Eu^{2+} state due to the highly reducing processing atmosphere of N_2 (>99.9995%) at a pressure of 0.92 MPa and the subsequent argon anneal. Quantitative fitting of XANES data using two arctangent steps and two Gaussian functions was performed using Eu_2O_3 as a reference, resulting in a calculated 81% of Eu^{2+}, and 19% Eu3+ ($\pm$ 5%) for each sample. A representative XANES fit with the individual Gaussian components for Eu^{2+} and Eu^{3+} is shown in Figure for the z=0.050 sample (arctangent steps not shown for clarity). The relative amount of Eu^{2+}:Eu^{3+} is constant regardless of z, indicating that any observed differences in the optical properties with varying

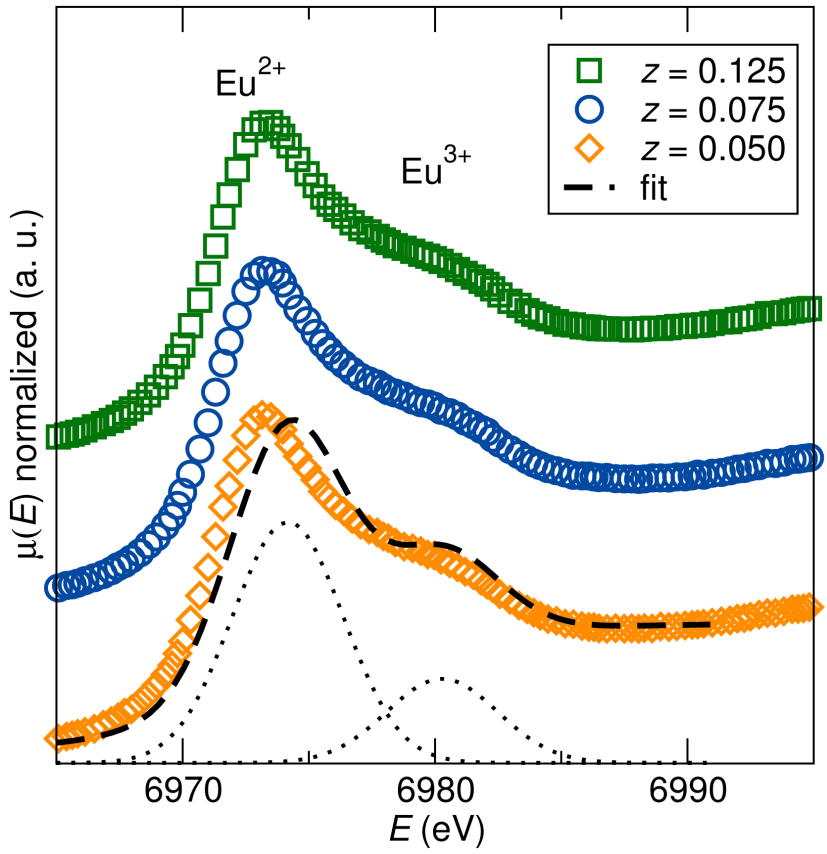

Figure 3.4: XANES of the Eu L_3 edge shows the valence state of Eu is 81% ($\pm$ 5%) Eu^{2+} for the series of β-$Si_{6-z}Al_zO_zN_{8-z}$:$Eu_{0.009}$ with varying z. A representative XANES fit is shown (dashed line) for the z=0.050 sample with individual Gaussian components for Eu^{2+} and Eu^{3+} (dotted lines) shown and arctangent steps not shown for clarity.

Table 3.2: Peak maximum and FWHM of the emission spectra. Increasing z shows a small red shift in the emission.

Al content z	maximum (nm)	FWHM (nm)
0.050	531	46
0.075	535	46
0.125	537	48

z is due to structural changes and not to the Eu^{2+}:Eu^{3+} ratio.

Eu^{2+} doped β-$Si_{6-z}Al_zO_zN_{8-z}$ displays green emission and is readily excited by $\lambda_{ex} = 405\,\text{nm}$ (near UV) and λ_{ex} = 450 nm (blue) due to broad excitation,[86–88] with excitation (line) and emission (circles) profiles for λ_{ex} = 450 nm for different z values shown in Figure 3.5. The emission spectra were deconvoluted on an energy scale (cm^{-1}) using one Gaussian peak corresponding to one crystallographically unique luminescent center in the unit cell. The tail of the emission profile is not captured by a single Gaussian, and is likely due to a distribution of dopant positions due to small fluctuations in channel position in the phosphor. Additionally, small changes in the dopant environment due to local changes in N/O can result in a distribution of local activator environments. The emission and broad excitation spectra are due to the allowed $4f^6 5d^1 \longrightarrow 4f^7$ transition in Eu^{2+}. Values for the maximum emission wavelength and full

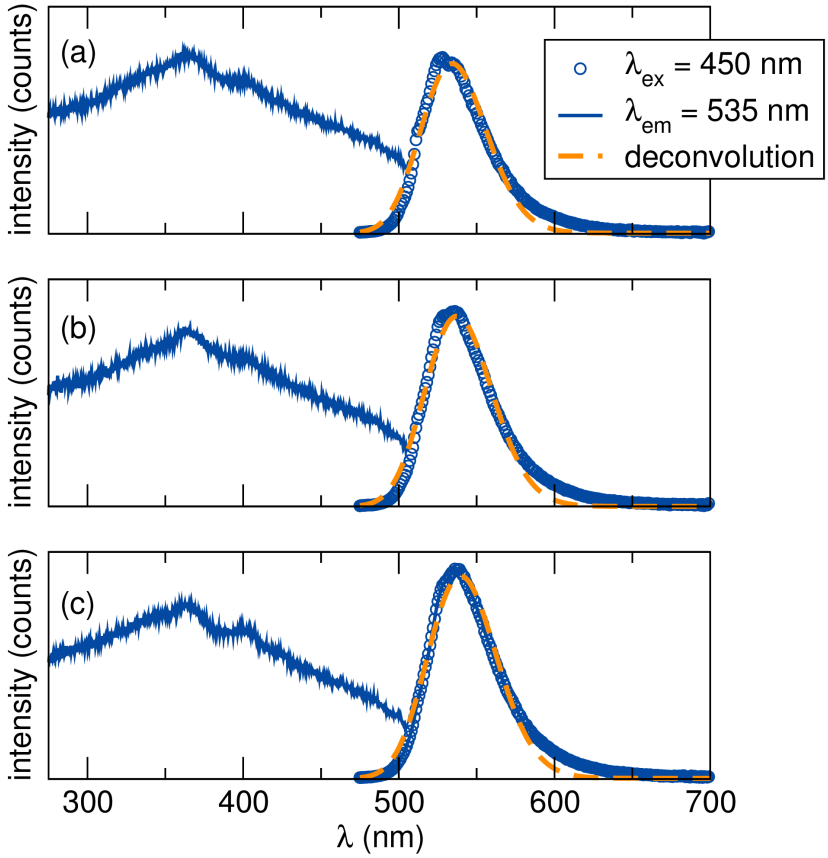

Figure 3.5: Emission spectra deconvolution with one Gaussian peak shape for (a) $z = 0.050$, (b) $z = 0.075$, and (c) $z = 0.125$ show the contributions of the activator site for each phosphor, with one peak accounting for one unique position of Eu^{2+} in the unit cell. The tail of the emission profile is not captured by a single Gaussian, likely due to a distribution of dopant positions due to small fluctuations in channel position and/or small changes in the dopant environment due to local changes in N/O distribution. Intensity is plotted in counts (arbitrary units). © The Royal Society of Chemistry 2017.

width at half maximum (FWHM) of the Gaussian peak shape fits are shown in Table 3.2. There is a clear red shift in emission for increasing amounts of Al substitution. The observed optical behavior in β-$Si_{6-z}Al_zO_zN_{8-z}$ with increasing z is not well explained by average bond lengths or polarizability of nitrogen,[2] as a red shift is observed with both increasing bond length and with increasing O. It has been experimentally observed that polyhedral distortion can alternately dominate crystal field splitting in some garnet-based phosphor systems, where a red shift in the emission was correlated to the distortion of the luminescence center.[89] A red shift in the emission due to polyhedral distortion was calculated by Wang *et. al.*[79] assuming that Eu^{2+} occupies the channel at approximately $(0, 0, \frac{1}{2})$, which is probable based on our own BVS calculations. It is therefore possible that polyhedral distortion is a reasonable mechanism for the red shift in β-$Si_{6-z}Al_zO_zN_{8-z}$ with increasing z.

The red shift can also be visualized by the Commission Internationale de l'Éclairage (CIE) (x, y) coordinates for the phosphor (Figure 3.6), which show an increase in CIE x and a decrease in CIE y with increasing Al/O content (z). Broadening was computationally observed over a larger z range ($z = 0.125$ to $z = 0.167$) by Wang *et. al.*,[79] and the present work observes similar behavior for nominal Al/O amounts of $z = 0.050$ to $z = 0.125$. While an increase in the unit cell volume does not guarantee an increase in Eu-N/O bond distances, we

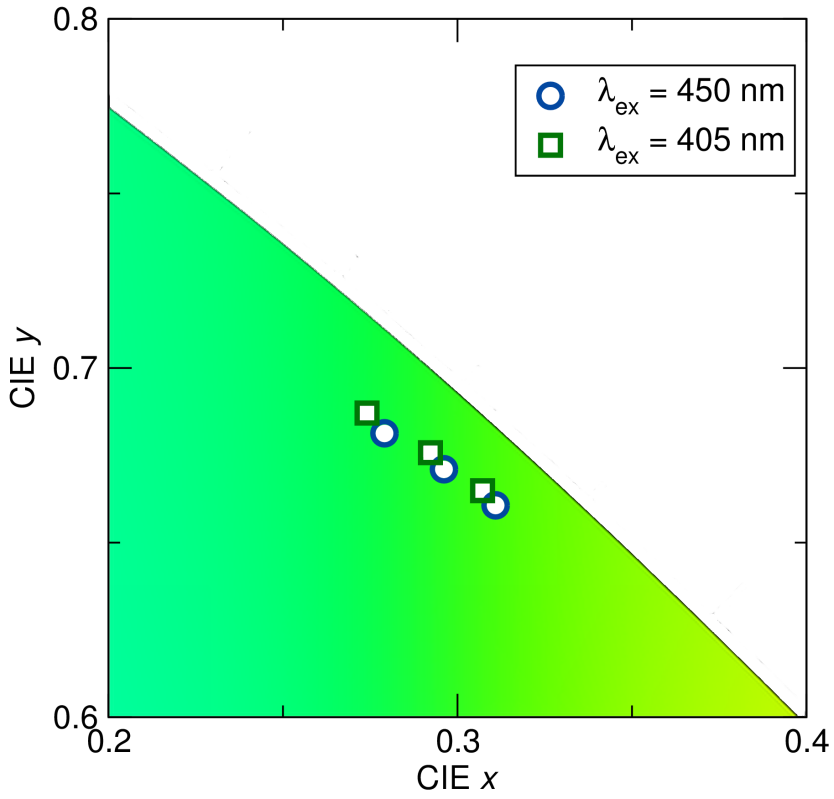

Figure 3.6: CIE coordinates on a section of the 1931 CIE diagram for $\lambda_{ex} = 405$ nm (squares) and $\lambda_{ex} = 450$ nm (circles) for β-$Si_{6-z}Al_zO_zN_{8-z}$:$Eu_{0.009}$ at room temperature. Systematic change, going down and right in the diagram, for the series is due to a red shift in the emission with increasing z. © The Royal Society of Chemistry 2017.

observed an increase in the average bond length around the Eu site from our refinements of X-ray diffraction data. The Eu–N/O bond lengths of the activator site are observed to increase from 2.6710 Å in $z = 0.050$ to 2.6982 Å in $z = 0.125$ assuming an atomic position of $(0, 0, \frac{1}{3})$, which lowers the crystal field splitting and results in the broadening of FWHM of the emission due to an increase in the splitting between the topmost two $4f$ bands. Based on conventional models of phosphor crystal field splitting,[2, 90] nitrides are generally more covalent than oxides and therefore should produce a larger centroid shift than oxides. A larger centroid shift leads to a closer proximity of the d and f levels, resulting in a lower energy difference between the 5d and 4f levels and longer wavelength emission. However, the expected trends based on covalency are not observed here and are likely instead dominated by polyhedral distortion, which is corroborated by recent work on this system.[79, 85] Peak positions and FWHM values of Guassian fits of the emission data (Table 3.2) show a red shift an a slight broadening over the small z range investigated presently, corroborated by recent results on this system investigating photoluminescence behavior at low temperature and high pressure.[85]

For a given z value, more Eu substitution leads to concentration quenching, or a drop in the normalized emission intensity as a function of temperature.[91] Therefore, in the present work, β-$Si_{6-z}Al_zO_zN_{8-z}$:Eu^{2+}

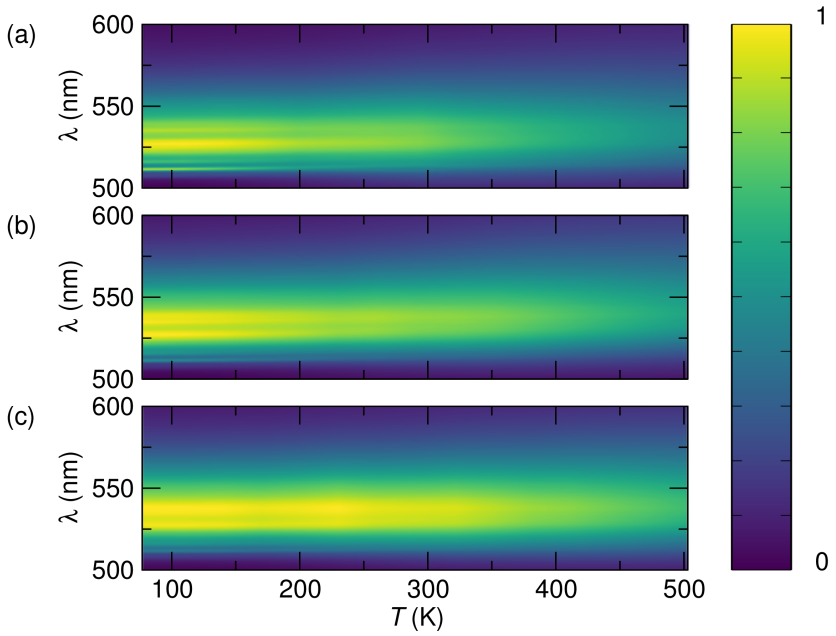

Figure 3.7: Temperature dependent emission intensity is robust across the temperature range for $z = 0.050$ (a), $z = 0.075$ (b), and $z = 0.125$ (c) due to the rigid network of (Si,Al)(O,N)$_4$ tetrahedra and low Eu doping. © The Royal Society of Chemistry 2017.

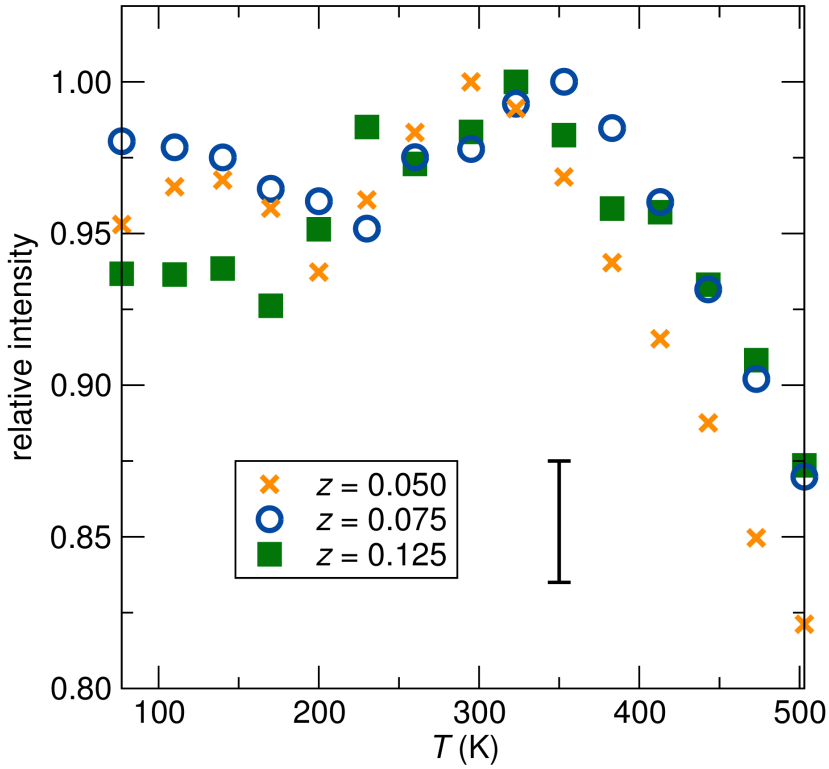

Figure 3.8: Relative intensities of the temperature dependent emission demonstrate higher relative emission intensity at higher temperatures for $z = 0.075$ and $z = 0.125$. Relative emission intensity was computed by taking the integral of the emission profile at each temperature, and dividing by the maximum value for a given sample, which was different for each sample. Shared standard error (displayed next to legend) are ± 0.02. © The Royal Society of Chemistry 2017.

with a nominal composition of 0.9 mol% Eu is studied as the relatively low dopant concentration minimizes the effects of thermal quenching. Temperature-dependent photoluminescence measurements were employed to assess the thermal stability of the phosphors (Figure 3.7). All samples exhibit robust thermal stability due to the rigid network of (Si,Al)(O,N)$_4$ tetrahedra[52] and the large gap (>0.5 eV)[79] between the 5d levels and the host conduction band. Thermal quenching occurs when the 5d electron in the excited 4$f^6$5d^1 state is promoted to the conduction band of the host instead of relaxing to the 4f band.[92] The energy barrier for thermal ionization was calculated to increase with increasing z from 0.125 to 0.167 and then decrease with increasing z from 0.167 to 0.208.[79] The authors were unable to explain this discrepancy between calculation and experiment aside from noting that the barrier is high and the range they studied was more narrow than experimental investigations.[52, 91] The present work experimentally observes the anomalous increase in thermal stability for increasing z over the range of 0.050 to 0.125, with $z = 0.125$ showing the most robust thermal stability up to 500 K. Comparing values for normalized intensity show that both $z = 0.075$ and $z = 0.125$ have higher relative emission intensity at higher temperatures than $z = 0.050$ (Figure 3.8). The low amount of Eu doping (0.09 mol-% nominally) also helps prevent thermal quenching by energy migration, which occurs in

phosphors with higher doping[5] and likely does not occur in the present system as there exists no evidence for activator clustering with the low amounts of Eu dopants explored presently.[52] Fine structure features are observed and are more prominent for lower z at lower temperatures, which arise from the discrete ^7F_J states in Eu^{2+} assuming the Eu^{2+} is bonded ionically and the Eu^{2+} excited state is localized near the $4f$ orbital.[93]

Following the work of Dorenbos,[92] the activation energy for thermal quenching (ΔE) can be calculated using temperature dependent emission intensity as a function of temperature by applying the following equation:

$$\ln[\frac{I(0)}{I(T)} - 1] = \frac{1}{k_B T}\Delta E + \ln\frac{\Gamma_0}{\Gamma_v} \tag{3.1}$$

where $\frac{I(0)}{I(T)}$ is the ratio of the highest intensity in the measured range $I(0)$ to the intensity at a particular temperature $I(T)$, k_B is the Boltzmann constant, T is temperature, Γ_v is the radiative decay rate of the 5*d* state of the activator, and Γ_0 is the attempt rate for thermal quenching. Linear fits of temperature-dependent intensity can then be used to calculate ΔE (Figure 3.9).

In the present work, linear fits of the data from 323 K to 503 K reveals that the calculated ΔE for z=0.05, z=0.075, and z=0.125 is 0.06 eV, 0.25 eV, and 0.20 eV, respectively. Compositions z=0.075 and z=0.125 match well with

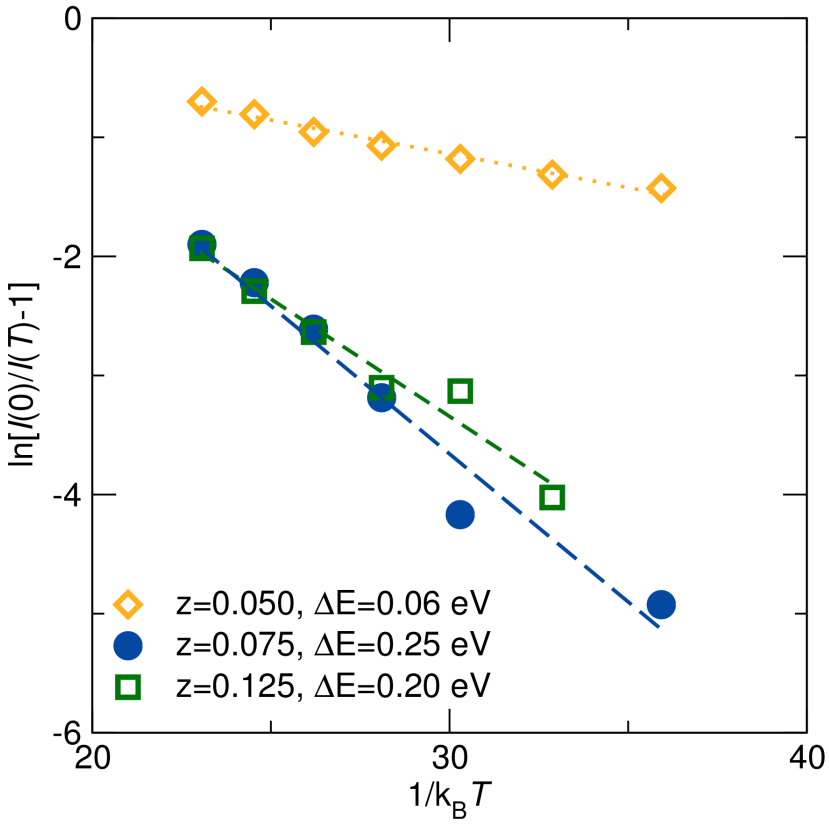

Figure 3.9: Linear fits of $\ln[I(0)/I(T)-1]$ vs. $\frac{1}{k_B T}$ from 323 K to 503 K were used to calculate activation energy of thermal quenching (ΔE) and show relatively high activation energies for z=0.075 and z=0.125. © The Royal Society of Chemistry 2017.

reported values (0.234 eV),[94] which support the observed high resistance to thermal quenching in this system. Data for the entire temperature range measured presently was not accurately captured with a linear fit due to oscillations in the emission intensity as a function of temperature, which is corroborated by recent work on this system[85] and is one possible reason for the discrepancy in the z=0.050 sample. This intensity increase and decrease has also been observed in canonical Ce-doped YAG phosphors for both emission and lifetime, wherein radiative recombination dominates up to a certain temperature (around 523 K) before dropping off due to thermal quenching.[30, 95] The current work observes the same behavior in the β-SiAlON system in addition to robust thermal quenching resistance.

PLQY was measured for both λ_{ex} = 405 nm and λ_{ex} = 450 nm (Figure 3.10). When comparing different compositions at room temperature, we see that PLQY increases with increasing z and that high PLQY values are achieved for both violet and blue excitation. The origins of this trend are likely linked to the calculated high barrier for thermal ionization (0.56-0.68 eV) that increases with increasing z from 0.125 to 0.167.[79] The increasing barrier calculated by Wang *et. al.* results in a high energy penalty for excited states to be promoted to the conduction band instead of relaxing to the 4*f* band to emit a photon. This limits nonradiative processes for increasing z across the small range studied, and

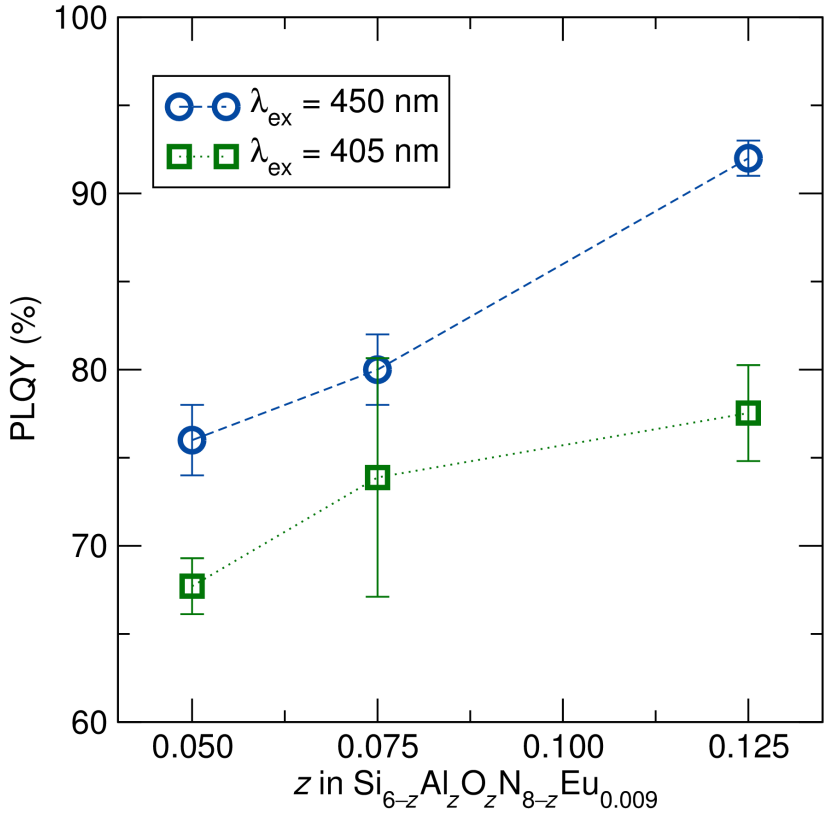

Figure 3.10: Room temperature PLQY collected with $\lambda_{ex} = 405$ nm and $\lambda_{ex} = 450$ nm for the β-$Si_{6-z}Al_zO_zN_{8-z}$:$Eu_{0.009}$ series. Highest efficiency is observed in the highest z sample at both excitation wavelengths. Error bars represent the standard deviation for measurements on three separate samples, and lines were added to guide the eye. © The Royal Society of Chemistry 2017.

offers a possible explanation for the origin of maximum PLQY (92%) observed for the $z = 0.125$ sample in our work. Additionally, the high ratio of Eu^{2+} to Eu^{3+} observed using XANES contributes to the high absolute PLQY values measured for β-$Si_{6-z}Al_zO_zN_{8-z}$:Eu^{2+} phosphors.

In conclusion, specific emission properties can be targeted via compositional tuning, such as narrower emission β-SiAlON:Eu^{2+} (low z) for lower temperature operation, or maximum PLQY and improved thermal stability (higher z up to 0.125) for high flux and/or high temperature operation. We have provided experimental evidence on the role of increasing z at low concentrations in β-$Si_{6-z}Al_zO_zN_{8-z}$:Eu^{2+} in modifying the structure and the resulting optical properties. XANES was used to confirm that the majority of Eu in the structure is in the active Eu^{2+} state, which allows for further investigation of the role of varying z as any observed changes in optical properties are not due to differences in Eu valence between samples. Increasing z distorts the Eu-N/O_9 environment, resulting in a red shift and broadening of emission. Temperature-dependent emission for these samples are robust with an increase in thermal stability with increasing z, due to the large gap between $5d$ levels and the conduction band of the host. Increased thermal quenching resistance is observed with increasing z over a small range, and likely gives rise to the increased quantum yield due to the predicted high barrier for thermal ionization

that increases with increasing z. The present work provides experimental verification of optical properties resulting from an increase in the polyhedral distortion of the Eu^{2+} activator site with increasing Al/O content, as well as enhanced thermal stability due to a large thermal ionization barrier. Our work illustrates that structurally tuning the host lattice at low concentrations can be leveraged to optimize the optical and thermal performance of this important inorganic phosphor.

Chapter 4

Microwave preparation and spark plasma sintering of monolithic $BaMgAl_{10}O_{17}:Eu^{2+}$ phosphors for solid state lighting

With high power light emitting diodes (LEDs) and laser diodes (LDs) being explored for white light generation and visible light communication, thermally

[1]The contents of this chapter have substantially appeared in Reference [96]: C. Cozzan, M. J. Brady, N. O'Dea, E. E. Levin, S. Nakamura, S. P. DenBaars, and R. Seshadri, Monolithic translucent $BaMgAl_{10}O_{17}:Eu^{2+}$ phosphors for laser-driven solid state lighting, *AIP Adv.* **6** (2016) 105005.

robust encapsulation schemes for color-converting inorganic phosphors is essential. In the current work, the canonical blue-emitting phosphor, high purity Eu-doped $BaMgAl_{10}O_{17}$ (BAM:Eu^{2+}), has been prepared using microwave-assisted heating (25 min), densified into a ceramic phosphor using spark plasma sintering (30 min), resulting in translucent samples that emit blue light when incident with a UV laser diode.

4.1 Introduction

LED lighting is rapidly replacing incandescent and fluorescent sources,[10] and advances in semi polar and non polar substrates for LEDs have pushed current densities to beyond 1000 A/cm^2.[11] Although current densities are increasing, laser diodes (LDs) have peak efficiencies at much higher operating currents than LEDs and therefore offer a higher power alternative to the droop-limited LEDs.[12] Currently, both LEDs and LDs are being explored to generate white light using inorganic phosphors, with LDs showing promise for high power white lighting.[9, 21, 22] Two common strategies are utilized for white light generation. Either a blue LED or LD is used in conjunction with a yellow-converting inorganic phosphor to generate a cool white light, or a near-UV or violet LED or LD is used to excite a mixture of blue,

red, and green emitting inorganic phosphors to generate a warm white light.[2, 18] Additionally, recent advances in laser diodes has also enabled visible light communication.[97] Laser-based phosphor-converted white light for visible light communication has also been demonstrated, where 2 Gbit/s was demonstrated using a single crystal phosphor.[98] With high power laser-based systems for lighting applications, the high intensity light generated requires phosphor morphologies with high thermal conductivity to keep a low operating temperature of the phosphor and to combat self-heating due to Stokes loss.

One way to make phase pure materials in a fast and energy efficient way is through microwave assisted heating. In microwave assisted heating, starting oxides are mixed in stoichiometric ratios, placed in an alumina crucible that sits in a bed of activated charcoal with a lid to keep a slightly reducing atmosphere from the combustion of carbon to carbon monoxide, and placed in an insulating container.[19] This setup is placed in a conventional microwave and phase pure materials can be prepared in 25 min. This method is fast due to direct heating of the reactants, and reduces the reaction time of these samples by an order of magnitude.

Spark plasma sintering (SPS) is one method to achieve stand-alone dense and robust ceramics. SPS can be used to achieve near theoretical density in already prepared ceramic powders, with certain crystal structures

enabling translucent or transparent samples.[99] In SPS, powder is placed in a carbon-coated die set, a pressure is placed on the powder by two die presses, and a current is applied to the sample to achieve temperatures up to 1700 °C with fast ramp rates (>100 °C/min). SPS of the canonical yellow phosphor, Ce-doped yttrium aluminum garnet, has been previously explored.[100–102] In this cubic system, scattering is dominated by pores, and the reduction of pores by optimizing SPS parameters and utilizing nanoparticles results in transparent samples. In hexagonal phosphor systems, like Eu-doped $BaMgAl_{10}O_{17}$ (BAM:Eu^{2+}), the refractive index is anisotropic and therefore depends on orientation of the grains. This anisotropy leads to additional grain scattering versus cubic crystals, making hexagonal systems, such as α-Al_2O_3, translucent at best, and not transparent.[103]

In the current work, the canonical blue-emitting phosphor, BAM:Eu^{2+}, has been prepared phase pure using microwave assisted heating (25 min) and densified into translucent pellets using SPS (30 min). The emission properties of the initial powder and the translucent sample have been studied using both a xenon lamp and a violet LD. Results indicate promise for uses of this blue phosphor in laser-based applications.

4.2 Methods

Eu-substituted $BaMgAl_{10}O_{17}$ (BAM:Eu^{2+}) was prepared by thoroughly mixing and grinding stoichiometric amounts of the starting materials $BaCO_3$ (99.999%, Sigma-Aldrich), MgO (99.95%, Cerac), Al_2O_3 (99.99%, Sigma-Aldrich), and Eu_2O_3 (99.99%, Sigma-Aldrich). The europium substitution amounts were 0.5 atom %, 1.0 atom %, 1.5 atom %, 2.0 atom %, 2.5 atom %, and 3.0 atom %, meaning that the nominal composition for the highest performing sample, 1.5 atom %, was $Ba_{0.985}Eu_{0.015}MgAl_{10}O_{17}$. LiF (99.995%, Aldrich) and NH_4F ($\geq$99.99%, Sigma-Aldrich) were added in small amounts (5 wt % and 0.5 wt%, respectively) as flux.

The microwave heating procedure was based on prior work by Birkel *et al.*[19] For each preparation, 8 g of granular carbon (20 mesh from Sigma-Aldrich) was used as the microwave susceptor, and placed in a 20 mL alumina crucible (Advalue). Approximately 0.5 g of the unreacted sample powder was placed in a 5 mL alumina crucible. The 5 mL crucible was pushed into the carbon in the 20 mL crucible, covered with an alumina lid (Advalue), and placed in a block of high temperature alumina insulation foam. The materials were heated in a domestic microwave oven (Panasonic NN-SN667B, 1200 W) operating at 720 W for 25 min. This power and time were found to be

highly reproducible and yielded the most efficient phosphors in this study. Other combinations of power and time produced the desired phase, but with phosphor efficiencies that were lower than that measured for samples prepared at 720 W for 25 min.

High resolution synchrotron powder diffraction data were collected using beamline 11-BM at the Advanced Photon Source (APS), Argonne National Laboratory using an average wavelength of 0.459266 Å. Rietveld refinements were performed using the General Structure Analysis System (GSAS) with EXPGUI.[57, 58] Peak shapes were handled using the pseudo-Voigt profile function, which combines Gaussian and Lorentzian components. The background was handled using a Chebyshev polynomial. The refined structure was visualized using the open-source crystallographic software VESTA.[59]

Scanning electron microscopy (SEM) images were collected using a FEI XL30 Sirion FEG Digital Electron Scanning Microscope in secondary electron mode using a 15 kV beam voltage.

Room temperature photoluminescence spectra and quantum yield (QY) were measured using a fluorescence spectrometer (Horiba, Fluoromax 4). Phosphors were thoroughly mixed by 25-wt % in a silicone matrix (Momentive, RTV-615) using a high speed mixing system (FlackTek Inc., DAC 150.1 FVZ-K) at 1500

rpm for 5 min, and subsequently deposited on a 100 mm^2 fused silica substrate (Chemglass) and heated at 105 °C for 15 min in a box furnace to accelerate the curing process. Phosphors encapsulated in a silicone matrix were then placed in a 15 cm diameter, Spectralon®-coated integrating sphere (Horiba, Quanta-ϕ) and excited using light with a wavelength of 340 nm and 400 nm, which was generated by a 150 W continuous output, ozone-free xenon lamp. Photon counts are collected with an R928P red-sensitive photomultiplier (PMT) in photon counting mode, which is able to reject photon counts due to noise, while a calibrated photodiode reference detector corrects for intensity and temporal fluctuations in the source during scanning. Slit widths for the excitation and emission monochromaters were held constant at 1.5 nm, and a metallic neutral density filter of 1.5 and 2.0 Optical Density (Newport) was used to protect the PMT from exceeding 10^5 counts during excitation scans. QY was calculated based on the work by de Mello *et al*.[83]

Spark plasma sintering was performed on an FCT Systeme GmbH SPS furnace. Sample powders were placed in a graphite die of 10 mm diameter with 1 mm thick graphite foil. In SPS, the chamber holding the sample is pumped down to vacuum with a preload applied, with the force increased after vacuum is achieved. To achieve translucent BAM:Eu^{2+} samples, a preload of 3 kN was applied and increased to 5 kN once vacuum was achieved. A heating rate of

200 °C was then initiated. The sample was heated to 1500 °C at a rate of 200 °C/min, held for 5 min, and cooled to room temperature in 10 min. Samples were then sanded to remove the graphite foil.

To demonstrate viability with a LD, QY was calculated using a 60 cm integrating sphere with the laser mounted in a side port and the phosphor sample mounted in the center of the sphere. The sample surface was positioned at a slight angle from the incoming laser beam to prevent reflection back towards the laser port, and the distance between the laser and the sample was 30 cm. The commercially available laser diode, with $\lambda_{max} = 402$ nm, FWHM = 2.6 nm, threshold current of 30 mA, and wall plug efficiency (WPE) of 20%, was mounted in a copper heat sink. The diode was operated at 500 mA with a voltage of 6.11 V, controlled by a Keithley 2440 5A SourceMeter. A FLIR A310 thermal imaging camera was used to monitor the thermal management of samples. The samples were thermally isolated on quartz wool, and the laser diode mounted in a copper heat sink. The diode was placed 5 cm from the surface of the samples and operated at 500 mA with a voltage of 6.11 V.

4.3 Results and discussion

$BaMgAl_{10}O_{17}:Eu^{2+}$ crystallizes in the hexagonal space group $P6_3/mmc$ (no. 194).[104, 105] The refined X-ray diffraction pattern and crystal structure for $Ba_{0.985}Eu_{0.015}MgAl_{10}O_{17}$ are shown in Figure 5.4(a), with unit cell values shown in Table 4.1. No impurity phases were discovered or refined, and the R_{wp} of the fit is 11.75%. Ba and Eu occupancies were held constant at the nominal amounts. The U_{iso} values for Ba and Eu are larger, indicating the likelihood for site disorder. The geometric density of the pellet was measured as 3.45 g/cm^3 ($\pm$ 0.05), which is 91.5% of the theoretical density of 3.770 g/cm^3 calculated from the refined unit cell. The measured density is likely not due to the presence of pores at grain boundaries, but is due to the non-perfect arrangement of hexagonal grains of the BAM:Eu^{2+}. As shown in a representative SEM image (Figure 5.4(c)), there are regions of densely packed layers that are oriented in different angles relative to each other. This non-perfect stacking of hexagonal grains appears to create spacing in the stacks themselves, and is also likely the source of grain scattering that makes SPS samples of this material translucent and not transparent.

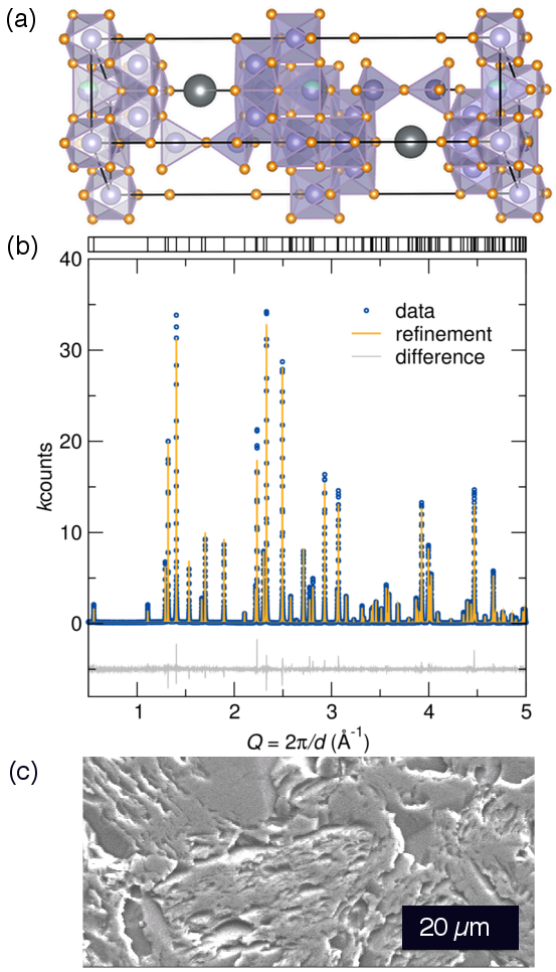

Figure 4.1: (a) Synchrotron X-ray diffraction refinement for $Ba_{0.985}Eu_{0.015}MgAl_{10}O_{17}$ ($R_{wp} = 11.75\%$) shows phase purity. The hexagonal structure is shown in (b), with Ba atoms charcoal, O atoms orange, Al atoms green, Mg atoms purple, and Al/Mg-O polyhedra purple. (c) SEM micrograph of the BAM:Eu^{2+} sample (black bar is 20 μm wide) showing the non-perfect arrangement of the hexagonal grains. This stacking leads to translucency in these materials, as well as a density of 91.5%.

The blue emitting phosphor $BaMgAl_{10}O_{17}:Eu^{2+}$ shows strong absorption in the UV, and emission centered around 445 nm (Figure 4.2(a)). The emission is due to the excited $4f^6 5d$ relaxing to the $4d^6$ ground state.[104] No emission is observed around 600 nm, which confirms the presence of Eu^{2+} in the lattice instead of Eu^{3+}, demonstrating the versatility of microwave assisted heating for preparing phosphor samples. QY of the starting powder was measured as a function of Eu mol % (Figure 4.2(b)). The maximum QY of 66 % ($\pm$ 5 %) for $\lambda_{ex} = 340$ nm was achieved for the 1.5 mol % sample. The Commission Internationale de l'Éclairage (CIE) 1931 (x, y) coordinates were (0.15, 0.05) for all samples measured.

To demonstrate potential for laser applications, the QY was measured using a commercial laser diode operating at 3 W, and a QY of 37 % ($\pm$ 5 %) was calculated. Photographs of a BAM:Eu^{2+} sample without and with a 402 nm LD incident to its surface is shown in Figure 4.3(a) and (b), respectively. The QY for $\lambda_{ex} = 400$ nm of the phase pure starting powder encapsulated in silicone was 33% ($\pm$ 5 %). The same QY within error was calculated using a xenon lamp and a LD, indicating that densification of the BAM:Eu^{2+} powder into a translucent does not serve to lower the QY. Additionally, the QY of the translucent sample will likely be higher with optimized starting materials.

In conclusion, phosphor powders were prepared using microwave-assisted

Table 4.1: Unit cell data obtained from Rietveld refinements of X-ray synchrotron diffraction data. Numbers in parenthesis indicate the error in refined values. Total occupancy of Ba and Eu was constrained to 1, the occupancy of Al2 and Mg1 was constrained to 1, and U_{iso} values for O were fixed at 0.005.

Cell a (Å)	5.623965(3)				
Cell b (Å)	5.623965				
Cell c (Å)	22.639717(22)				
Cell volume (Å^3)	620.1360(10)				
Space group	$P6_3/mmc$				
atom	x	y	z	Occupancy	U_{iso}
Ba	0.3333	0.6667	0.75	0.985	0.01414(8)
Eu	0.3333	0.6667	0.75	0.015	0.01414(8)
Al1	0.16593(6)	0.33186(11)	0.894445(21)	1	0.00126(11)
Al2	0.3333	0.6667	0.02414(4)	0.55(4)	0.00174(32)
Mg1	0.3333	0.6667	0.02414(4)	0.45(4)	0.00174(32)
Al3	0.3333	0.6667	0.174127(34	1	0.00143(18)
Al4	0	0	0	1	0.001
O1	0.1543	0.3086	0.0516	1	0.005
O2	0.5041	0.0082	0.1486	1	0.005
O3	0.3333	0.6667	-0.0588	1	0.005
O4	0	0	0.1441	1	0.005
O5	0.3333	0.6667	0.25	1	0.005

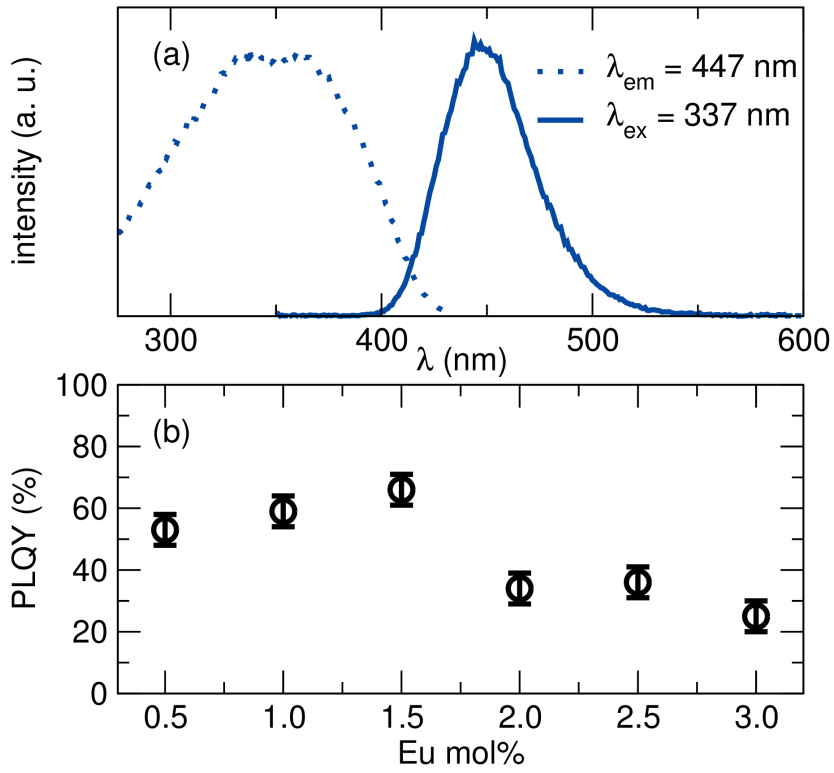

Figure 4.2: (a) Excitation (dashed) and emission profile of $Ba_{0.985}Eu_{0.015}MgAl_{10}O_{17}$ show strong absorption in the UV and blue emission due to the allowed 5*d* to 4*f* transition in Eu^{2+}. (b) QY as a function of Eu mol-% shows max QY = 66% for 1.5 mol-% Eu nominally Error bars are ± 5%.

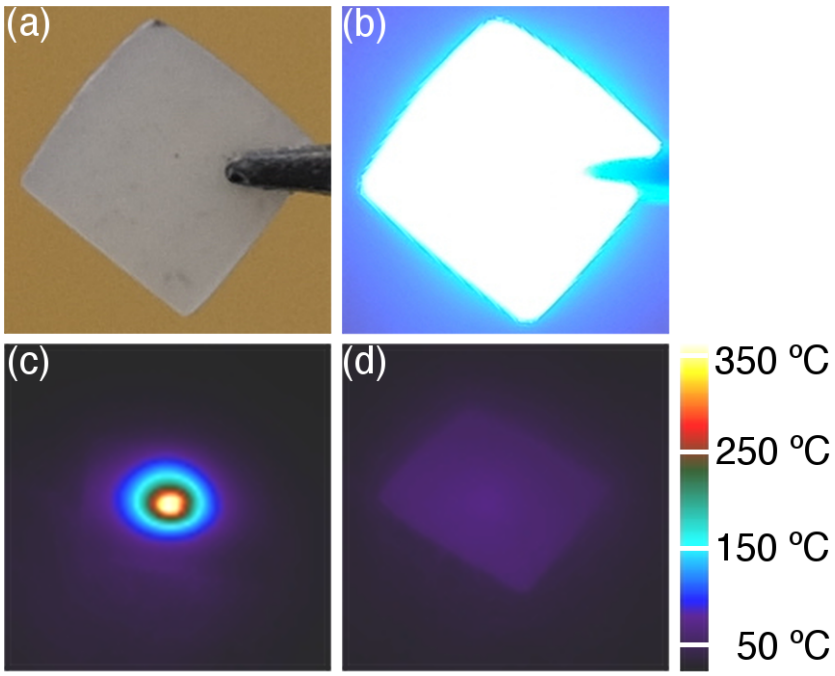

Figure 4.3: Photograph of (a) translucent BAM:Eu^{2+} sample held by carbon-tipped tweezers, and (b) the same translucent BAM:Eu^{2+} excited by a 402 nm laser diode incident perpendicular to the surface of the sample. The translucent sample under laser excitation after 11 s (c) only reaches 67 °C, whereas (d) the phosphor powder in silicone exceeds 360 °C and burns in the same time.

heating in 25 min, which reduces preparation time and energy consumption. Results of the refinement on synchrotron X-ray diffraction data demonstrate the viability of microwave assisted heating for preparation of phase pure $BaMgAl_{10}O_{17}:Eu^{2+}$. Phosphor powders were then densified into opaque or translucent dense ceramics using SPS in 30 min, with a heating rate of 200 °C to a temperature of 1500 °C for a 5 min hold. QY of the starting powder does not change from after densification into a translucent sample, and could likely be improved using optimized starting powders. Due to the monolithic nature of the present blue-emitting phosphor, translucent phosphors prepared in this way are useful as a blue component in warm white light generation using LDs for general illumination and visible light communication.

Chapter 5

Stable, heat conducting phosphor composites for high-power laser lighting

Solid-state lighting using laser diodes is an exciting new development that requires new phosphor geometries to handle the greater light fluxes involved. The greater flux from the source results in more conversion and therefore more conversion loss in the phosphor, which generates self-heating, surpassing

[1]The contents of this chapter have substantially appeared in Reference [96]: C. Cozzan, G. Lheureaux, N. O'Dea, E. E. Levin, J. Graser, T. D. Sparks, S. Nakamura, S. P. DenBaars, C. Weisbuch, and R. Seshadri, Stable, heat conducting phosphor composites for high-power laser lighting, *ACS Appl. Mater. Interfaces* **10** (2018) 5673–5681.

the stability of current encapsulation strategies used for light-emitting diodes, usually based on silicones. Here we present a rapid method using spark plasma sintering (SPS) for preparing ceramic phosphor composites of the canonical yellow-emitting phosphor Ce-doped yttrium aluminum garnet (Ce:YAG) combined with a chemically compatible and thermally stable oxide, α-Al_2O_3. SPS allows for compositional modulation, and phase fraction, microstructure, and luminescent properties of ceramic composites with varying compositions are studied here in detail. The relationship between density, thermal conductivity, and temperature rise during laser-driven phosphor conversion is elucidated, showing that only modest densities are required to mitigate thermal quenching in phosphor composites. Additionally, the scattering nature of the ceramic composites makes them ideal candidates for laser-driven white lighting in reflection mode, where Lambertian scattering of blue light offers great color uniformity and a luminous flux $>$1000 lumens is generated using a single commercial LD coupled to a single phosphor element.

5.1 Introduction

Solid state white lighting is more efficient than traditional sources and is currently experiencing increasing rates of adoption due to improvements in

color quality and luminaire design. For high power lighting (>100,000 lumens) using light emitting diodes (LEDs), many diodes are required to produce high light output to avoid droop,[13] resulting in a luminaire with a very large footprint. Directional lighting using LEDs is limited by the emission angle for the emitter, requiring secondary optics that diminish the total light produced. To circumvent these technological and fundamental limits, laser diodes (LDs) provide a promising path forward owing to their monochromatic, highly coherent, and directional light emission.[12] LDs coupled to small inorganic phosphors allow very high luminous flux for a given solid state emitter,[9] and the small laser spot size can result in a quasi-point source of white light with a smaller étendue compared to conventional LED systems. New technologies, such as laser-boosted headlights[32] and visible light communication[97, 98, 106] have leveraged the benefits of LDs over LEDs. In these emerging demonstrations, a monochromatic LD is converted to broad band emission using inorganic phosphors. A key design requirement is the development of phosphor morphologies capable of withstanding high conversion and therefore high thermal loading due to the higher fluence from LDs.[96]

Despite impressive recent improvements in monochromatic LEDs and LDs, inorganic phosphors will likely always have a role in solid-state white lighting due to their ease to manufacture,[19] low cost compared to solid-state

emitters, high efficiencies,[2] and well-studied emission and color stability with temperature. Thermal stability of phosphor emission is dictated by the crystal structure and the dopant concentration.[92] Lower efficiencies are observed at elevated temperatures for a given dopant concentration due to thermal quenching, and more quenching is observed as dopant amount in a phosphor is increased for a given temperature.[5] For example, the widely used yellow-emitting Ce-doped yttrium aluminum garnet (YAG) phosphor quenches at high temperatures partially due to thermal ionization,[95] which adds to heat generated via the Stokes shift.[2] These mechanisms raise the phosphor temperature and degrade efficiency and color stability. LED phosphor encapsulation schemes impact the thermal conductivity of the phosphor element, such as an epoxy resin, silicone, or glass, that is mixed with the phosphor and then cured.[25] Therefore, to mitigate thermal quenching, the phosphor morphology used must have enough thermal conductivity to dissipate heat generated from conversion.

Many new strategies have been explored to improve the thermal conductivity of phosphor encapsulation schemes. Phosphor-in-glass, or the mixture of phosphor powders with glass frit at low temperatures, is reported to display higher thermal conductivity to 2.18 W/(m·K), but reflection losses of the excitation light led to a lower luminous efficacy than in silicone-based

commercial white LEDs.[25, 107] Thermally robust phosphors can be achieved by avoiding low thermal conductivity encapsulating materials altogether to create stand-alone phosphor monoliths, such as single crystals[29] or dense monolithic or composite ceramics[40, 102, 108, 109] and have been successfully deployed in industry.[33] When compared to phosphors in silicone, polycrystalline ceramics offer control of light scattering via pore size and compositional tuning, reduced degradation, reduced color over angle shift, can be characterized before use with LEDs, and offer better heat conduction.[31] In addition to monolithic phosphor ceramics, phosphor composites (phosphors or multiple phosphors with heat dissipating materials) offer design flexibility.

In the present work, a series of Ce:YAG and α-Al_2O_3 composites were made using spark plasma sintering (SPS) and their phase fraction, microstructure, and luminescent properties ew studied for use in LD-based white lighting. Both transparent and scattering YAG[100–102] and YAG composites[37, 38, 109–112] have been studied previously for white light generation, the latter offering increased thermal conductivity and increased light extraction through the inclusion of alumina, which has a thermal conductivity three times that of YAG. For the first time, relationships between ceramic density, thermal conductivity, and operating temperature are investigated and reveal that large differences in thermal conductivity as a function of Al_2O_3 do not

translate to significantly lower operating temperatures for the system design studied presently. Unique experimental insights into the relationship between density, thermal conductivity, and operating temperature demonstrate that encapsulation-free composites of modest density do not sacrifice light output ($>$1000 lm for one phosphor and one LD) with naturally Lambertian scattering of incoming laser light rendering a more uniform white light. Additionally, the composites sufficiently mitigate thermal quenching and are superior to ceramics containing no alumina, offering high light output and excellent color uniformity with no additional preparation.

5.2 Methods

Mixtures of commercially available Ce-doped yttrium aluminum garnet ($Y_3Al_5O_{12}$:Ce^{3+} or Ce:YAG) and alpha phase alumina (α-Al_2O_3 average particle size of 0.71 μm, Materion, 99.9%) were prepared via mixing with an agate mortar and pestle with care taken to mix and not grind the powders, in the following amounts: 25%, 50%, 75%, and 100% by weight Ce:YAG respectively. Samples were densified using the spark plasma sintering technique in an FCT Systeme GmbH SPS furnace. Powders were placed in a graphite die of 10 mm diameter with 1 mm thick gcellraphite foil lining the die. The sample chamber

was pumped down to vacuum with a preload of 3 kN applied, and subsequently increased to 5 kN or 8 kN over 30 s once vacuum was achieved. The sample was heated up to 1200–1500° C at a rate of 200° C/min with a 5 min hold, and then finally cooled to room temperature in over 10 min. The resulting samples were then sanded to remove the graphite foil. The maximum temperature was increased with increasing Ce:YAG content as Ce:YAG was observed to densify at a higher temperature than the Al_2O_3.

Sintered samples were annealed using a Lindberg tube furnace with an alumina tube under 0.1 L/min of 5% H_2:95% Ar with the following heating regimen; a 2 °C/min heating to 1500 °C, 24 h at 1500 °C, and finally a 2 °C/min cool to room temperature. Geometric density was measured before and after annealing by weighing the samples and measuring their dimensions using a micrometer. Density of the samples was not altered by the annealing step. Qualitative information on carbon concentration as a function of depth was obtained using secondary ion mass spectrometry (SIMS). SIMS was performed on a Cameca IMS-7f Auto system using Cs primary ions. A gold coat and electron flood were used to control electrical charging effects. In each sample, three 100 μm craters were made, and secondary ions were collected from the center 33 μm. The etch rate was approximately 65 nm/min, and composition down to a depth of 2500 nm to 3000 nm was investigated. Aluminum ions (^{27}Al) were

collected in addition to carbon, for purposes of normalizing the carbon results across samples.

X-ray powder diffraction was performed at room temperature using a Panalytical Empyrean powder diffractometer with Cu $K\alpha$ radiation. Starting materials and powder from grinding sintered samples with an agate mortar and pestle were was placed on a zero background silicon holder and scanned for an 1 h in duration. Rietveld refinement of the diffraction data was performed using the General Structure Analysis System (GSAS) with EXPGUI.[57, 58] Scanning electron microscopy (SEM) images of the sintered samples were collected using a FEI XL30 Sirion FEG Scanning Electron Microscope using a backscattered electron detector for compositional contrast with a 15 kV beam voltage.

Photoluminescence spectra were collected using a 50 cm diameter integrating sphere with a commercial blue laser diode in a copper heat sink mounted in a side port and the phosphor sample mounted in the center of the sphere. The diode was controlled by a Keithley 2440 5A SourceMeter. Data were collected using a MAS40 spectrometer with a 2.0 OD filter. A correction factor was experimentally measured to account for the attenuation imparted by the filter. Quantum yield (QY) was calculated using a two measurement approach.[113] To mitigate sample heating for phosphor powders measured in silicone, a 1.0 OD filter was placed in front of the LD to attenuate the LD

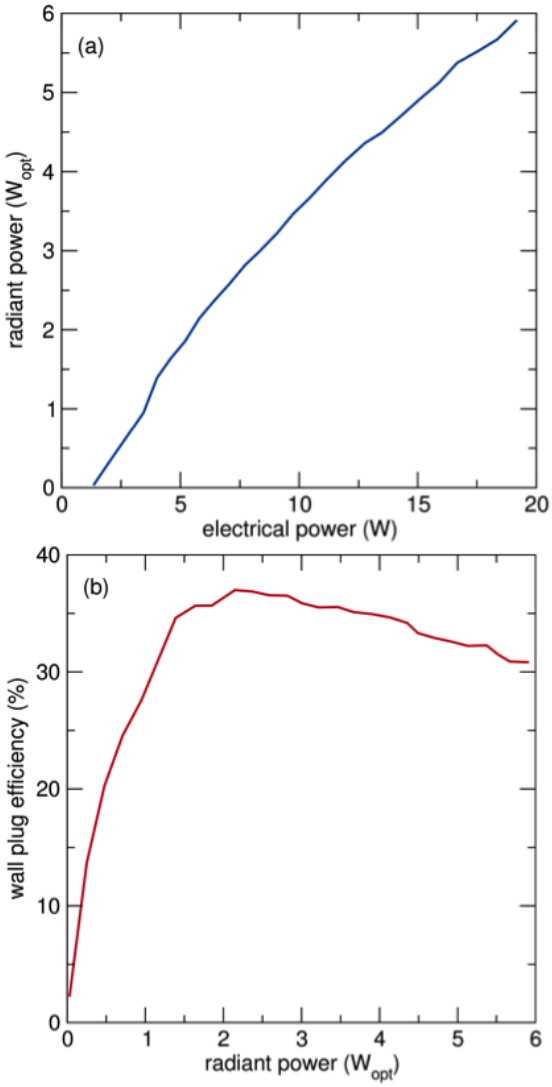

Figure 5.1: (a) Laser radiant power (W) versus electrical power (W) and (b) laser wall plug efficiency (%) as a function of radiant power (W) shown right for the commercial laser diodes employed in the present work. © 2018 American Chemical Society.

light. No filter was required for ceramic samples. The data collected was then used to calculate optical properties, such as quantum yield and luminous flux, using Mathematica. Current, voltage, radiometric, and electrical power used to calculate wall plug efficiency (WPE) for the LD used is shown in Figure 5.1. For phosphors measured in silicone, phosphor powders were thoroughly mixed at 25 wt% in a silicone matrix (Momentive, RTV-615) using a high speed mixing system (FlackTek Inc., DAC 150.1 FVZ-K) at 1500 rpm for 5 min and subsequently deposited on a 100 mm^2 fused silica substrate and heated at 398 K for 15 min in a box furnace to accelerate the curing process.

Using the same commercial LD, samples were placed on a large aluminum heat sink and monitored using a FLIR A310 thermal imaging camera with range 0° C–360° C. The LD lens was placed 5 cm away from the surface of samples at an angle of 45 °. The LD was mounted in a cylindrical copper heat sink of diameter 20 mm to mitigate laser overheating. The samples were placed on a large metal heatsink that was much larger in volume than the sample and thermally attached using a silicone-based thermal joint compound. The samples were then monitored using an infrared (IR) camera. Emissivity of the samples was set to 0.95 to obtain the temperature from IR camera images.

Thermal diffusivity was measured using the laser flash technique between room temperature and 973 K under an argon atmosphere on a Netzsch LFA

457 system with a flow rate of 100 ml/min. Pellets for the measurement, approximately 6 mm in diameter and 2 mm thick, were sprayed with a layer of carbon paint to minimize errors in the emissivity. Heat capacity was calculated using a Netzsch DSC 3500. The samples were run from 273 K to 773 K and back under nitrogen gas. The energy required to heat the samples were compared to a sapphire standard using a inbuilt ratio method. The thermal conductivity was calculated using $\kappa = \alpha C_p \rho$, where α, C_p, and ρ are the thermal diffusivity, heat capacity, and density, respectively.

To characterize reflection of incoming laser light and analyze the color uniformity, angular resolved experiments were carried out on a home-built system. A commercial LD was mounted and used to excite samples at an incident angle of 30 °. Samples were placed on a heat sink while a an optical fiber attached to a mechanical arm scanned angles from 0 ° to 90 °. Light was collected using an optical fiber connected to a Horiba Jobin Yvon Spex 550 Triple Imaging Axial spectrometer.

5.3 Results and discussion

Ceramic phosphor composites of Ce:YAG and Al_2O_3 in different ratios by weight were prepared by mixing and densifying powders using SPS. SPS

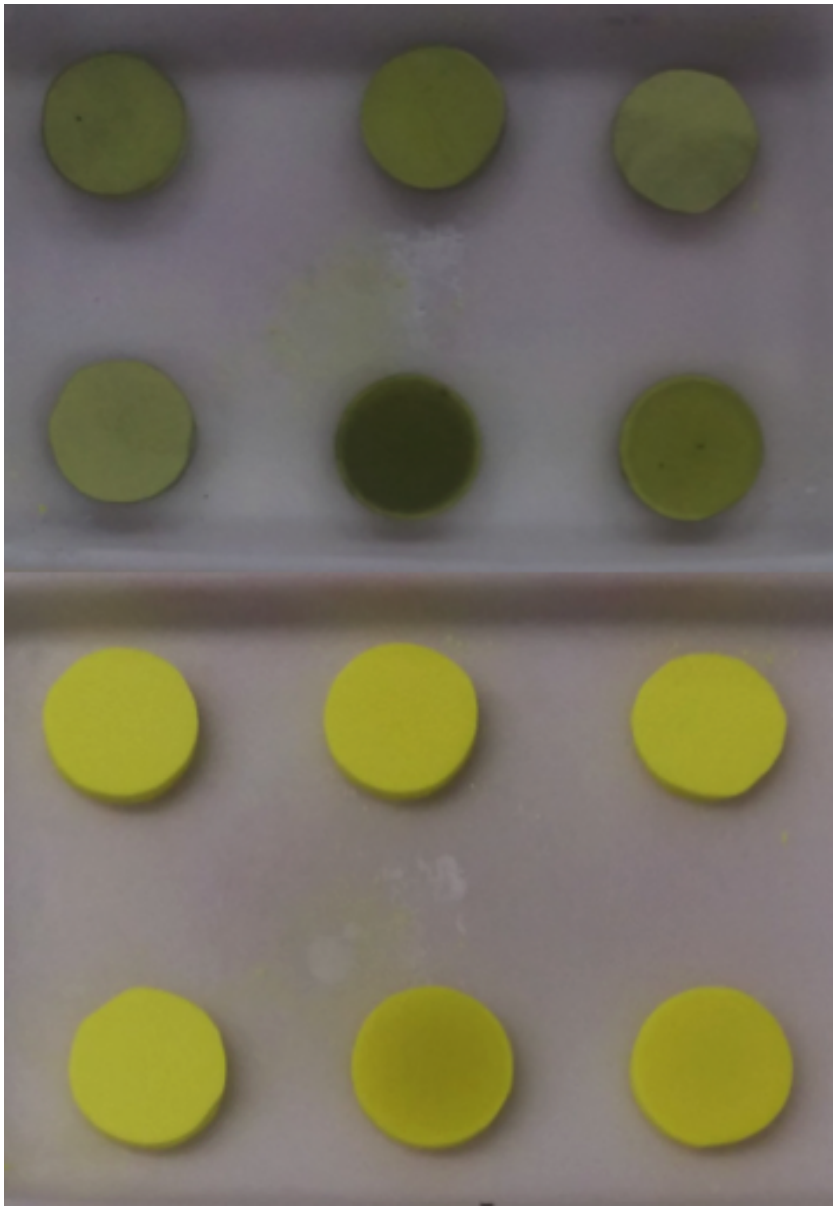

Figure 5.2: Photographs of samples after spark plasma sintering and removing the graphite foil (top), followed by a subsequent annealing step (bottom) of 2 °C/min to 1500 °C for 24 h with a 2 °C/min cool to room temperature. Sample density was not altered by the annealing step. © 2018 American Chemical Society.

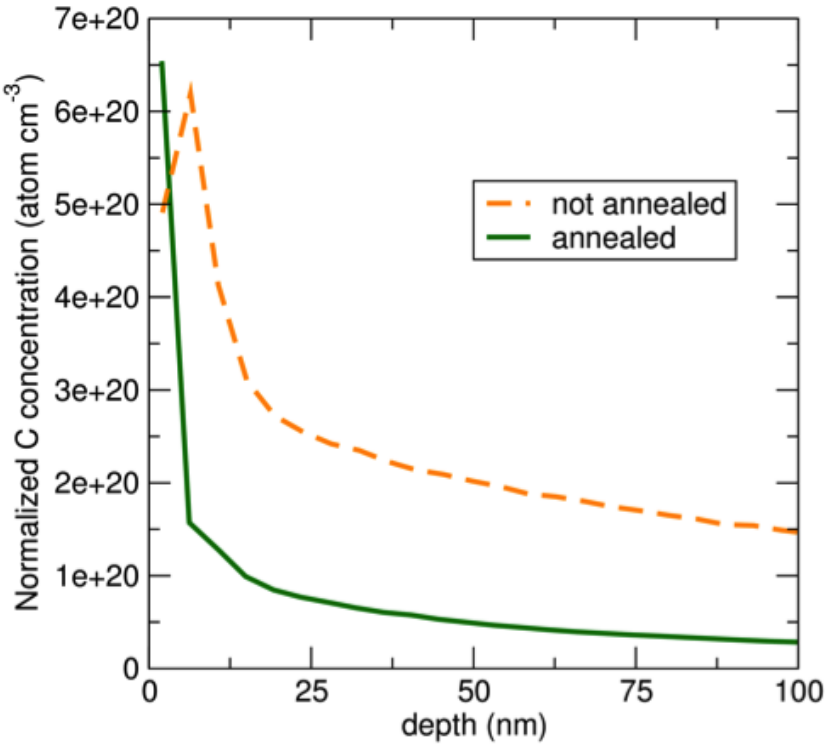

Figure 5.3: Qualitative SIMS data shows higher levels of carbon for the not annealed sample. SIMS ionization efficiency for an arbitrary system were used to estimate absolute carbon concentration. However, carbon still exists in the annealed sample. Removing carbon in future processing will therefore increase efficiency. © 2018 American Chemical Society.

relies on graphite and carbon-based tooling surrounding the powder, resulting in a carbon-rich densification environment. After densification, the samples appeared dark in color due to the presence of carbon instead of yellow Ce:YAG and white Al_2O_3. Carbon contamination in SPS-prepared transparent oxides was observed by others, evidenced by lower in-line transmission.[114] The densified ceramics in the present work were then subjected to an annealing step in a reducing atmosphere of 0.1 L/min of 5% H_2:95% Ar for 6 h at 1500° C on an alumina crucible in an alumina tube furnace. It was hypothesized that heating in a reducing environment would mitigate carbon contamination as hydrogen is an effective etching gas for carbon.[115] Visually, the samples appeared closer to the color of the original starting powders after the annealing step (Figure 5.2). To investigate the effect of the annealing step on the amount of carbon in the ceramics, SIMS was performed on three craters 3 μm to 4 μm deeper than the surface of the samples, with areas of approximately 30 mm^2 assessed. Using ^{27}Al as a reference signal, it was confirmed by SIMS that an order of magnitude less carbon was present in the annealed sample than in the as-prepared by SPS with no anneal (Figure 5.3). All further investigations in the present work were performed on annealed ceramic samples.

No intermediate phases are expected when mixing and heating Ce:YAG ($Y_3Al_5O_{12}$) and Al_2O_3 to 1500 °C, as evidenced by the α-Al_2O_3 and Y_2O_3 phase

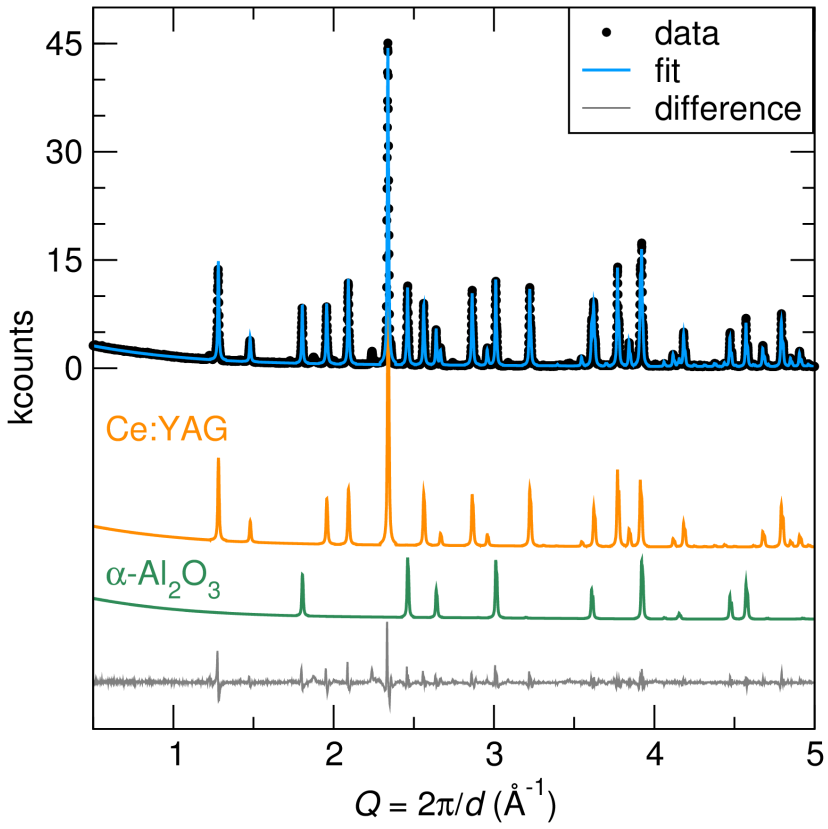

Figure 5.4: Rietveld refinement of powder from an SPS-prepared 50% Ce:YAG nominally by weight composite sample is shown with the components of Ce:YAG and α-Al_2O_3 displayed beneath. Results of the refinements indicate phase fractions of 48.6% Ce:YAG and 51.4% Al_2O_3, providing evidence to the compatibility of the two materials. © 2018 American Chemical Society.

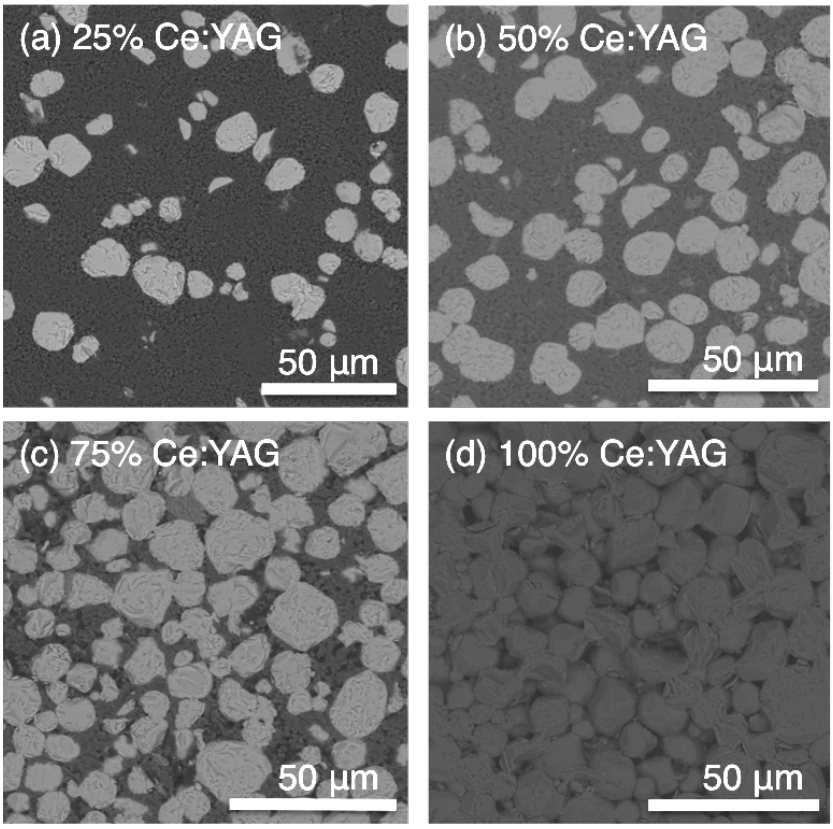

Figure 5.5: Backscattered SEM images show compositional contrast with lighter Ce:YAG and darker α-Al_2O_3 for the 25% (a), 50% (b), 75% (c), and 100% (d) Ce:YAG samples. Composite microstructures show Ce:YAG particles surrounded by a connected network of α-Al_2O_3. © 2018 American Chemical Society.

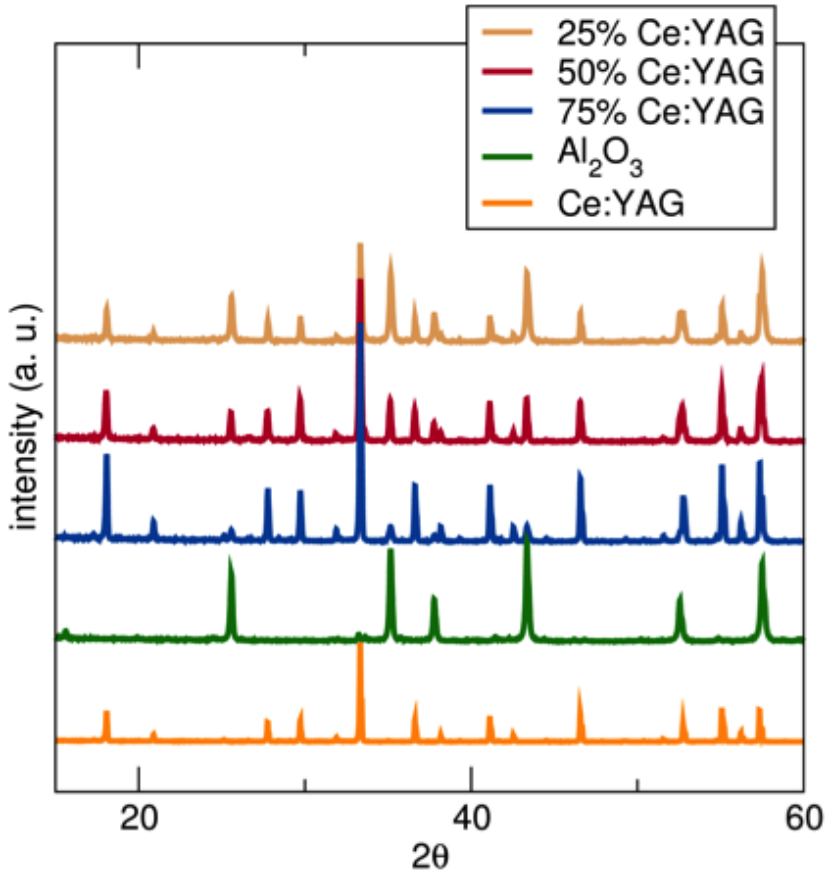

Figure 5.6: X-ray diffraction patterns of Ce:YAG, Al_2O_3, and 25% Ce:YAG, 50% Ce:YAG, and 75% Ce:YAG ceramic composites are shown. No intermediate phases were observed. © 2018 American Chemical Society.

Table 5.1: Refined unit cell parameters for the 50wt% Ce:YAG ceramic composite.

$Y_3Al_5O_{12}$ (YAG)	α-Al_2O_3 (corundum)	
Cell length a	12.01660(8)	4.76093(7)
Cell length b	12.0166	4.760937
Cell length c	12.0166	13.0037(4)
Cell angleα (°)	90	90
Cell angle β (°)	90	90
Cell angle γ (°)	90	120
Cell volume (Å^3)	1735.180(35)	255.260(7)
Symmetry	cubic	trigonal
Space group	Ia$\bar{3}$d	R$\bar{3}$c

Table 5.2: Refined atomic positions for the 50% Ce:YAG ceramic composite.

x‘	y	z	U_{iso}	
YAG				
Al1	0	0	0	0.005
Al2	0.375	0	0.25	0.005
Y1	0.125	0	0.25	0.005
O1	-0.03205	0.05414	0.15075	0.005
α-Al_2O_3				
Al1	0	0	0.35216	0.00393
O1	0.3061	0	0.25	0.00418

diagram.[116] To confirm the purity of phases in the sintered ceramics, X-ray diffraction was performed on powder derived from grinding an SPS-prepared ceramic sample (25% Ce:YAG and 75% Ce:YAG shown in Figure 5.6). Rietveld refinements of a representative 50% Ce:YAG ceramic ground into a powder (Figure 5.4) were used to obtain phase fractions, which were calculated to be 51.4% Al_2O_3 and 48.6% Ce:YAG. A table of refined unit cell parameters and refined atomic positions are shown in the Supporting Information in Table 5.1 and Table 5.2, respectively. The compatibility of $Y_3Al_5O_{12}$ and Al_2O_3 was also observed using SEM, where micrographs show Ce:YAG particles ($\sim$50 μm) distributed in an Al_2O_3 (0.71 μm) matrix (Figure 5.5). The particles of Ce:YAG isolated in the α-Al_2O_3 matrix suggest implications for both light scattering and thermal conductivity that will be discussed in more detail later in the present work. In Ce:YAG/Al_2O_3 phosphor systems, it has been noted that the refractive indices of YAG and Al_2O_3 are similar, potentially reducing backscattering and total internal reflection losses at crystal boundaries as an increased optical path enables more efficient excitation.[117] Additionally, higher thermal stability during conversion is also expected due to this morphology,[40] as the connectivity of the Al_2O_3 offers a percolating pathway for heat dissipation from Ce:YAG particles through the higher thermal conductivity of α-Al_2O_3.

Emission properties for samples with varying wt% Ce:YAG were measured

Table 5.3: Coordinated color temperature (CCT), Commission Internationale de l'Éclairage (CIE) (x, y) coordinates, and color rendering index (CRI) of ceramic composites prepared using SPS with systematically increasing amounts of Ce-doped YAG phosphor. The 50% Ce:YAG ceramic shows CIE coordinates closest to the white point with lowest CCT.

	25%	50%	75%	100%
CCT (K)	12399	5340	6760	5872
CIE (x, y)	(0.29, 0.25)	(0.34, 0.32)	(0.32, 0.28)	(0.33, 0.31)
CRI	63	61	63	63

using an integrating sphere and a commercial laser diode and are reported in Table 5.3. In the present work, ceramic samples of 50% Ce:YAG measured the lowest coordinated color temperature (CCT), Commission Internationale de l'Éclairage (CIE) coordinates closest to the white point, and relatively low CRI that is to be expected for a blue LD source coupled with a yellow-emitting phosphor.[9, 21] The LD was controlled using a Keithley 2440 power source with the LD operating at low power for $<$1000 ms to avoid sample heating. Small differences in the emission color of the ceramic phosphors did not follow any systematic trends. Recent work on Ce:YAG/Al_2O_3 ceramics observed systematic blue-shifted emission as the amount of α-Al_2O_3 was increased.[112]

It is therefore possible that the addition of α-Al_2O_3 mitigates the effects of reabsorption of the scattered blue light, resulting in blue-shifted emission with increasing α-Al_2O_3 content. However, this was not observed with consistency in the current work. Alternatively, as more α-Al_2O_3 is added to the system, less blue incident light is absorbed which may also result in the blue shift in emission. Therefore, it is difficult to conclude with confidence if differences in the emission spectra of 1-2 nm are due to the experimental setup or due to changes in light propagation as a function of α-Al_2O_3 content. As seen in the present work and in work by others,[112] white light near the white point (0.33, 0.33) can be achieved with 50% Ce:YAG samples. For these ceramics to be viable white lighting devices, both color and efficiency must be considered, and the theoretical limit of phosphor quantum yield must be understood. Reported external quantum efficiencies in these systems are less than the Ce:YAG powder by itself,[40] possibly due to low extraction in the ceramics.

For transparent Ce:YAG ceramics, the quantum efficiency of the transparent ceramics were reported to be lower than Ce:YAG powder due to waveguiding and backward emission losses.[118] In translucent or scattering Ce:YAG ceramics however, pores introduce scattering and can be controlled by tuning both the pore size and the prevalence of pores.[36] This scattering can overcome light trapping effects of the high index (n=1.85 at 450 nm) in Ce:YAG.[119] In

Table 5.4: PLQY measured for commercial Ce:YAG, a mixture of 50% Al_2O_3/50% Ce:YAG by weight, a 50% Ce:YAG ceramic, and powder achieved from grinding a 50% Ce:YAG ceramic. QY shows an initial drop from mixing with α-Al_2O_3, and a further drop in QY after SPS processing, due largely in part to the presence of carbon.

Sample	PLQY (%)	CIE (x, y)
Commercial Ce:YAG	*83–89	(0.33, 0.35)
50%Al_2O_3/50% Ce:YAG starting powders	*77–86	(0.27, 0.19)
50% Ce:YAG ceramic	*69–75	(0.29, 0.27)
97% theoretical density	48–53	

*indicates sample in silicone

the present work, scattering is introduced both through the grain boundaries of the hexagonal Al_2O_3 mixing with cubic Ce:YAG, as well as the presence of pores. QY was measured for ceramic samples as-prepared using SPS, and the SPS samples were then ground into powders and mixed in silicone and measured. Curiously, the measured QY of the powders in silicone derived from grinding the ceramics (69-75%) was higher than the ceramics prior to grinding (48-53%), which could be due to increased extraction by using silicone due to different indices of refraction or an increase in the probability for reabsorption in the silicone sample.

In the present work, phosphor mixtures were investigated both prior to SPS and post SPS preparation to determine if the drop in photoluminescent quantum yield (PLQY) is due to processing. For the starting Ce:YAG powder, the PLQY of the commercial Ce:YAG in silicone was measured to be 83–89%, which matches expected values for this particular phosphor. A sample of 50% by weight Ce:YAG and 50% by weight Al_2O_3 in silicone measured a small drop in the PLQY to 77–86 % (Table 5.4). PLQY was measured using an integrating sphere setup reported elsewhere,[9] where the ranges reported presently are minimum and maximum values measured for a range of laser powers tested. In the current work, conclusions about PLQY across the range of ceramic samples prepared are difficult to make as the samples contain qualitative but not quantifiable

amounts of carbon, which is known to absorb light.[120, 121] Quantitative values for carbon concentration in the present samples are also very difficult as oxide and carbon standards for these ceramic oxides do not exist at the time of publication for methods such as SIMS. While the potential interplay between PLQY and density are difficult to elucidate in the present work, it is clear that SPS processing in a carbon rich atmosphere introduces carbon that lowers the PLQY of the composite ceramic phosphors. Future work is needed to decrease the presence of carbon to increase the PLQY.

The increase in extraction by encapsulating the phosphor powder in silicone might also provide some reasoning as to the lower QY observed in the ceramics than the original powder, as some light might scatter but not escape the ceramic. However, the drop in QY observed is due largely to the carbon introduced via the SPS process. Other methods for preparation of ceramics, such as tape casting[122] and floating zone growth[117], might provide a more viable route for higher purity ceramic phosphors in the future, and ceramics with higher QY values have been reported for Al_2O_3/Ce:YAG samples.[40] The rest of the current work will instead focus on the viability of this system for use in high power white lighting, with the knowledge that improvements in QY are possible via cleaner processing routes and more efficient starting phosphors.

The luminous flux (Φ_{lum}) is the light power of a white light emitting device

as perceived by the human eye, and is given as follows (Eq. 5.1):

$$\Phi_{\mathrm{lum}} = 683\frac{\mathrm{lm}}{\mathrm{W}}\int_{\lambda} V(\lambda)S(\lambda)d\lambda \tag{5.1}$$

where 683 lm/W is a normalization factor representing the amount of lumens (lm) given by a light source of 1 W emitting at 555 nm, $S(\lambda)$ is the power spectral distribution measured experimentally, and $V(\lambda)$ is the eye response function which represents the intensity of color perception. One lumen is equal to a light source emitting one candela uniformly across a solid angle of one steradian. Therefore, luminous flux is the perceived total light output for a given emitter and phosphor combination or device and does not contain any information about the color of the light, just the intensity as perceived by the human eye. The luminous efficacy of radiation (LER), which is the luminous flux divided by the radiometric/optical power of the source (lm/W_{rad}), provides information about how efficiently visible light is produced by a given source. This is the upper limit measurement for a given light source and phosphor combination, whereas the overall luminous efficiency, calculated by dividing the flux by the electrical power of the solid state emitter, provides a measure of the actual device efficiency for producing light. Luminous efficiency is measured in lm/ W_{elec}, and in the case of LED or LD based devices, is dictated by both

the efficiency of electricity to light conversion (wall plug efficiency or WPE) and the efficiency of the phosphor. For comparison, compact fluorescent light bulbs and fluorescent light tubes have luminous efficiencies around 50 lm/W_{elec} to 80 lm/W_{elec}.[6]

Photopic parameters of the scattering Al_2O_3/Ce:YAG ceramics were measured as a function of radiometric laser power. In Figure 5.7, spectral power (mW/nm) of a 50% Ce:YAG ceramic is shown as a function of wavelength for different input powers of the blue LD. The spectral power reaches nearly 17 mW/nm for phosphor emission, which is a factor of twenty increase from earlier examples of LD-excited Ce:YAG for lighting.[21] Increases in spectral power observed in the present work are due to both higher performing lasers and thermally stable phosphor morphologies capable of withstanding high flux. At the maximum measured LD output power of 6.82 W, ~1.2 klm of white light was measured using an integrating sphere. Using only one phosphor sample and one commercial LD operating at maximum laser power, the 1.2 klm white light has a luminous efficacy of 165 lm/W_{rad} with a CRI of 65, CCT of 5350 K, and CIE coordinates of (0.34, 0.32). The luminous efficiency was measured to be 51 lm/W_{elec} using a 28% WPE LD. The most efficiency 50% Ce:YAG sample with measured density of 80% theoretical was PLQY=70%. These luminous flux values are generally better than what is reported for the best single chip

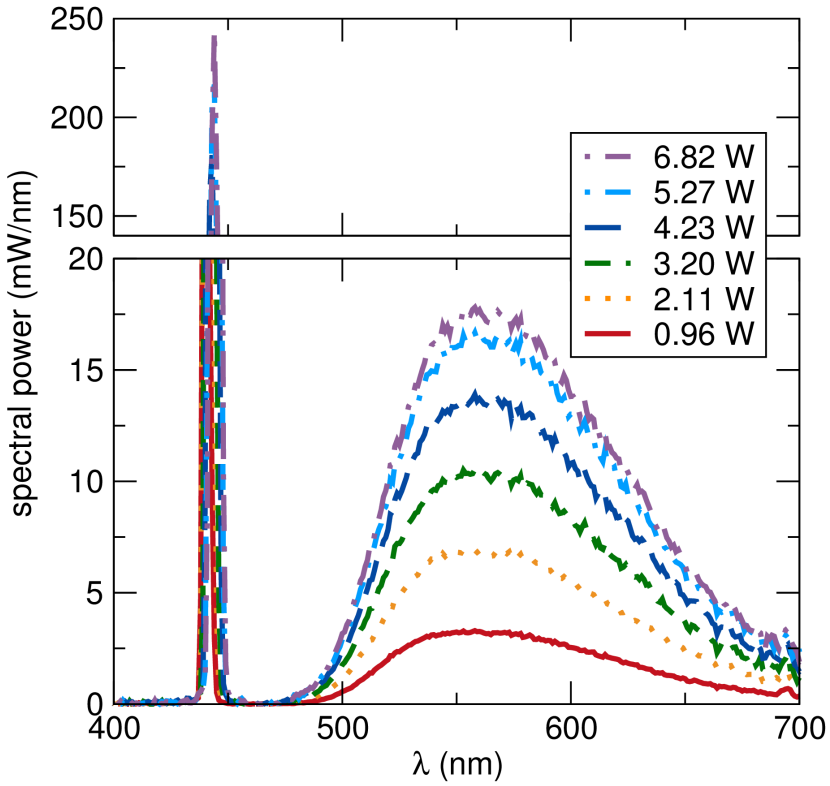

Figure 5.7: Spectral power distribution for increasing LD radiometric power for white light created when a 450 nm LD is incident a 50% Ce:YAG ceramic. White light is generated regardless of laser power, $(0.34, 0.33)$ for $0.92\,W_{rad}$ and $(0.34, 0.32)$ for $6.82\,W_{rad}$. © 2018 American Chemical Society.

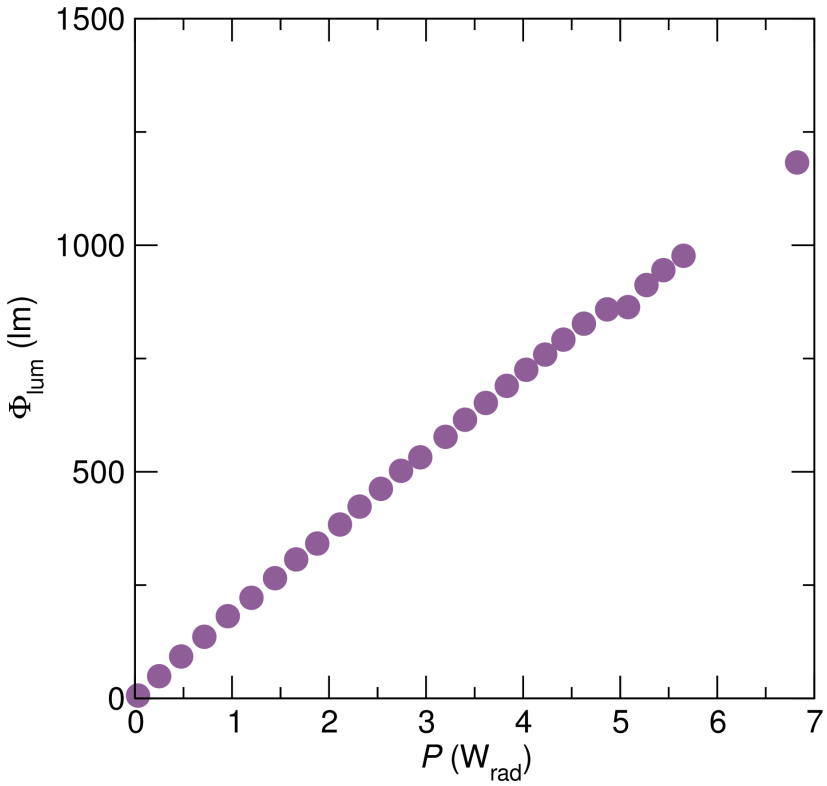

Figure 5.8: Luminous flux (Φ_{lum}) as a function of LD power for a 50% Ce:YAG ceramic, where a Φ_{lum} of 1.2 klm is observed at 6.82 W_{rad}. © 2018 American Chemical Society.

LEDs under normal operating conditions. The present demonstrations show that more than 1000 lm of white light can be produced by a single phosphor and a single solid state emitter. Since the above measurements were made with excitations $<$1 s, thermal management of the phosphors during operation must first be considered to understand feasibility for steady-state at high power. Additionally, it follows there is potential for increasing luminous flux via using multiple lasers for excitation, where thermal management is critical as roughly 25% of power is converted to heat due to Stokes shift and QY losses in the present system.

Densities of the samples were calculated using a weighted average of each component based on the nominal composition. To investigate the relationship between density and thermal conductivity, thermal diffusivity and heat capacity were measured from 323 K to 723 K to calculate thermal conductivity. Thermal conductivity as a function of temperature for a 100% Ce:YAG ceramic, a 50% Ce:YAG ceramic of similar density, and 50% Ce:YAG ceramics of increasing density are shown in Figure 5.9. It can be seen that for a similar theoretical density, the thermal conductivity at 323 K of a 100% Ce:YAG ceramic doubles with the inclusion of 50 weight % α-Al_2O_3. Thermal conductivity at 323 K continues to increase with increasing density. However, the current ceramics have QY values lower than typical values reported for Ce:YAG phosphors.[19]

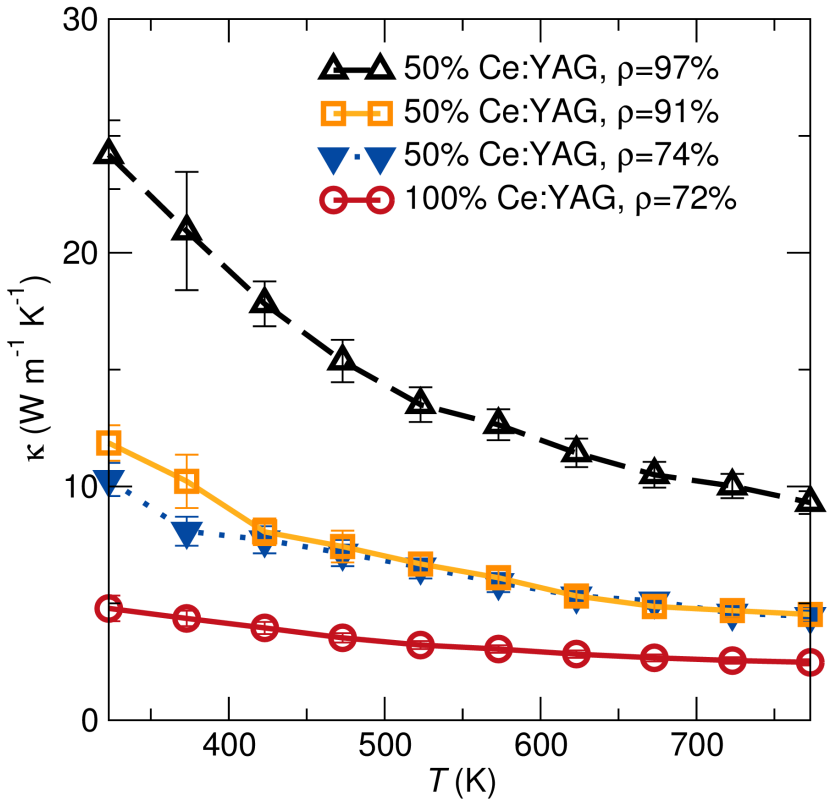

Figure 5.9: Thermal conductivity as a function of temperature from 323 K to 723 K for different ceramic samples shows that including Al_2O_3 increases thermal conductivity in the Ce:YAG/Al_2O_3 ceramics, and increasing density increases thermal conductivity. Density is listed after the sample composition. As expected, the 50% Ce:YAG ceramic with the highest density has the highest thermal conductivity. © 2018 American Chemical Society.

During conversion, more heat will be generated in the present ceramics due conversion losses due to the lower QY. The higher thermal conductivity of α-Al_2O_3 (33 W/(m·K) $\pm$2)[39] compared to 9.2 W/(m·K) for Ce:YAG[29] allows for a lower operating temperature at a given device current, which results in high conversion efficiency and higher luminous output at the same operating conditions due to reduced thermal quenching. This also allows for higher power density without reaching a thermal quenching or degradation regime.[31]

In the current work, benefits of the high thermal conductivity α-Al_2O_3 compete with the deleterious effects of porosity. It has long been known that both volume fraction of porosity and the size, shape, and orientation of the pores play a large role in the thermal conductivity of ceramics.[123] The change in thermal conductivity for a given temperature in the current work is similar to observed values for alumina with an increase of 5-10% porosity resulting in a 5-10 W/(m·K) drop in thermal conductivity,[123] which is directly related to the pore volume fraction in the composite materials. However, this is not observed to greatly impact the steady state temperature for the current configuration.

To test the thermal management of the ceramic composites during LD excitation, samples were irradiated using a commercial laser diode with λ_{ex}=450 nm at 5 W_{rad}. The maximum surface temperature as a function of time is shown in Figure 5.10. There is a great reduction in steady-state

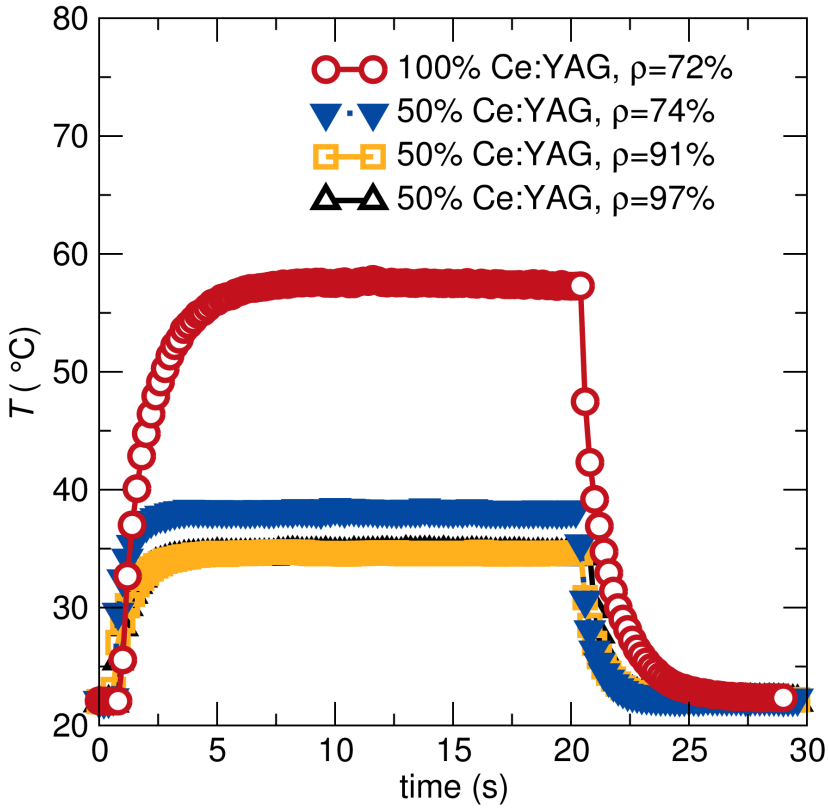

Figure 5.10: Heating curves of the ceramic samples and a Ce:YAG single crystal when excited by 5 W_{opt} of 450 nm LD excitation are shown. Including alumina in the ceramic phosphors lowers to saturation temperature to around the same value for densities ranging from 74% to 97%. All ceramic samples had the same dimensions and were affixed to a large metal heat sink using a thermal joint compound. Density of each ceramic is listed in legend. © 2018 American Chemical Society.

temperature from 57 °C to 37 °C by including alumina in the composite for a given density, which is enough to prevent thermal quenching for the Ce:YAG doping concentration investigated presently.[5, 92] There is only a difference in steady-state temperature of roughly 3 °C between ceramic composites with density of 74% and 97%, despite the large differences in thermal conductivity (Figure 5.9). While the amount of heating depends on a large number of phosphor and device-specific parameters such as the thermal conductivity, the QY of the phosphor, the size of the sample, how it is thermally fixed to a heat sink, etc., the present results demonstrate that a baseline level of thermal conductivity is achieved using α-Al_2O_3 that successfully mitigates phosphor heating. Additionally, less phosphor material results in less heating without an appreciable loss in luminous flux (1180 lm for 100% Ce:YAG and 1023 lm for 50% Ce:YAG). In the current work, all samples are the same cylindrical shape with identical dimensions of 8 mm diameter and 2 mm thickness. For LD-based white lighting, small samples are preferred as it can be used as a quasi-point source. As sample volume decreases, the differences in thermal conductivity will likely play a larger role due to less thermal mass. However, it is observed in the current work that large increases in thermal conductivity are accompanied by small changes in the steady state temperature. Therefore, Ce:YAG/Al_2O_3 composites mitigate temperature very well whilst converting laser light even if

the densities achieved are not the theoretical maximum.

One additional consideration for ceramic composites their scattering behavior, as the reflected light will play a role in both the color of a device as well as device safety. A recent study of this system hypothesized that the use of α-Al_2O_3 introduced additional scattering, resulting in altered light propagation and increased extraction efficiency, whereas transparent samples waveguide light via total internal reflection.[38] In the present work, angular dependent emission was collected for a 50% Ce:YAG ceramic sample as prepared via SPS with a rough surface and a commercially prepared Ce:YAG single crystal that is roughly the same volume using a home-built system described in Figure 6.7.

A polished surface reflects light away at the same angle as the incident light, meaning the reflected angle and incident angle are equivalent, and is known as specular reflection. A rough surface will reflect the light at more than one angle but predominantly in the same direction as the polished surface. For LD-based lighting in a reflection geometry, a matte surface might be preferred for color mixing, as blue source and yellow emitted light must mix to create white. Perfectly matte surfaces diffusely scatter light resulting in the same apparent brightness in every direction. While phosphor materials exhibit omnidirectional emission for the light that is absorbed and emitted, scattering of the incident light is an important consideration for making reflection-based devices.[124] In

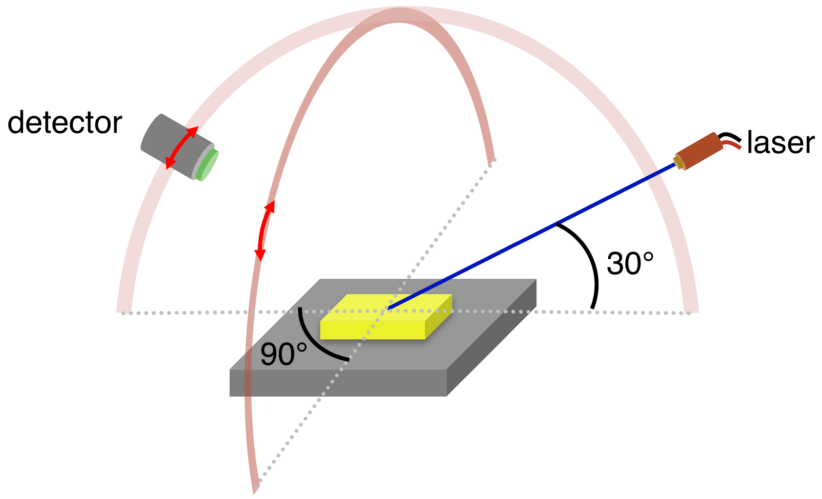

Figure 5.11: Scheme for measuring the angular dependence of light emission. The blue laser diode is fixed at an angle of 30°, relative to the sample surface while a detector attached to a goniometer arm is scanned along longitudes from 0°, to 180°, (scan directions indicated by the double arrows). First, the detector is scanned from 0° to 180° in the same plane as the laser diode, which is denoted as the 0° azimuthal scan in the data. Longitudinal scans at azimuthal angles of 45° and 90° with respect to the plane of the laser were also carried out. The longitudinal detector arc at an azimuthal angle of 90° is indicated. © 2018 American Chemical Society.

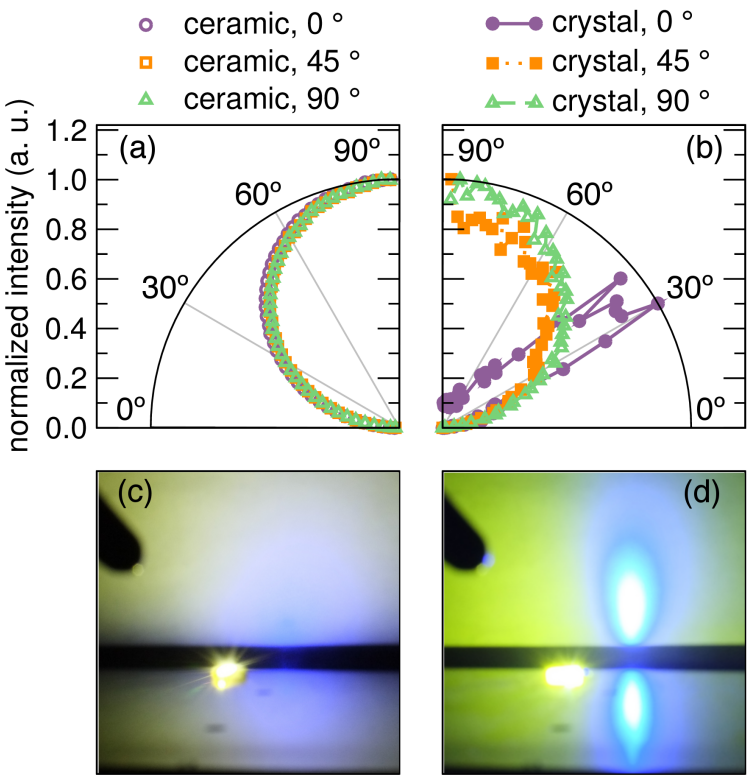

Figure 5.12: Normalized emission intensity for 375 nm to 525 nm emission is shown in (a) for a Ce:YAG/Al_2O_3 ceramic composite (open shapes) and in (b) for a roughened Ce:YAG single crystal (closed shapes connected with lines). The samples were excited by a blue LD at 30° incident to the sample surface, and the data is shown as a function of $\cos(\theta)$. Data for azimuthal detector angles of 0°, 45°, and 90° relative to the laser path are shown. The ceramic composite sufficiently scatters blue light rendering a uniform white color, as shown quantitatively by the isotropic luminance (a) and qualitatively in the photograph (c). The roughened single crystal reflects blue light at with the same angle as the incident LD (b), which leads to nonuniform emission (d). © 2018 American Chemical Society.

the present work, the reflection geometry is investigated as a demonstration that leverages the highly scattering nature of the ceramic composites.

Using a blue LD positioned at 30 ° incident to the phosphor, three collection angles of 0°, 45°, and 90° were used to characterize the nature of the reflected blue light. It was observed that after the normal routine of surface sanding to remove the graphite foil present after SPS preparation, the 50% Ce:YAG ceramics display Lambertian reflection of incoming laser light. This is shown quantitatively in polar coordinates in Figure 5.12(a), which leads to diffuse blue reflection that mixes with yellow Ce:YAG emission to create white light (Figure 5.12(c)). A Ce:YAG single crystal was subjected to the same sanding regime as the SPS ceramics in an attempt to create a matte surface, but under LD excitation, the single crystal displays spread blue reflection associated with a rough surface. This is shown quantitatively in Figure 5.12(b), where the highest peak intensity of blue light is observed at the reflected angle of 30°, leading to a spread laser spot surrounded by a halo of converted yellow light (Figure 5.12(d)). It is likely that the high hardness of the Ce:YAG single crystal prevented sufficient roughening using the techniques attempted in the present work. However, it is difficult to conclude that surface roughening alone would prevent total internal reflection in the single crystal phosphor. Therefore, effort needs to be taken to texture or pattern the surface of single crystals in the

attempt to produce Lambertian reflection of blue light, whereas SPS-prepared polycrystalline ceramics in the present work display Lambertian emission as prepared without additional processing, resulting in high outputs of thermally stable white light. Therefore, the increased thermal conductivity of ceramic composites over single crystals, as well as the Lambertian scattering achieved with no additional sample preparation render ceramic composites competitive candidates for high power LD-based lighting devices in reflection geometries.

In conclusion, the realization of encapsulation-free phosphor ceramics is required for the next generation of laser-based white lighting due to the temperature limitations of resins and glasses. With increased light output, drastically lower operating temperatures, and white color points, these composites offer an advantage over the exemplary phosphor material alone. By mixing α-Al_2O_3 and Ce:YAG powders and consolidating using SPS, the steady state operating temperature of the ceramic under laser flux is observed to reduce greatly. This is likely due to the presence of less phosphor material, as well as the thermal conductivity of α-Al_2O_3 being larger than Ce:YAG single crystals by a factor of $\approx$3. One key advantage to using α-Al_2O_3 over other filler/composite oxides is that there are no phases between $Y_3Al_5O_{12}$ and Al_2O_3 on the Y_2O_3/Al_2O_3 phase diagram, which results in no reactivity between the two oxides during preparation of the ceramic composites. Thus, using α-Al_2O_3

prevents the formation of secondary phases, ensuring the purity of Ce:YAG in the ceramic composites produced. Improvements in efficiency will come from improvements in processing, as well as the use of higher quality starting materials with higher initial QY values. One important benefit of the SPS technique is that many oxide materials, both oxide phosphors and high thermal conductivity scattering oxide fillers, can be combined and sintered together. These scattering ceramics are viable candidates for LD-based white lighting due to the improved thermally stability, which is seen to reduce the operating temperature of the phosphors regardless of sample density in the configurations tested thereby preventing thermal quenching of the phosphor. Additionally, light is scattered and results in a more uniform distribution of blue and yellow light. For use in devices, the relationships between heat mitigation, color uniformity, and luminous flux must be considered as a function of the specific device geometry, including sample size and heat sink size, as small samples can be combined with LDs to achieve quasi-point source-like behavior.

Chapter 6

Conclusion

6.1 Summary

Through the work presented in this dissertation, we have elucidated the role of intrinsic and extrinsic properties of phosphors to better prepare and engineer these materials. First, we have shown that Al and O have a surprising affinity for one-another in the β-SiAlON structure, despite the high dilution of both Al and O in the framework. High-field ^{27}Al solid-state NMR spectral features were assigned to different AlO_qN_{4-q} ($0 \leq q \leq 4$) species, employing DFT calculations to help in the assignment. These results suggest unambiguously that $AlON_3$ with $q = 1$ and AlO_2N_2 with $q = 2$ are found in far greater excess than would be

suggested by a stochastic distribution of Al and O on the β-Si_3N_4 framework. DFT calculations of defect energetics on large supercells also suggest extra stabilization associated with Al–O clustering in the unit cell, which can be anticipated by electrostatic bond valence arguments. This work also shows the exquisite details of local compositional fluctuations in crystal structure that can be unravelled by the judicious combination of high-field, high-resolution NMR experiments coupled with DFT calculations.

Next, the local structure trends of the activator site of these materials when doped with europium were shown to dictate macroscopic properties of this commercially relevant phosphor. It has been shown that specific emission properties can be targeted via compositional tuning, such as narrower emission β-SiAlON:Eu^{2+} (low z) for lower temperature operation, or maximum PLQY and improved thermal stability (higher z up to 0.125) for high flux and/or high temperature operation. We have provided experimental evidence on the role of increasing z at low concentrations in β-$Si_{6-z}Al_zO_zN_{8-z}$:Eu^{2+} in modifying the structure and the resulting optical properties. XANES was used to confirm that the majority of Eu in the structure is in the active Eu^{2+} state, which allows for further investigation of the role of varying z as any observed changes in optical properties are not due to differences in Eu valence between samples. Increasing z distorts the Eu-N/O_9 environment, resulting in a red shift and

broadening of emission. Temperature-dependent emission for these samples are robust with an increase in thermal stability with increasing z, due to the large gap between 5d levels and the conduction band of the host. Increased thermal quenching resistance is observed with increasing z over a small range, and likely gives rise to the increased quantum yield due to the predicted high barrier for thermal ionization that increases with increasing z. The present work provides experimental verification of optical properties resulting from an increase in the polyhedral distortion of the Eu^{2+} activator site with increasing Al/O content, as well as enhanced thermal stability due to a large thermal ionization barrier. Our work illustrates that structurally tuning the host lattice at low concentrations can be leveraged to optimize the optical and thermal performance of this important inorganic phosphor.

Following this, it is now important to develop an understanding of how these materials can been used to support the advent of high power solid state lighting. To this end, blue emitting phosphor powders were prepared using microwave-assisted heating in 25 min, which reduces preparation time and energy consumption. Results of the refinement on synchrotron X-ray diffraction data demonstrate the viability of microwave assisted heating for preparation of phase pure $BaMgAl_{10}O_{17}:Eu^{2+}$. Phosphor powders were then densified into opaque or translucent dense ceramics using SPS in 30 min, with a heating rate of

200 °C to a temperature of 1500 °C for a 5 min hold. QY of the starting powder does not change from after densification into a translucent sample, and could likely be improved using optimized starting powders. Due to the monolithic nature of the present blue-emitting phosphor, translucent phosphors prepared in this way are useful as a blue component in warm white light generation using LDs for general illumination and visible light communication. This phosphor can be used in conjunction with others to make white light. Therefore, a single phosphor solution was sought to demonstrate the effectiveness of this preparation technique for high power white lighting.

Lastly, the realization of encapsulation-free phosphor ceramics is required for the next generation of laser-based white lighting due to the temperature limitations of resins and glasses. With increased light output, drastically lower operating temperatures largely independent of sample density, and white color points, the phosphor composites explored in the present thesis offer an advantage over the exemplary phosphor material alone. By mixing α-Al_2O_3 and Ce:YAG powders and consolidating using SPS, the steady state operating temperature of the ceramic under laser flux is observed to reduce greatly. This is likely due to the presence of less phosphor material, as well as the thermal conductivity of α-Al_2O_3 being larger than Ce:YAG single crystals by a factor of $\approx$3. Improvements in efficiency will come from improvements in processing,

as well as the use of higher quality starting materials with higher initial QY values. For use in devices, the relationships between heat mitigation, color uniformity, and luminous flux must be considered as a function of the specific device geometry, including sample size and heat sink size, as small samples can be combined with LDs to achieve quasi-point source-like behavior. Recent modeling efforts have shown that small spot sizes can lead to extreme local heating depending on the phosphor geometry, the thermal resistance of the device, and the power delivered as a function of spot size,[125] so future device work must be studied and understood on a system level.

In the appendix of this work, experiments show the discrepancy between temperature dependent emission and lifetime measurements for phosphors of different morphologies. The quenching temperature of Ce:YAG is observed to be a result of low doping regardless of whether it is in single crystal or powder in silicone form. In the future of high power LED and LD-based lighting sources, it will be important to explore the role of quenching temperature. The present results remind us that that thermal conductivity does not dictate the inherent quenching temperature, as the phosphor in silicone and single crystal differ in thermal conductivity by two orders of magnitude, but display nearly identical behavior. However, thermal conductivity of the phosphor during operation should be investigated further, as it is expected that a single crystal

will withstand higher laser fluxes because it will not melt like silicone. With Ce:YAG single crystals being explored for transmission LD-based white lighting, the potential complex interplay between the ability to dissipate heat and the thermally quenching temperature must be explored further.

6.2 Future Directions

As stated in the present thesis, there is a need in the lighting industry for small and high-power solid-state lighting devices. Widely used LEDs suffer from droop of efficiency at high current densities. Multiple chips or larger solid state area can compensate this effect but also increase both package size and cost. Laser lighting can consist of one small single chip operating at high current densities, allowing decreases in size and increases in luminous flux output. Moreover, smaller dimensions of the lighting device can be advantageously used to reduce the angular divergence of emitted light.[126, 127] To this end, it is possible to engineer a laser-based system with an angular divergence less than five degrees, which is still a challenge in LED systems. To ensure the promise of these devices, warm white emitters must be developed through including some red or amber emission in a device due to market demands and

[1]The contents of this section were made possible thanks to contributions from Nicholas O'Dea, Guillaume Lheureaux, and Caroline Reilly

increasing understanding of the role blue light may play in regulating circadian rhythm.[128] This can be achieved through advances in laser efficiencies and phosphor development of stable red phosphors for warm laser lighting, which have been demonstrated.[129] The challenges and preliminary work conducted at UCSB will be discussed.

6.2.1 Calculating lumens per watt and color coordinates

Solid state lasers emit photons nearly monochromatic light, and these photons can be converted by phosphors into a broader range of colors. Specifically for a transmission geometry, where a laser is incident on a phosphor and light is collected on the side opposite, some laser light is not absorbed by the phosphor and is either reflected or transmitted without conversion to a different wavelength. The total power of the light as it passes from the laser to the phosphor to final emission is impacted by several loss mechanisms. First, some of the laser light is absorbed and not re-emitted. In this case, the amount of energy that is absorbed is multiplied by the efficiency of the phosphor (quantum yield, or QY) to account for the amount of light lost to purely non-radiative processes. Second, the power of light emitted by the phosphor is shifted from that of the laser. The difference between the absorption and emission energy is

known as the Stokes Shift or SS, which is is the power-averaged wavelength of the phosphor and the laser. This ratio provides the average amount of energy of a phosphor photon over the average energy of the laser-emitted photon. The power of the converted light is therefore shifted from that of the absorbed light by both the quantum yield and the Stokes Shift. Since the phosphor is a uniform emitter, a first-order optical component can used to increase the amount of directionally-focused light. In this case, the absorption of light by this optic and the heat sink incorporated into it may be non-negligible. Let η_{des} be the optical efficiency of the overall design, including the optic and the heat sink. With an efficiency less than 1, the power of the light decreases to P_f. Then the final power of the device is

$$P_f = \eta_{des} \cdot (P_{uncon} + P_{abs} \cdot QY \cdot SS) \tag{6.1}$$

The number of lumens per watt is wavelength dependent. Since the relative shape of phosphor emission spectra remains constant, a phosphor has a fixed luminous efficacy that can be found by considering its emission spectrum multiplied at each wavelength by the eye response function. Let Φ_{las} and Φ_{phos} be the luminous efficacies of the laser and phosphor. For the laser and the phosphor, the luminous efficacies used here refer to the the number of lumens

per optical watt of power. However, for the final lumens per watt of the system, both the lumens per watt of optical power and the lumens per watt of electrical power can be important, and both will be explored.

$$L = \eta_{des} \cdot (P_{uncon} \cdot \Phi_{las} + P_{abs} \cdot QY \cdot SS \cdot \Phi_{phos}) \tag{6.2}$$

P_{uncon} and P_{abs} are both related to the power of the laser. Let R_{abs} be the ratio of absorbed photons to the number of laser pump photons. Then $P_{uncon} = P_{las} \cdot (1 - R_{abs})$ and $P_{abs} = P_{las} \cdot R_{abs}$. This gives

$$L = P_{las} \cdot \eta_{des} \cdot ((1 - R_{abs} \cdot \Phi_{las} + R_{abs} \cdot QY \cdot SS \cdot \Phi_{phos}) \tag{6.3}$$

Dividing by the power of the laser, one has the system's lumens per watt of optical power,

$$\Phi_{Sopt} = \eta_{des} \cdot ((1 - R_{abs} \cdot \Phi_{las} + R_{abs} \cdot QY \cdot SS \cdot \Phi_{phos}) \tag{6.4}$$

Multiplying by the wall plug efficiency of the laser, η_{las}, gives the system lumens per watt of electrical power,

$$\Phi_{Selec} = \eta_{las} \cdot \eta_{des} \cdot ((1 - R_{abs} \cdot \Phi_{las} + R_{abs} \cdot QY \cdot SS \cdot \Phi_{phos}) \tag{6.5}$$

Table 6.1: Lumens per watt of pumps and phosphors sorted by CIE function date shows that the newer functions give the greatest lm/W for all three laser pumps and Ce:YAG. However, the newest functions are tentative, and the more accepted 1988 function introduced some corrections to the brightness of blue and violet light in the 1931 function.

	1931	1988	2011
Ce:YAG	488.07	488.07	501.16
415 nm laser	1.49	8.05	9.77
442 nm laser	15.96	24.77	36.42
470 nm laser	67.65	67.65	88.72

Also, since varying the amount of laser light that is absorbed by the phosphor will change the color and lumen output of the device, there exists an optimum ratio of converted to unconverted light.

The Stokes Shift of Ce:YAG is the laser wavelength divided by the phosphor centroid wavelength. The centroid wavelength for Ce:YAG is about 573 nm. For simplicity, all laser photons are treated as though they are at the laser peak wavelength. Table 6.1 provides the calculated luminous efficacy for the canonical phosphor Ce:YAG, as well as for a few different laser pumps. These are Φ_{las} and Φ_{phos} discussed above. The Ce:YAG efficacy was calculated using

the shape of the spectrum of a Ce:YAG single crystal collected experimentally. The different years refer to the different CIE functions used to find the luminous efficacy.

The (x, y) coordinates for the 1931 CIE standards of color can be calculated through the following series of steps. Using the $\bar{x}$, $\bar{y}$, $\bar{z}$ functions to find the relative weighting of color at each wavelength of a spectrum, and X, which is the sum of the power of light at each wavelength multiplied by $\bar{x}$ at that wavelength, then the (x, y) coordinates are found using the following expressions:

$$x = \frac{X}{X + Y + Z} \tag{6.6}$$

and

$$y = \frac{Y}{X + Y + Z} \tag{6.7}$$

Y and Z are found analogously.

If the power of a light source is scaled, its color point will change similarly, as x and y effectively divide out the power. However, if the relative powers of different colors within a spectra change, then its (x, y) color point will change. Then the calculated color point of the laser-phosphor light mixture must capture

the exact proportions of the final light mixture.

Here, we will scale the power of the final laser light to be in the proper proportion to the phosphor light. Note that

$$P_{uncon} = P_{las} \cdot (1 - R_{abs}) \tag{6.8}$$

while

$$P_{phos} = P_{las} \cdot SS \cdot QY \cdot R_{abs} \tag{6.9}$$

Then the ratio of unconverted laser light to phosphor light is

$$\frac{P_{uncon}}{P_{phos}} = \frac{1 - R_{abs}}{R_{abs} \cdot SS \cdot QY} \tag{6.10}$$

This ratio gives the relative powers of the unconverted laser light and the phosphor converted light, and then allows one to predict the color points for different values of R_{abs}.

From this framework, it is clear how drawing a line on the CIE diagram between two points represents attainable colors from mixing of the two, with the slope of the line is determined by the color point of the laser and the color point of the phosphor. Systematic changes in R_{abs} can be understood as follows,

beginning with all laser and no phosphor coupling, which resides in the lower left of a CIE 1931 diagram, and ending with all light converted and no laser light in the right of a CIE 1931 diagram.

An expression for number of lumens per watt can be written as follows:

$$\Phi_{Selec} = \eta_{las} \cdot \eta_{des} \cdot (QY \cdot SS \cdot \Phi_{phos} - \Phi_{las}) R_{abs} + \eta_{las} \cdot \eta_{des} \cdot \Phi_{las} \tag{6.11}$$

This form, similar to $y = mx + b$, helps emphasize the contribution of R_{abs}. If $QY \cdot SS \cdot \Phi_{phos} > \Phi_{las}$, as it is in every case explored here since $\Phi_{phos} >> \Phi_{las}$, then the system lumens per watt is monotonically increasing in R_{abs}. Then increasing R_{abs} while holding the other parameters fixed will increase the number of lumens. One guideline for LED efficiency as dictated by the US Department of Energy is that LED devices are to reach 200 lm/W. In our current exploration using a laser pump instead of an LED pump, there is thus a minimum value for R_{abs} in order to reach this 200 lm/W value. If the other parameters are specified, we can solve for R_{abs} using the previous expression as follows:

$$R_{abs} = \frac{\Phi_{Selec} - \eta_{las} \cdot \eta_{des} \cdot \Phi_{las}}{\eta_{las} \cdot \eta_{des} (QY \cdot SS \cdot \Phi_{phos} - \Phi_{las})} \tag{6.12}$$

If laser efficiency values are to reach LED values (η_{las} = 0.70), and assuming

our Ce:YAG phosphor is optimized to QY = 0.95, and with an assumed optical efficiency for the phosphor as 96%, and the device total optical efficiency (η_{des}) to be between 0.9 and 1, we can calculate R_{min} values for different laser pumps. The choice of luminous efficacy function has little effect on the ratio of light needed to produce 200 lm/W. Based on what is known for the maximum luminous efficacy for a pair of monochromatic emitters, the best possible scenario for luminous efficacy is 420 lm/W for 6500 K and >500 lm/W for lower CCTs.[6] Additionally, being above the Planckian locus in a CIE 1931 diagram means higher lm/W values. Therefore, in our calculations, we assume an acceptable deviation of 0.01 above the Planckian locus. It follows that using a 445 nm laser (70% WPE) and a Ce:YAG single crystal (95% QY), we calculate the maximum luminous efficacy of white light to be 191 lm/W on the locus (CT=6920 K) and 203 lm/W (CCT=5800 K) for 0.01 above the locus, which is a 10% increase. In these calculations, 200 lm/W is the maximum possible value. Is it therefore reasonable to say that laser lighting is likely to outperform LEDs in luminance, or lumens delivered to a source, rather than outperform LEDs in terms of electrical efficiency, at least for now.

6.2.2 Theoretical investigation of a cool white laser-based emitter

One way to develop a viable light source is to enable new or increased functionality. In the case of laser lighting, use of a phosphor with a blue laser diode allows for a large reduction in the size of the emitting area. Previous experimental demonstrations of the luminous flux emitted from laser excited phosphors show that it already exceeds those of LED devices for a single solid-state emitter. Challenges for laser-based lighting include thermal management of the phosphor and the laser. Currently, the wall plug efficiencies (WPEs) of commercial blue laser diodes range from 30% to 38%, which will limit the luminous efficiency in lab demonstrations. In the current work, experimental measurements of laser excited Ce:YAG single crystals were modeled successfully using Lighttools, where parameters were measured experimentally instead of as fitting parameters in the simulation (Figure 6.1). The parameters and how they are measured are detailed as follows. The excitation spectrum represents the probability of a photon to be absorbed and emitted into visible light as a function of the wavelength (emission spectrum), and both excitation and emission are obtained experimentally using a fluorimeter. The QY is the ratio between the emitted photons and

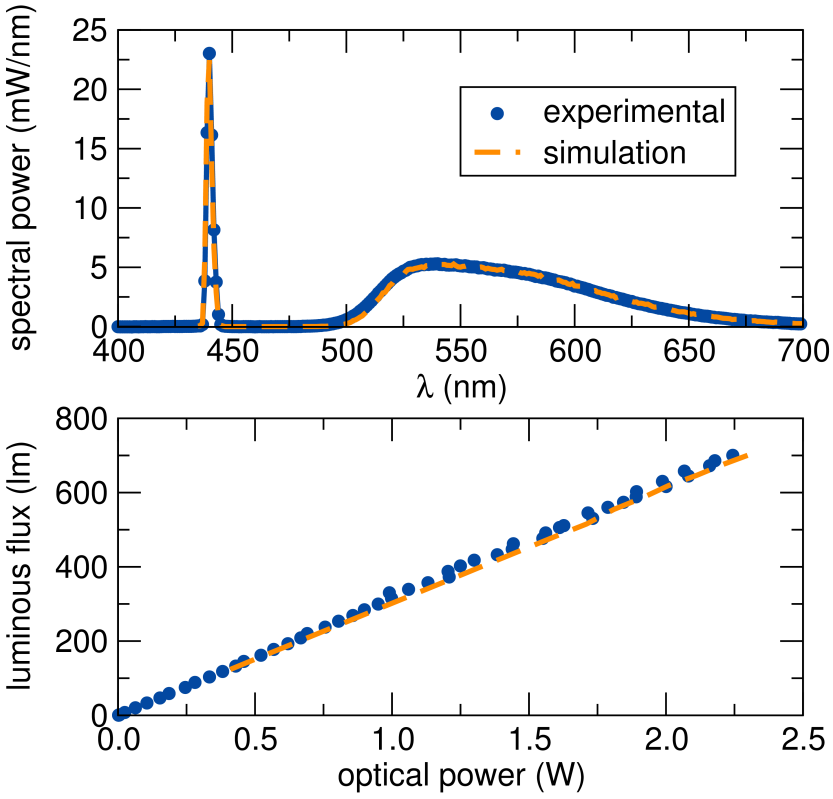

Figure 6.1: Results of Monte Carlo ray tracing simulations match extremely well with experimentally observed spectral power density (top) and luminous flux as a function of input laser optical power (bottom). By using experimentally obtained values to describe the optical properties of the phosphor, the physics of the system is properly modeled, paving the way for accurate simulations of device prototypes.

absorbed photons, which is measured using an integrating sphere setup with a laser as the excitation source. The absorption spectrum is collected using an integrating sphere attachment to accommodate scattering samples in a UV-Visible Spectrometer. The mean free path is defined as the average distance a photon can travel inside the material before being scattered or absorbed. In the case of a single crystals with polished and parallel sides, the mean free path is easily extracted from the sample transmission measurement according to the Beer-Lambert Law, and thickness is measured using calipers.

One simple design of a device involves placing the phosphor at the focal point of a parabolic mirror to achieve very low angular divergence. A schematic view of the device design is visible in Figure 6.2. Using Lighttools, Figure 6.3 shows the resulting angular divergence as a function of the reflector diameter. For this calculation, the phosphor size is held constant, with a radius and a thickness of 0.25 mm. It can be seen that very low angular divergences can be achieved for reflector diameters greater than 10 mm, due to the smaller size of phosphor compared to the emitting area needed for LEDs. By keeping the phosphor approximately the same size as the laser spot size, a quasi-point source can be achieved. This is important because phosphors emission behavior is omnidirectional, and the benefits étendue conservation from the very narrow incident beam are mitigated if the phosphor is much larger than the beam. The

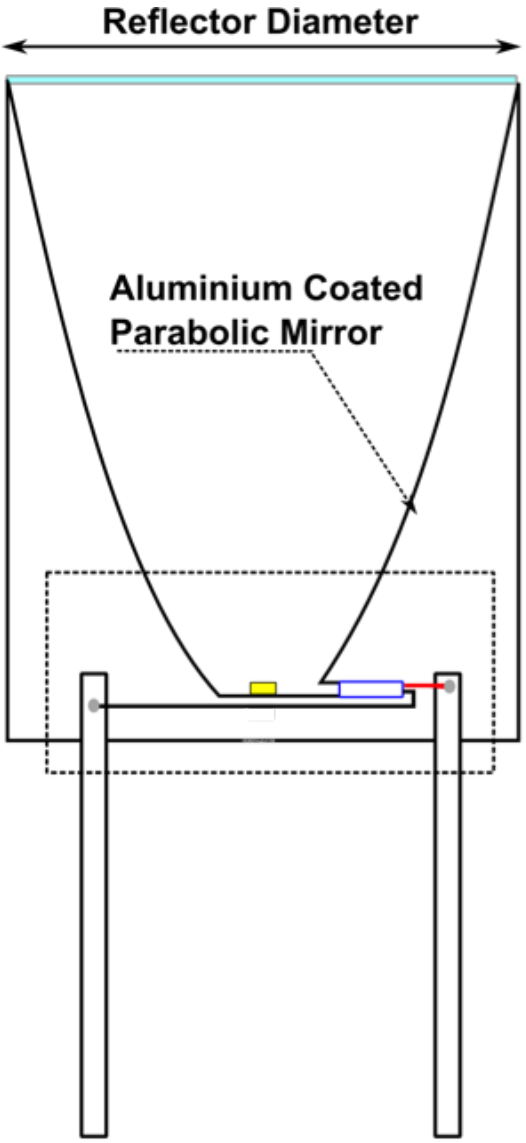

Figure 6.2: Schematic representation of a typical reflective design for a laser-based white lighting device. Radius and thickness of the phosphor disk have been fixed at 0.25 mm.

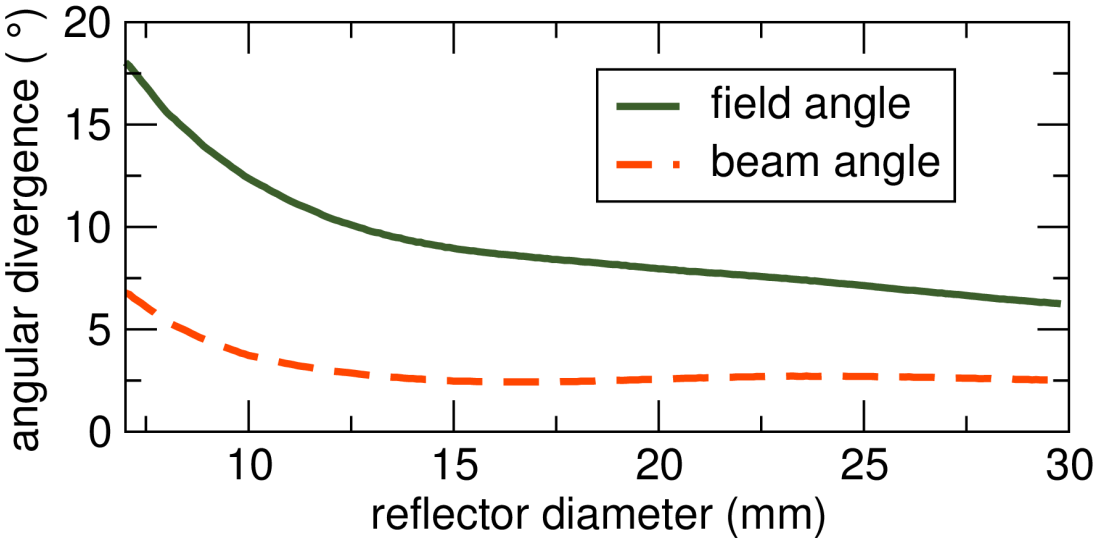

Figure 6.3: Angular divergence of the emitted light as a function of the reflector diameter. Radius and thickness of the phosphor disk have been fixed at 0.25 mm.

Table 6.2: State of the art commercial white LED compared to results obtained by numerical simulation carried for a single-crystal phosphor disk excited by a blue laser diode show the increased light output possible with a smaller solid-state device. Laser device simulated operating at 5 W, and values in the table are calculated. The geometry of a conceptual device used in the simulation is visible in Figure 6.2. The LD-based reflector dimensions are as follows: phosphor dimensions radius= 1 mm, thickness = 0.25 mm, and reflector = 10×11 mm. The absorption coefficient of the phosphor was fixed in the simulation to be 12 cm^{-1}, which was obtained experimentally by measuring the absorption using a UV-visible spectrometer.

Device	Dimensions (mm^3)	Luminous flux (lm)	Luminous efficiency (lm/W)	Angular divergence (°)
Luxeon 5050 (Lumileds)	5×5×0.7	610	156	116
NWSW229A (Nichia)	4×4×2.3	637	150	135
XLamp XT-E LEDs (Cree)	4×4×2.3	629	178	115
LD-based reflector	in caption	1000	100-150	4

present simulations show a luminous flux output of more than 650 lumens when 3 W are delivered by a blue laser, a luminous flux which is comparable to state of the art high-power single-chip white LEDs shown in Table 6.2. It should be noted that the input laser power can be increased to reach higher lumen output. In addition to the distribution of light generated from these reflectors, geometry, surface finish, and manufacturing costs must be considered.[130]

Another possible alternative reflector design is showed in Figure 6.4. A cylindrical phosphor is placed at the bottom of the parabolic reflector and operated in transmission. The placement of the phosphor improves the surface contact between the phosphor and the reflector to improve thermal management. Assuming a polished single crystal Ce:YAG sample, the color over angle of the resulting spotlight is poor (Figure 6.5) and variation can be easily overcome using surface roughening. For a transmission geometry, a rough surface on the incident side of the phosphor improves the laser light coupling and provides better color uniformity at the emission side of the phosphor, as illustrated in (Figure 6.4(b)), which shows the angular distribution of the phosphor and laser emission in true color as obtained in simulations. To control color in such a device, the thickness of the phosphor cylinder is the optical path of and can be adjusted to tune the color of the spotlight as illustrated in Figure 6.4(c), which shows the color point of the emitted light for different

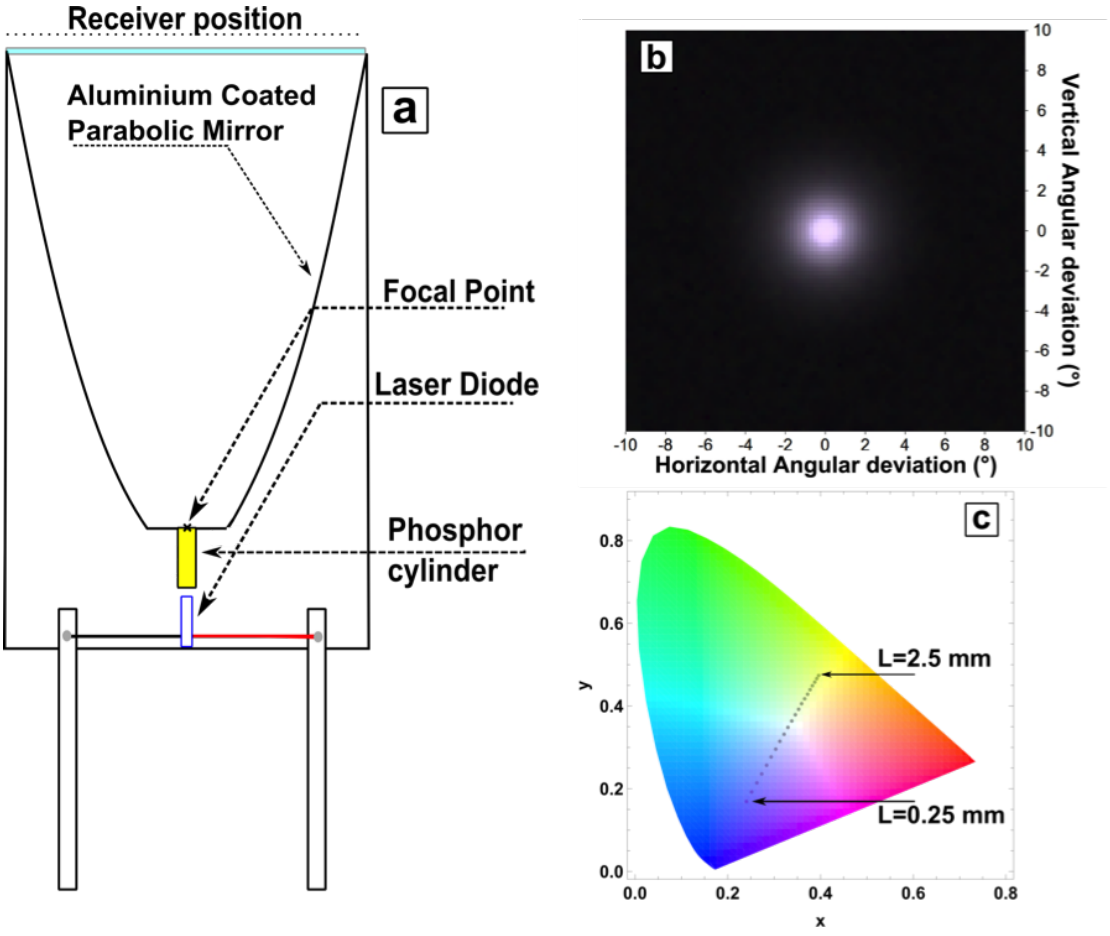

Figure 6.4: Schematic representation of a transmission design for a laser-based white lighting device is shown in (a). The phosphor cylinder has a fixed radius of 0.25 mm and is placed at the bottom of the reflector. The simulated angular distribution of the light at the reflector output for a roughened phosphor is shown in true color (b), demonstrating the excellent color uniformity and absence of color over angle variation that is seen for polished surfaces. The color point is tunable by altering the phosphor thickness, as shown in the 1931 CIE diagram. A thickness of 1.5 mm emits a color very close to the white point.

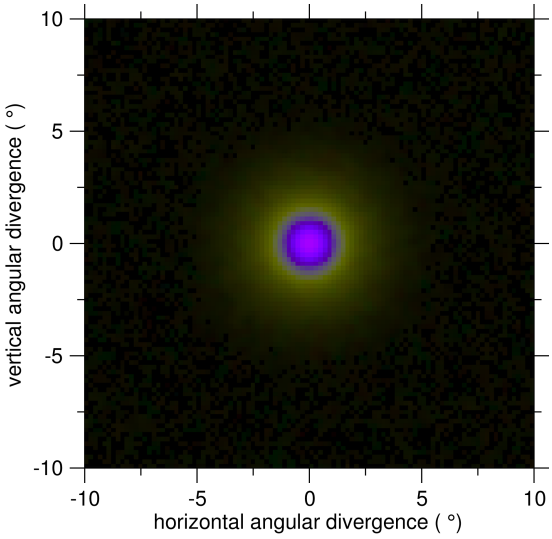

Figure 6.5: The simulated angular distribution of the light at the reflector output for a phosphor single crystal with smooth, polished surfaces shows very poor color uniformity. The phosphor cylinder has a fixed radius of 0.25 mm and is placed at the bottom of the reflector.

phosphor cylinder thicknesses. Phosphor length could also be increased to reach higher lumens output, depending on the desired application. The two reflector designs presented currently could also utilize multiple lasers, leading to a compact and powerful light source with higher luminous flux than a single diode source.

6.2.3 Theoretical investigation of a warm white laser-based emitter

Calculations on two phosphor systems were performed to investigate the fundamental limits for generating white light with a 445 nm laser using different red phosphors. No reabsorption or interactions of the phosphors were considered; these calculations are simply a result of the color based on the emission spectra, the amount of red phosphor absorbed, which is a tunable parameter, the amount of Ce:YAG absorbed needed, a calculated parameter, and the phosphor quantum yields (QY). The QY assumed were 95% for Ce:YAG. The three red phosphors investigated were the canonical broad-emitting nitride $CaAlSiN_3$:Eu^{2+}, which has some emission in the IR and modest QY=70% as measured experimentally by these authors, the narrow band $Sr[LiAl_3N_4]$:Eu^{2+} (SLA) which has reduced emission in the IR and a low reported QY=52%,[131]

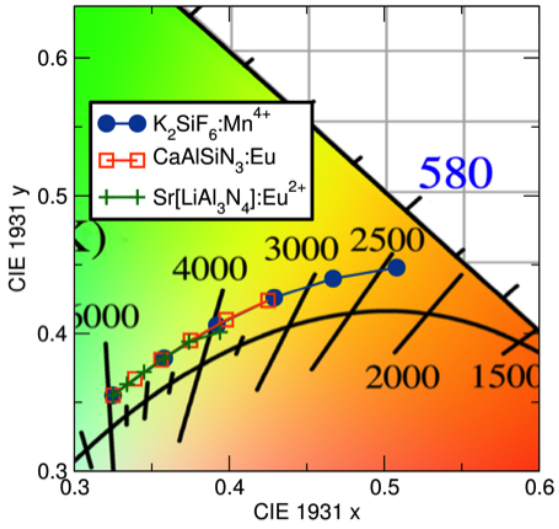

Figure 6.6: Section of a CIE 1931 diagram showing the results of calculations of Ce:YAG single crystal emission (QY=95%) used in conjunction with $K_2SiF_6:Mn^{4+}$ (QY=70%, closed blue circle), $CaAlSiN_3$:Eu (QY=70%, open red square), and $Sr[LiAl_3N_4]:Eu^{2+}$ (QY=52%, green plus). $K_2SiF_6:Mn^{4+}$ showed the widest range of color temperature tunability with also the highest luminous efficacies. For the calculations, the amount of red absorption was fixed, the amount of Ce:YAG absorption was refined, and a maximum of 0.01 above the locus was allowed.

and K_2SiF_6:Mn^{4+} (KSF) which is used for display applications and has a measured QY=76% at 410 nm excitation and was assumed 70% for calculations. KSF may not be suitable for high flux due to the saturation of excited states in Mn^{4+}, but was explored in the present work as it is gaining popularity for its desirable color quality. The results in Figure 6.6 show that KSF demonstrates the lowest CCT (2395 K), and the highest efficacy (232 lm/W) for 50% red absorption and 49% Ce:YAG absorption was calculated. Assuming 10% of red absorption, 75% Ce:YAG absorption was calculated with a CCT of 4690 K and an efficacy of 284 lm/W calculated. These two efficacy values greatly outperformed white light obtained using Ce:YAG and $CaAlSiN_3$:Eu or SLA, but need to be experimentally realized and verified. Additionally, neglecting absorption and interaction of the two phosphors for 10% red absorption and 75% Ce:YAG single crystal absorption with QY=95%, a luminous efficiency of 200 lm/W might be the upper limit if LD WPE values reach current LED values, that is to say 70%. Moving forward, experimental verification is needed, as well as considering absorption of phosphors in the calculations. In the present work, two phosphor demonstrations using Ce:YAG single crystals and $CaAlSiN_3$:Eu red phosphors are pursued as both materials have well-characterized emission behavior and known thermal stability trends.

6.2.4 Experimental demonstration of a warm white laser-based emitter

Work on integrating the laser with two phosphors is in progress, and more optimization of the Ce:YAG sample dimensions is required to demonstrate an acceptable color point. The optical path of the single crystal needs to be decreased to continue shifting the color point of the two-phosphor system closer to the Planckian locus. The TiO_2 paint referenced in Figure 6.7, as well as the initial attempts to supply a coating of red phosphors to the surface of the single crystal, were applied using an airbrush. Red emitting $CaAlSiN_3:Eu^{2+}$ phosphor powder was mixed with thinner and applied to a glass slide. When excited by a blue laser, conversion and red emission is observed (Figure 6.9). However, when this coating is supplied to a single crystal, only the Ce:YAG emission is seen and there is no observed emission from the red phosphor (Figure 6.8. Our simulations predict that the thickness of the phosphor needs to be decreased to reduce the optical path and find the right sample dimensions to make warm white lighting using two phosphors. Utilizing a layer of red-emitting phosphor has been demonstrated for high power LEDs.[132, 133] For LD lighting, it is hypothesized that with proper heat sinking of the phosphor system, the thin layer of red-emitting phosphors will be heat sunk by the single crystal it is

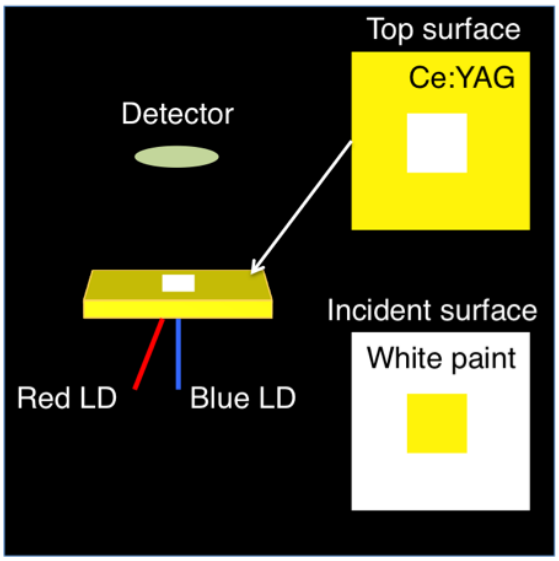

Figure 6.7: Schematic depiction of a two-laser setup, wherein a single crystal of Ce:YAG of thickness 0.47 mm is coated on the incident surface with white TiO_2-based paint, leaving a space for incoming laser light to pass. The top surface, opposite this space, is painted white to reflect any unconverted blue laser light back into the crystal, thereby increasing the optical path, allowing for more absorption, and subsequently enabling the reduced use of phosphor material to produce the same color.

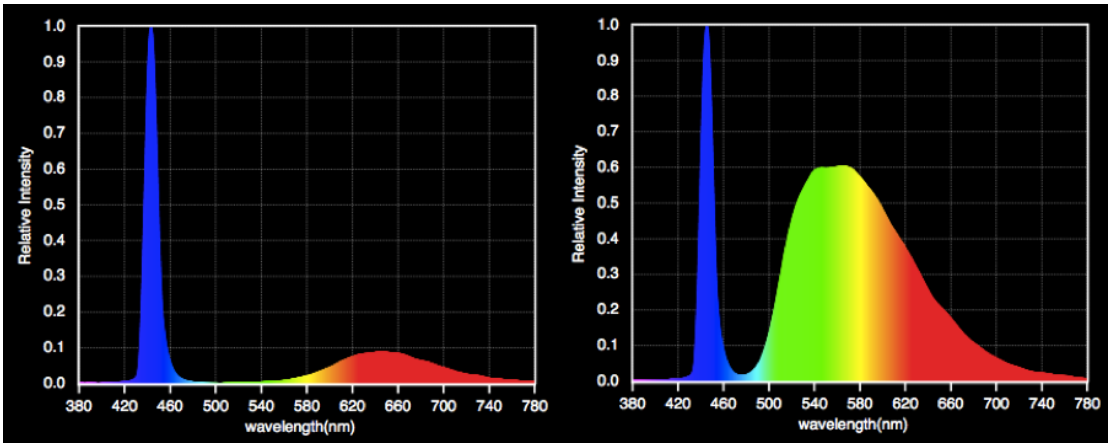

Figure 6.8: Emission spectra of a blue laser exciting a layer of red phosphor that has been painted on a glass slide (left) shows some conversion and emission in the red. When the same coating is applied to a Ce:YAG single crystal (right), the emission is dominated by the single crystal and no red emission is seen. To overcome this, the optical path of the single crystal must be reduced.

Table 6.3: Data for a two laser system shows that a CCT of 3000 K with a CRI of 80 is possible using a Ce:YAG phosphor converted by a blue laser with a supplemental red laser to shift the color. Laser optical powers given.

Red optical P (W)	Blue optical P (W)	CCT (K)	CRI	Lux
0.015	0.085	2962	80	1784
0.15	0.263	2990	80	4177
0.29	0.486	2992	79	6726

contacting.

For the time being, a two-laser approach has been investigated and does meet the requirements of warm white light, namely 3000 K and 80 CRI (Figure 6.9). In the future, a system-level comparison of laser power used for a two-laser system compared to the energy associated with absorbing and converting blue laser light with a red phosphor must be explored to determine the efficacy of both approaches, as well as comparisons for thermally stability during operation of the red laser and the red phosphor based on the selected geometries.

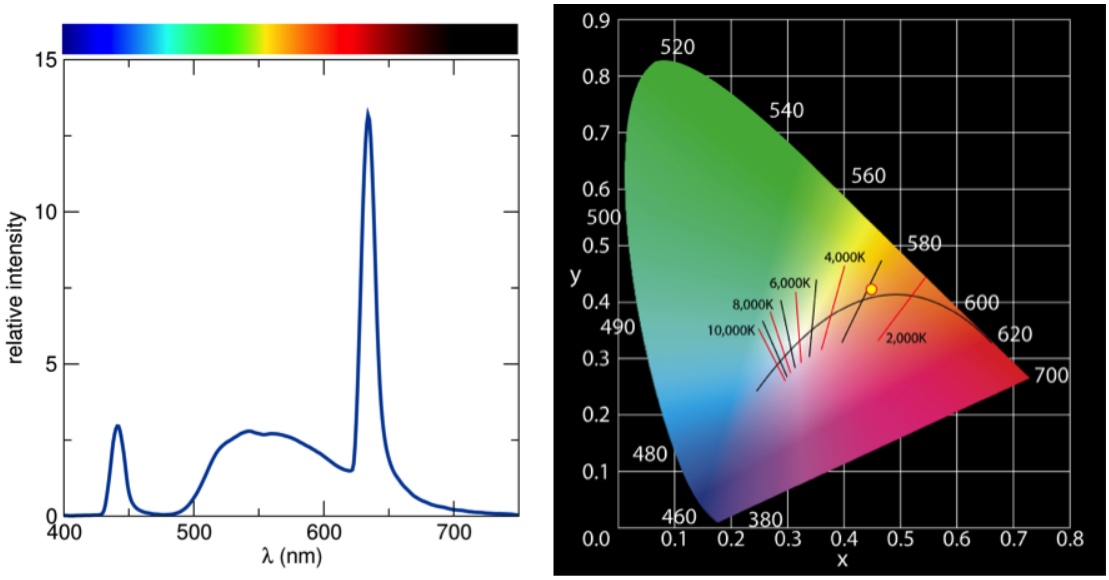

Figure 6.9: Emission spectrum of the two-laser system with CIE coordinates for the three measurements reported in Table 6.3 show a CCT of 3000 K, within an acceptable distance from the Planckian locus.

Appendix A

Thermal quenching of Ce-doped YAG: comparing single crystals and powders of the same composition

With LEDs and laser diodes being explored for high power lighting, thermal stability of inorganic phosphors used for color converting is essential. To this end, polycrystalline dense ceramics and single crystals are being studied as replacements for ceramic powders in silicone. The canonical yellow phosphor, Ce-doped yttrium aluminum garnet (Ce:YAG), has high thermal stability due

[1]The contents of this section were made possible thanks to contributions from Alex A. Mikhailovsky

to a high quenching temperature (>700 K) for low (<1% Ce) doping. In the present work, temperature dependent emission and photoluminescent lifetime measurements show nearly identical lifetime behavior from 77 K to 503 K for a single crystal and a powder derived from grinding the single crystal, indicating that the thermal quenching temperature is due to composition and not form.

A.1 Introduction

LED lighting is rapidly replacing incandescent and fluorescent sources,[10] and advances in semi polar and non polar substrates for LEDs have pushed current densities to beyond 1000 A/cm^2.[11] Ultimately, LEDs experience efficiency droop with increasing current due largely in part to Auger recombination.[134–137] Laser diodes (LDs) have peak efficiencies at much higher operating currents than LEDs and therefore offer an alternative to the droop-limited LEDs.[12] Currently, both LEDs and LDs are being explored to generate white light using inorganic phosphors, with LDs holding the most promise for the future of high power white lighting that LEDs cannot achieve due to droop.[9, 21, 22] Two common strategies are utilized for white light generation. Either a blue LED or LD is used in conjunction with a yellow-converting inorganic phosphor to generate a cool white light, or a

near-UV or violet LED or LD is used to excite a mixture of blue-, red-, and green-emitting inorganic phosphors to generate a warm white light.[2, 18] The high intensity light generated from LDs require thermally stable phosphors that are packaged to withstand the high flux.

In white LEDs, it is thought that high thermal conductivity of the phosphor is desirable, as it suggests a higher ability to dissipate heat. In recent years, many different strategies have been explored to replace the resin historically used to encapsulate phosphors, as the resin typically has a low thermally conductivity (0.18 W/(m·K)) and can turn from transparent to yellow or brown around operating temperatures.[24–26] Phosphor-in-glass, a strategy involving the mixture of phosphor powders with glass frit at low temperatures ($<$1000 °C), shows an order of magnitude increase in thermally conductivity (2.18 W/(m·K)), which is higher than the soda lime glass itself (0.97 W/(m·K)).[25] However, in use, reflection loss of the excitation light leads to a lower luminous efficacy than commercial white LEDs.

Yttrium aluminum garnet (YAG) single crystals have long been studied for their use as scintillators[138] and as laser materials,[139] including the first demonstration of Nd:YAG solid-state lasers at Bell Laboratories in 1964.[140] Although optical studies of undoped and Ce-doped YAG single crystals have been studied previously,[141, 142] it was not until 2013 that high quality,

Czochralski-grown single crystals of Ce:YAG were explored extensively as a yellow phosphor in LED packages.[24] Benefits of single crystals for LED or LD use include a resin free phosphor with observed high stability at elevated temperatures and light flux. Additionally, the YAG lattice is very rigid, resulting in a high quantum efficiency,[4] and substitutions of Gd and Lu result in color tuning of the emission, making this phosphor tunable.[19] Optically transmissive single crystals were only obtained using low Ce-doping levels with any doping amount greater than 0.5 at% resulting in polycrystalline boules. This is different from polycrystalline powders, where the optimized quantum efficiency is observed at 2-3 at% Ce.[19] Thermal conductivity of the single crystal phosphor plate was measured to be 9.2 W/(m·K) at room temperature and 5.6 W/(m·K) at 200 °C, which exceeds the 0.2 W/(m·K) of typical organic resins typically used to encapsulate phosphors.[24] In separate work, the thermal quenching temperature of the crystals was measured using lifetime decay measurements, and a quenching temperature of 632 K was reported,[30], which agrees with previous work on Ce:YAG with very low doping amounts.[5]

Lifetime decay measurements are an accurate means to determine the decay behavior of isolated Ce ions in the YAG system for low ($<$1 %) amounts of Ce doping, as increased doping leads to thermally activated concentration quenching.[5] Thermal stability of a phosphor is often investigated using

temperature dependent emission studies, but the results of which can be misleading due to the strong temperature dependence of the 460 nm absorption band in Ce:YAG,[30] as well as thermally activated broadening of the bands that causes crossover.[5] For this reason, temperature quenching in phosphors is best explored using lifetime decay measurements for very small doping amounts. In the present work, temperature dependent emission and lifetime decay measurements of a Ce:YAG single crystal and single crystal-derived powder both of the same composition are explored and compared to Ce:YAG of higher doping. It is observed that the high thermal quenching temperature is a result of composition and not of high thermal conductivity.

A.2 Methods

A commercially obtained Ce:YAG single crystal with Ce doping of 0.5 at% and a single crystal-derived powder of the same composition obtained by grinding the single crystal, were compared. Average particle size for the powder was 60 μm. To measure the emission and lifetime behavior of the powder, the powder was mixed with silicone resin using the ratio of 25 wt% phosphor in a silicone matrix (Momentive, RTV-615) using a high speed mixing system (FlackTek Inc., DAC 150.1 FVZ-K) at 1500 rpm for 5 min, and subsequently

deposited on a 100 mm^2 fused silica substrate (Chemglass) and heated at 125 °C for 15 min in a box furnace to complete the curing process.

The temperature dependence of the PLQY was measured from 77 K to 503 K in 30 K increments using a home-built fluorometer with a cryostat sample stage for low temperatures and a heating stage for high temperatures. Luminescence lifetime measurements were performed using the Time-Correlated Single Photon Counting (TCSPC) technique.[143] Approximately 200 femtosecond (fs) excitation pulses with wavelength 440 nm were generated by doubling the fundamental frequency of fs – Ti:Sapphire laser (Coherent Mira 900) pulses in a commercial optical harmonic generator (Inrad). The laser pulse rate was reduced to 200 KHz by a home-made acousto-optical pulse picker in order to avoid any saturation effects. The TCSPC system is equipped with an ultrafast micro-channel plate photomultiplier tube detector (Hamamatsu R3809U-51), an electronics board (Becker & Hickl SPC-630), and has an instrument response time of about 60-65 picoseconds. The triggering signal for the TCSPC board was generated by sending a small fraction of the laser beam onto a fast (*i.e.,* 400 MHz bandwidth) Si photo-diode (Thorlabs Inc.). The fluorescence signal was dispersed in a monochromator (Acton Research SPC-500) after passing through a pump blocking, long wavelength-pass, autofluorescence-free, interference filter (Omega Filters, ALP series). The monochromator is equipped

with a CCD camera (Roper Scientific PIXIS-400), allowing for monitoring of the time-averaged fluorescence spectrum. Luminescence transients were not deconvolved with the instrument response function since their characteristic time-constants were much longer than the width of the system response to the excitation pulse.

A.3 Results and discussion

The temperature dependent emission behavior for the single crystal and powder Ce:YAG are shown in Figure A.1. The normalized emission intensity of the single crystal is very stable (Figure A.1(a) and Figure A.1(b)), and two well-resolved emission bands observed at low temperatures for both the single crystal and powder (Figure A.1(c)). Details for the origins of these bands have been explained previously.[30] It is important to note that the intensity is normalized to the largest integral of the emission, which for the single crystal 140 K and 110 K for the ground Ce:YAG powder in silicone. At 503 K, the emission intensity is 92% its maximum value for the single crystal, which agrees well with literature for Ce:YAG with low Ce doping.[5, 30] However, the emission intensity of the ground Ce:YAG powder is 78% its maximum.

As noted in the introduction, emission intensity does not uncover the

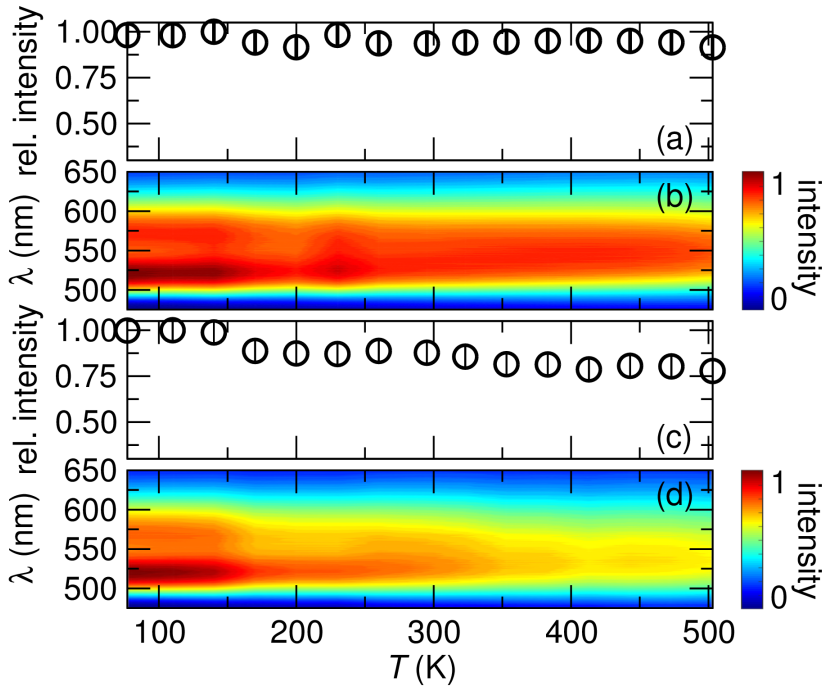

Figure A.1: Normalized intensity (a) and temperature dependent emission intensity (b) for the single crystal shows stable emission across the temperature regime investigated. The integrated area falls slightly (c) for the powder and emission peaks become more broad (d).

intrinsic quenching behavior of the phosphor, as the absorption bands are temperature dependent. Of interest for blue excitation is the absorption band at 460 nm, which decreases with increasing temperature due to a redistribution over different crystal field components of the $^2F_{5/2}$ ground state. This occurs because the transition from second crystal field level of the $^2F_{5/2}$ level to lowest d-level is symmetry forbidden,[144–147] resulting in a lower light output while the quantum efficiency remains constant.[5] Additionally, normalizing to unity for the maximum value will result in a decrease in peak height, which provides misleading results for temperature dependent emission, as the relative intensity, as given by the integral, remains high (Figure A.1(c)) while the emission bands broaden and display a lower peak intensity (Figure A.1(d)). Therefore, lifetime measurements were employed to observe the shortening of luminescence lifetime that is characteristic of additional non radiative contributions to the decay process.[5]

Lifetime curves are shown in Figure A.2. Both the single crystal and the single crystal-derived powder displayed mono exponential behavior and were fit to a single curve, which agrees well with literature for low Ce doping levels.[5] Plotting the natural logarithm of the intensity ratios yields a line with negative slope that is the inverse of the lifetime. From this, lifetime values were extracted and are shown in Figure A.3 as a function of temperature. The lifetime values

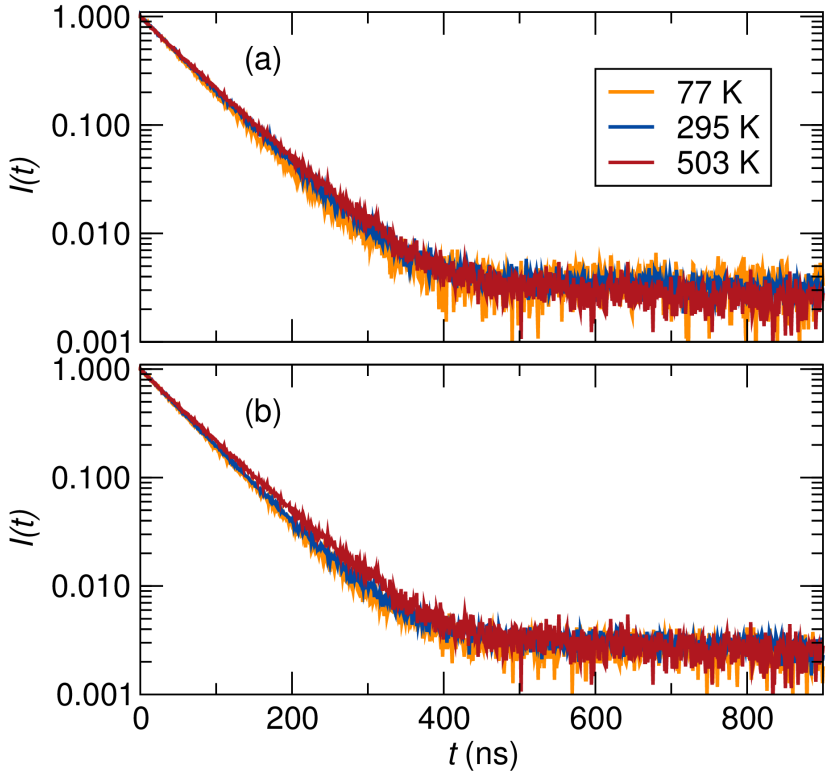

Figure A.2: Photoluminescence lifetime curves for the Ce:YAG single crystal (a) and the Ce:YAG powder (b) show single exponential behavior with little deviation across the temperatures measured.

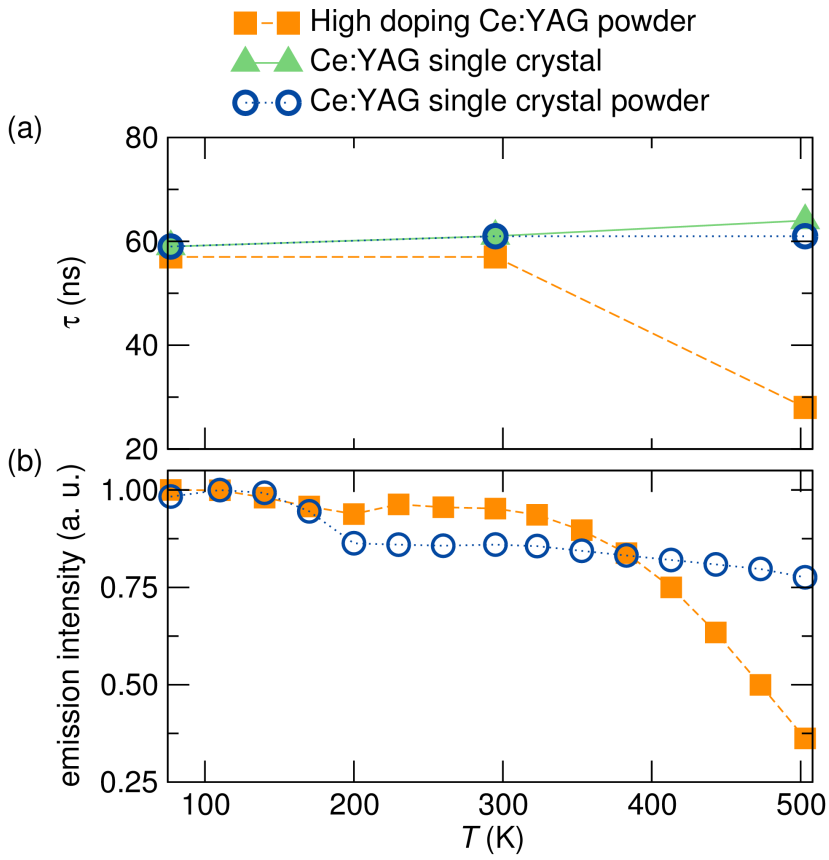

Figure A.3: Phosphor lifetime (a) and integrated emission intensity (b) as a function of temperature for Ce:YAG powders and Ce:YAG single crystal shows similar behavior despite different morphologies.

for the single crystal and the single crystal derived phosphor powder do not differ greatly up to 500 K, confirming previous work on powders and suggesting that Ce concentration in the source of thermal quenching in single crystals.[5]

The results of the present study confirm previous observations for ceramic Ce:YAG powders with low Ce doping.[5] In recent work on Ce:YAG single crystals, the decay of the quantum efficiency as a function of temperature for the ceramic powder was investigated as a comparison, and could not be fit using a single exponential. This was attributed to additional non-radiative recombination paths inherent to ceramic phosphor powders and not to single crystals.[30] For reasons explained presently, lifetime measurements, and not quantum efficiency or normalized intensity, should be used to investigate the thermal quenching of a phosphor as it provides the most insight into the inherent quenching behavior of isolated Ce ions.[5] It is seen through lifetime measurements in the present work that low doping in powders derived from single crystals show almost identical behavior to single crystals. The origins of these observations will now be discussed.

Previous work on single crystal Ce:YAG observed constant lifetime values up to room temperature, which was attributed to radiative recombination as the dominant mechanism.[30] This is followed by a slight increase in PLLT values up to 523 K and a precipitous drop at higher temperatures. The slight

increase was observed for Ce:YAG powders and was attributed to reabsorption from spectral overlap in Ce:YAG, with the increase in spectral overlap with increasing temperature describing the slight increase in lifetime observed in the present work for both the single crystal and the phosphor powder.[5] The quenching temperature for the single crystal was determined in previous work to be 632 K,[30] which is lower than that determined for a powder of lower Ce doping (0.033%).[5] Therefore, low doping leads to high thermal quenching, regardless of single crystal or powder in silicone, and needs to be considered for designing devices. Thin single crystal plates were observed to have high conversion efficiencies,[30] which is at first unexpected as there is a lower absorption strength for the lower Ce amounts. A longer optical pathway of the plate would compensate the loss. It has been suggested that ceramic powder phosphors possess defects that lead to non-radiative losses, the effects of which speculated to increase in temperature.[30] The results of the present study add some confusion to this understanding, suggesting that ceramic powder phosphors have nearly identical thermal quenching behavior up to 503 K.

As noted, reabsorption of the emission can occur for higher doping concentrations, which will affect both the emission intensity and lifetime as a function of temperature. Therefore, investigating low Ce concentrations ($<$0.1 at%) ensures that interacting between the Ce^{3+} ions and reabsorption

are negligible.[5] For example, a Ce concentration of only 1% results in a quenching temperature of 480 K due to thermally activated temperature quenching. Therefore, the improved thermal stability of the single crystal relies first on its very low doping amount, as both the Ce:YAG single crystal and Ce:YAG powder of 0.05% Ce display the same thermal quenching behavior as determined by the decay lifetime. Then, the high thermal conductivity over silicone offers good heat mitigation during excitation. Shown in the present thesis, ceramic phosphor composites with thermal conductivities superior to single crystals can be made. In other work, quantum yield was observed to increase with decreasing doping, which may explain the high quantum yield observed in Ce:YAG single crystals.[5] For designing a device with Ce:YAG, the thermal conductivity and the quantum yield must be considered, as a lower QY will result in more self heating, and self heating will be effectively mitigated with high thermal conductivity.

In conclusion, the results demonstrate the discrepancy between temperature dependent emission and lifetime measurements. In the present study, the quenching temperature of the Ce:YAG is observed to be a result of low doping regardless of whether it is in single crystal or powder in silicone form. The phosphor in silicone and single crystal differ in thermal conductivity by two orders of magnitude, but display nearly identical behavior. In the future of

high power LED and LD-based lighting sources, it will be important to explore the role of quenching temperature, as well as the potential complex interplay between the ability to dissipate heat and the thermal quenching temperature, QY, sample size, and heat sinking strategies.

Bibliography

[1] R. E. Hummel, *Electronic properties of materials*. Springer-Verlag New York, 4th ed., 2011.

[2] N. C. George, K. A. Denault, and R. Seshadri, "Phosphors for solid-state white lighting," *Annual Review of Materials Research*, vol. 43, no. 1, pp. 481–501, 2013.

[3] S. Shionoya and W. Yen, *Phosphor handbook*. CRC press, 1998.

[4] J. Brgoch, S. P. DenBaars, and R. Seshadri, "Proxies from Ab initio calculations for screening efficient Ce^{3+} phosphor hosts," *The Journal of Physical Chemistry C*, vol. 117, no. 35, pp. 17955–17959, 2013.

[5] V. Bachmann, C. Ronda, and A. Meijerink, "Temperature quenching of yellow Ce^{3+} luminescence in YAG:Ce," *Chemistry of Materials*, vol. 21, no. 10, pp. 2077–2084, 2009.

[6] E. F. Schubert, *Light Emitting Diodes*. Wiley Online Library, 2006.

[7] A. Zukauskas, M. S. Shur, and R. Gaska, *Introduction to Solid-State Lighting*. J. Wiley, 2002.

[8] Y. Ohno, "Practical use and calculation of CCT and Duv," *LEUKOS*, vol. 10, no. 1, pp. 47–55, 2014.

[9] M. Cantore, N. Pfaff, R. M. Farrell, J. S. Speck, S. Nakamura, and S. P. DenBaars, "High luminous flux from single crystal phosphor-converted laser-based white lighting system," *Optics Express*, vol. 24, no. 2, pp. A215–A221, 2016.

[10] J. R. Brodrick, "Energy Savings Forecast of Solid-State Lighting in General Illumination Applications," *US Department of Energy, Washington, DC*, 2014.

[11] S. Nakamura and M. R. Krames, "History of gallium–nitride-based light-emitting diodes for illumination," *Proceedings of the IEEE*, vol. 101, no. 10, pp. 2211–2220, 2013.

[12] L. Y. Kuritzky and J. S. Speck, "Lighting for the 21st century with laser diodes based on non-basal plane orientations of GaN," *MRS Communications*, vol. 5, no. 03, pp. 463–473, 2015.

[13] J. J. Wierer, J. Y. Tsao, and D. S. Sizov, "Comparison between blue lasers and light-emitting diodes for future solid-state lighting," *Laser & Photonics Reviews*, vol. 7, no. 6, pp. 963–993, 2013.

[14] S. Nakamura, M. Senoh, S.-I. Nagahama, N. Iwasa, T. Yamada, T. Matsushita, H. Kiyoku, and Y. Sugimoto, "InGaN-based multi-quantum-well-structure laser diodes," *Japanese Journal of Applied Physics*, vol. 35, no. 1B, p. L74, 1996.

[15] J. W. Raring, M. C. Schmidt, C. Poblenz, Y.-C. Chang, M. J. Mondry, B. Li, J. Iveland, B. Walters, M. R. Krames, R. Craig, R. Paul, J. S. Speck, S. P. DenBaars, and S. Nakamura, "High-efficiency blue and true-green-emitting laser diodes based on non-*c*-plane oriented GaN substrates," *Applied Physics Express*, vol. 3, no. 11, p. 112101, 2010.

[16] Y.-D. Lin, S. Yamamoto, C.-Y. Huang, C.-L. Hsiung, F. Wu, K. Fujito, H. Ohta, J. S. Speck, S. P. DenBaars, and S. Nakamura, "High quality InGaN/AlGaN multiple quantum wells for semipolar InGaN green laser diodes," *Applied Physics Express*, vol. 3, no. 8, p. 082001, 2010.

[17] C. Holder, J. S. Speck, S. P. DenBaars, S. Nakamura, and D. Feezell, "Demonstration of nonpolar GaN-based vertical-cavity surface-emitting lasers," *Applied Physics Express*, vol. 5, no. 9, p. 092104, 2012.

[18] J. Sheu, S. Chang, C. Kuo, Y. Su, L. Wu, Y. Lin, W. Lai, J. Tsai, G. Chi, and R. Wu, "White-light emission from near UV InGaN-GaN LED chip

precoated with blue/green/red phosphors," *IEEE Photonics Technology Letters*, vol. 15, pp. 18–20, Jan 2003.

[19] A. Birkel, K. A. Denault, N. C. George, C. E. Doll, B. Hery, A. A. Mikhailovsky, C. S. Birkel, B.-C. Hong, and R. Seshadri, "Rapid microwave preparation of highly efficient Ce^{3+}-substituted garnet phosphors for solid state white lighting," *Chemistry of Materials*, vol. 24, no. 6, pp. 1198–1204, 2012.

[20] K. R. Long, B. S. Van Gosen, N. K. Foley, and D. Cordier, "The principal rare earth elements deposits of the United States: a summary of domestic deposits and a global perspective," in *Non-Renewable Resource Issues*, pp. 131–155, Springer, 2012.

[21] K. A. Denault, M. Cantore, S. Nakamura, S. P. DenBaars, and R. Seshadri, "Efficient and stable laser-driven white lighting," *AIP Advances*, vol. 3, no. 7, p. 072107, 2013.

[22] Q.-Q. Zhu, X.-J. Wang, L. Wang, N. Hirosaki, T. Nishimura, Z.-F. Tian, Q. Li, Y.-Z. Xu, X. Xu, and R.-J. Xie, "β-Sialon:Eu phosphor-in-glass: a robust green color converter for high power blue laser lighting," *Journal of Materials Chemistry C*, vol. 3, pp. 10761–10766, 2015.

[23] X. Luo, X. Fu, F. Chen, and H. Zheng, "Phosphor self-heating in phosphor converted light emitting diode packaging," *International Journal of Heat and Mass Transfer*, vol. 58, no. 1, pp. 276–281, 2013.

[24] A. Latynina, M. Watanabe, D. Inomata, K. Aoki, Y. Sugahara, E. G. Villora, and K. Shimamura, "Properties of Czochralski grown Ce,Gd:$Y_3Al_5O_{12}$ single crystal for white light-emitting diode," *Journal of Alloys and Compounds*, vol. 553, pp. 89–92, 2013.

[25] S. Fujita, S. Yoshihara, A. Sakamoto, S. Yamamoto, and S. Tanabe, "YAG Glass-Ceramic Phosphor for White LED (I): Background and Development," in *Optics and Photonics 2005*, vol. 5941, pp. 594111–594117, 2005.

[26] S. Tanabe, S. Fujita, S. Yoshihara, A. Sakamoto, and S. Yamamoto, "YAG glass-ceramic phosphor for white LED (II): luminescence characteristics," in *Optics & Photonics 2005*, p. 594112, 2005.

[27] R. Murota, T. Kobayashi, and Y. Mita, "Solid state light source fabricated with YAG:Ce single crystal," *Japanese Journal of Applied Physics*, vol. 41, no. 8A, p. L887, 2002.

[28] A. Hanafi, H. Erdl, and S. Weber, "New efficient, compact vehicular lighting system using high-power semiconductor laser diodes," in *DOE Solid-State Lighting R&D Workshop*, 2014.

[29] S. Arjoca, E. G. Víllora, D. Inomata, K. Aoki, Y. Sugahara, and K. Shimamura, "Ce:$(Y_{1-x}Lu_x)Al_5O_{12}$ single-crystal phosphor plates for high-brightness white LEDs/LDs with high-color rendering (R_a>90) and temperature stability," *Materials Research Express*, vol. 1, no. 2, p. 25041, 2014.

[30] S. Arjoca, E. G. Víllora, D. Inomata, K. Aoki, Y. Sugahara, and K. Shimamura, "Temperature dependence of Ce:YAG single-crystal phosphors for high-brightness white LEDs/LDs," *Materials Research Express*, vol. 2, no. 5, p. 055503, 2015.

[31] M. Raukas, J. Kelso, Y. Zheng, K. Bergenek, D. Eisert, A. Linkov, and F. Jermann, "Ceramic phosphors for light conversion in LEDs," *ECS Journal of Solid State Science and Technology*, vol. 2, no. 2, pp. R3168–R3176, 2013.

[32] C. Basu, M. Meinhardt-Wollweber, and B. Roth, "Lighting with laser diodes," *Advances in Optical Technologies*, vol. 2, no. 4, pp. 313–321, 2013.

[33] R. Mueller-Mach, G. O. Mueller, and M. R. Krames, "Phosphor-converted high power LEDs," in *Manufacturing LEDs for Lighting and Display*, vol. 6797, p. 67970G, International Society for Optics and Photonics, 2007.

[34] G. Mueller, R. Mueller-Mach, M. R. Krames, P. Schmidt, H. Bechtel, M. J, J. de Grraf, and T. Kop, "Luminescent ceramic for a light emitting device," Tech. Rep. US20050269582 A1, 2005.

[35] H. Bechtel, P. Schmidt, W. Busselt, and B. S. Schreinemacher, "Lumiramic: A new phosphor technology for high performance solid state light sources," in *Optical Engineering + Applications*, p. 70580E, International Society for Optics and Photonics, 2008.

[36] H. Bechtel, P. Schmidt, A. Tücks, M. Heidemann, D. Chamberlin, R. Müller-Mach, G. O. Müller, and O. Shchekin, "Fully phosphor-converted LEDs with Lumiramic phosphor technology," in *SPIE Optical Engineering + Applications*, p. 77840W, International Society for Optics and Photonics, 2010.

[37] S.-I. Sakata, A. Mitani, and I. Fujii, "Light conversion structure and light-emitting device using the same," Tech. Rep. US 8044572 B2, US 8044572 B2, 2011.

[38] Y. Tang, S. Zhou, C. Chen, X. Yi, Y. Feng, H. Lin, and S. Zhang, "Composite phase ceramic phosphor of Al_2O_3-Ce:YAG for high efficiency light emitting," *Optics Express*, vol. 23, no. 14, pp. 17923–17928, 2015.

[39] R. G. Munro, "Evaluated material properties for a sintered alpha-alumina," *Journal of the American Ceramic Society*, vol. 80, no. 8, pp. 1919–1928, 1997.

[40] S. Li, Q. Zhu, D. Tang, X. Liu, G. Ouyang, L. Cao, N. Hirosaki, T. Nishimura, Z. Huang, and R.-J. Xie, "Al_2O_3–YAG:Ce composite phosphor ceramic: a thermally robust and efficient color converter for solid state laser lighting," *Journal of Materials Chemistry C*, vol. 4, pp. 8648–8654, 2016.

[41] C. Cozzan, K. J. Griffith, G. Laurita, J. G. Hu, C. P. Grey, and R. Seshadri, "Structural evolution and atom clustering in β-SiAlON:β-$Si_{6-z}Al_zO_zN_{8-z}$," *Inorganic Chemistry*, vol. 56, pp. 2153–2158, 2017.

[42] G. Cao and R. Metselaar, "α'-Sialon ceramics: a review," *Chemistry of Materials*, vol. 3, no. 2, pp. 242–252, 1991.

[43] J. P. Attfield, "Principles and applications of anion order in solid oxynitrides," *Crystal Growth & Design*, vol. 13, no. 10, pp. 4623–4629, 2013.

[44] N. Butler, R. Dupree, and M. H. Lewis, "The use of magic-angle-spinning NMR in structural studies of Si-Al-ON phases," *Journal of Materials Science Letters*, vol. 3, no. 5, pp. 469–470, 1984.

[45] J. Sjöberg, R. K. Harris, and D. C. Apperley, "^{29}Si, ^{27}Al and ^{15}N magic angle spinning nuclear magnetic resonance study of O'-Sialons and some related phases," *Journal of Materials Chemistry*, vol. 2, no. 4, pp. 433–438, 1992.

[46] R. Dupree, M. Lewis, G. Leng-Ward, and D. Williams, "Co-ordination of Si atoms in silicon-oxynitrides determined by magic-angle-spinning NMR," *Journal of Materials Science Letters*, vol. 4, no. 4, pp. 393–395, 1985.

[47] M. E. Smith, "Observation of mixed aluminum oxynitride (Al(O, N)$_4$) structural units by aluminum-27 magic angle spinning NMR," *Journal of Physical Chemistry*, vol. 96, no. 3, pp. 1444–1448, 1992.

[48] V. L. Vinograd, E. A. Juarez-Arellano, A. Lieb, K. Knorr, W. Schnick, J. D. Gale, and B. Winkler, "Coupled Al/Si and O/N order/disorder in BaYb[$Si_{4-x}Al_xO_xN_{7-x}$] sialon: neutron powder diffraction and Monte Carlo simulations," *Zeitschrift für Kristallographie*, vol. 222, no. 8, pp. 402–415, 2007.

[49] R. Dupree, M. H. Lewis, and M. Smith, "Structural characterization of ceramic phases with high-resolution ^{27}Al NMR," *Journal of Applied Crystallography*, vol. 21, no. 2, pp. 109–116, 1988.

[50] J. Klinowski, J. Thomas, D. Thompson, P. Korgul, K. Jack, C. Fyfe, and G. Gobbi, "Structural studies of sialon ceramics by high-resolution solid-state NMR," *Polyhedron*, vol. 3, no. 11, pp. 1267–1269, 1984.

[51] K. Tatsumi, T. Mizoguchi, S. Yoshioka, T. Yamamoto, T. Suga, T. Sekine, and I. Tanaka, "Distribution of solute atoms in β-and spinel $Si_{6-z}Al_zO_zN_{8-z}$ by Al K-edge X-ray absorption near-edge structure," *Physical Review B*, vol. 71, no. 3, p. 033202, 2005.

[52] J. Brgoch, M. W. Gaultois, M. Balasubramanian, K. Page, B.-C. Hong, and R. Seshadri, "Local structure and structural rigidity of the green phosphor β-SiAlON:Eu^{2+}," *Applied Physics Letters*, vol. 105, p. 181904, 2014.

[53] E. Lippmaa, M. Mägi, A. Samoson, M. Tarmak, and G. Engelhardt, "Investigation of the structure of zeolites by solid-state high-resolution silicon-29 NMR spectroscopy," *Journal of the American Chemical Society*, vol. 103, no. 17, pp. 4992–4996, 1981.

[54] N. C. George, A. J. Pell, G. Dantelle, K. Page, A. Llobet, M. Balasubramanian, G. Pintacuda, B. F. Chmelka, and R. Seshadri, "Local environments of dilute activator ions in the solid-state lighting phosphor $Y_{3-x}Ce_xAl_5O_{12}$," *Chemistry of Materials*, vol. 25, no. 20, pp. 3979–3995, 2013.

[55] J. K. Furdyna, "Diluted magnetic semiconductors," *Journal of Applied Physics*, vol. 64, no. 4, pp. R29–R64, 1988.

[56] K. F. Hsu, S. Loo, F. Guo, W. Chen, J. S. Dyck, C. Uher, T. Hogan, E. Polychroniadis, and M. G. Kanatzidis, "Cubic $AgPb_mSbTe_{2+m}$: bulk thermoelectric materials with high figure of merit," *Science*, vol. 303, no. 5659, pp. 818–821, 2004.

[57] A. C. Larson and R. B. Von Dreele, "GSAS," *General Structure Analysis System. LANSCE, MS-H805, Los Alamos, New Mexico*, 1994.

[58] B. H. Toby, "EXPGUI, a Graphical User Interface for GSAS," *Journal of Applied Crystallography*, vol. 34, no. 2, pp. 210–213, 2001.

[59] K. Momma and F. Izumi, "VESTA :a three-dimensional visualization system for electronic and structural analysis," *Journal of Applied Crystallography*, vol. 41, no. 3, pp. 653–658, 2008.

[60] S. J. Clark, M. D. Segall, C. J. Pickard, P. J. Hasnip, M. I. Probert, K. Refson, and M. C. Payne, "First principles methods using CASTEP," *Zeitschrift für Kristallographie*, vol. 220, no. 5/6, pp. 567–570, 2005.

[61] C. J. Pickard and F. Mauri, "All-electron magnetic response with pseudopotentials: NMR chemical shifts," *Physical Review B*, vol. 63, no. 24, p. 245101, 2001.

[62] J. R. Yates, C. J. Pickard, and F. Mauri, "Calculation of NMR chemical shifts for extended systems using ultrasoft pseudopotentials," *Physical Review B*, vol. 76, no. 2, p. 024401, 2007.

[63] M. Profeta, F. Mauri, and C. J. Pickard, "Accurate first principles prediction of ^{17}O NMR parameters in SiO_2: assignment of the zeolite ferrierite spectrum," *Journal of the American Chemical Society*, vol. 125, no. 2, pp. 541–548, 2003.

[64] J. P. Perdew, K. Burke, and M. Ernzerhof, "Generalized gradient approximation made simple," *Physical Review Letters*, vol. 77, no. 18, p. 3865, 1996.

[65] H. J. Monkhorst and J. D. Pack, "Special points for Brillouin-zone integrations," *Physical Review B*, vol. 13, no. 12, p. 5188, 1976.

[66] M. Bak, J. T. Rasmussen, and N. C. Nielsen, "SIMPSON: a general simulation program for solid-state NMR spectroscopy," *Journal of Magnetic Resonance*, vol. 147, no. 2, pp. 296–330, 2000.

[67] X. Zhu, Y. Masubuchi, T. Motohashi, and S. Kikkawa, "The z value dependence of photoluminescence in Eu^{2+}-doped β-SiAlON ($Si_{6-z}Al_zO_zN_{8-z}$) with $1 \leq z \leq 4$," *Journal of Alloys and Compounds*, vol. 489, no. 1, pp. 157–161, 2010.

[68] T. Takeda, R.-J. Xie, and N. Hirosaki, "Local structure analysis in nitride and oxynitride phosphors," *ECS Journal of Solid State Science and Technology*, vol. 2, no. 2, pp. R3132–R3137, 2013.

[69] K. A. Denault, J. Brgoch, S. D. Kloß, Simon D., M. W. Gaultois, J. Siewenie, K. Page, and R. Seshadri, "Average and Local Structure,

Debye Temperature, and Structural Rigidity in Some Oxide Compounds Related to Phosphor Hosts," *ACS Applied Materials & Interfaces*, vol. 7, no. 13, pp. 7264–7272, 2015.

[70] R. Shannon, "Effective ionic radii in oxides and fluorides," *Acta Crystallogr. B.*, vol. 25, pp. 925–946, 1969.

[71] C. Cozzan, G. Laurita, M. W. Gaultois, M. Cohen, A. A. Mikhailovsky, M. Balasubramanian, and R. Seshadri, "Understanding the links between composition, polyhedral distortion, and luminescence properties in green-emitting β-$Si_{6-z}Al_zO_zN_{8-z}$:Eu^{2+} phosphors," *Journal of Materials Chemistry C*, vol. 5, no. 38, pp. 10039–10046, 2017.

[72] S. Nakamura, T. Mukai, and M. Senoh, "Candela-class high-brightness InGaN/AlGaN double-heterostructure blue-light-emitting diodes," *Applied Physics Letters*, vol. 64, no. 13, pp. 1687–1689, 1994.

[73] S. Pimputkar, J. S. Speck, S. P. DenBaars, and S. Nakamura, "Prospects for LED lighting," *Nature Photonics*, vol. 3, no. 4, pp. 180–182, 2009.

[74] N. Hirosaki, R.-J. Xie, K. Kimoto, T. Sekiguchi, Y. Yamamoto, T. Suehiro, and M. Mitomo, "Characterization and properties of green-emitting β-SiAlON:Eu^{2+} powder phosphors for white light-emitting diodes," *Applied Physics Letters*, vol. 86, p. 211905, 2005.

[75] W. B. Im, N. N. Fellows, S. P. DenBaars, and R. Seshadri, "$La_{1-x-0.025}Ce_{0.025}Sr_{2+x}Al_{1-x}Si_xO_5$ solid solutions as tunable yellow phosphors for solid state white lighting," *Journal of Materials Chemistry*, vol. 19, no. 9, pp. 1325–1330, 2009.

[76] K. A. Denault, N. C. George, S. R. Paden, S. Brinkley, A. A. Mikhailovsky, J. Neuefeind, S. P. DenBaars, and R. Seshadri, "A green-yellow emitting oxyfluoride solid solution phosphor $Sr_2Ba(AlO_4F)_{1-x}(SiO_5)_x$:$Ce^{3+}$ for thermally stable, high color rendition solid state white lighting," *Journal of Materials Chemistry*, vol. 22, no. 35, pp. 18204–18213, 2012.

[77] A. P. Black, K. A. Denault, C. Frontera, R. Seshadri, A. R. Goñi, and A. Fuertes, "Emission colour tuning through coupled N/La introduction

in Sr_2SiO_4:Eu^{2+}," *Journal of Materials Chemistry C*, vol. 3, no. 43, pp. 11471–11477, 2015.

[78] K. Kimoto, R.-J. Xie, Y. Matsui, K. Ishizuka, and N. Hirosaki, "Direct observation of single dopant atom in light-emitting phosphor of β-SiAlON:Eu^{2+}," *Applied Physics Letters*, vol. 94, no. 4, p. 041908, 2009.

[79] Z. Wang, W. Ye, I.-H. Chu, and S. P. Ong, "Elucidating structure–composition–property relationships of the β-SiAlON: Eu^{2+} phosphor," *Chemistry of Materials*, vol. 28, pp. 8622–8630, 2016.

[80] T. Nakayasu and T. Yamada, "Local chemical bonding around rare-earth ions in α- and β-Si_3N_4," *Journal of the American Ceramic Society*, vol. 80, no. 10, pp. 2525–2532, 1997.

[81] W. H. Baur, "The geometry of polyhedral distortions. predictive relationships for the phosphate group," *Acta Crystallographica*, vol. B30, pp. 1195–1215, 1974.

[82] B. Ravel and M. Newville, "ATHENA, ARTEMIS, HEPHAESTUS: Data analysis for X-ray absorption spectroscopy using IFEFFIT," *Journal of Synchrotron Radiation*, vol. 12, no. 4, pp. 537–541, 2005.

[83] J. C. de Mello, H. F. Wittmann, and R. H. Friend, "An improved experimental determination of external photoluminescence quantum efficiency," *Advanced Materials*, vol. 9, no. 3, pp. 230–232, 1997.

[84] I. D. Brown, "Recent developments in the methods and applications of the bond valence model," *Chemical Reviews*, vol. 109, pp. 6858–6919, 2009.

[85] X. Zhang, M.-H. Fang, Y.-T. Tsai, A. Lazarowska, S. Mahlik, T. Lesniewski, M. Grinberg, W. K. Pang, F. Pan, C. Liang, W. Zhou, J. Wang, J.-F. Lee, B.-M. Cheng, T.-L. Hung, Y.-Y. Chen, and R.-S. Liu, "Controlling of structural ordering and rigidity of β-SiAlON:Eu through chemical cosubstitution to approach narrow-band-emission for light-emitting diodes application," *Chemistry of Materials*, vol. 29, no. 16, pp. 6781–6792, 2017.

[86] H. Höppe, H. Lutz, P. Morys, W. Schnick, and A. Seilmeier, "Luminescence in Eu^{2+}-doped $Ba_2Si_5N_8$: fluorescence, thermoluminescence, and upconversion," *Journal of Physics and Chemistry of Solids*, vol. 61, no. 12, pp. 2001–2006, 2000.

[87] J. Van Krevel, J. Van Rutten, H. Mandal, H. Hintzen, and R. Metselaar, "Luminescence properties of terbium-, cerium-, or europium-doped α-sialon materials," *Journal of Solid State Chemistry*, vol. 165, no. 1, pp. 19–24, 2002.

[88] R.-J. Xie, M. Mitomo, K. Uheda, F.-F. Xu, and Y. Akimune, "Preparation and luminescence spectra of calcium-and rare-earth (R= Eu, Tb, and Pr)-codoped α-SiAlON ceramics," *Journal of the American Ceramic Society*, vol. 85, no. 5, pp. 1229–1234, 2002.

[89] J. L. Wu, G. Gundiah, and A. Cheetham, "Structure–property correlations in Ce-doped garnet phosphors for use in solid state lighting," *Chemical Physics Letters*, vol. 441, no. 4–6, pp. 250–254, 2007.

[90] P. Dorenbos, "Crystal field splitting of lanthanide $4f^{n-1}$ $5d$-levels in inorganic compounds," *Journal of Alloys and Compounds*, vol. 341, no. 1, pp. 156–159, 2002.

[91] R.-J. Xie, N. Hirosaki, H.-L. Li, Y. Q. Li, and M. Mitomo, "Synthesis and photoluminescence properties of β-Sialon:Eu^{2+} ($Si_{6-z}Al_zO_zN_{8-z}$): A promising green oxynitride phosphor for white light-emitting diodes," *Journal of the Electrochemical Society*, vol. 154, no. 10, pp. J314–J319, 2007.

[92] P. Dorenbos, "Thermal quenching of Eu^{2+} $5d$–$4f$ luminescence in inorganic compounds," *Journal of Physics: Condensed Matter*, vol. 17, no. 50, p. 8103, 2005.

[93] K. Takahashi, K.-I. Yoshimura, M. Harada, Y. Tomomura, T. Takeda, R.-J. Xie, and N. Hirosaki, "On the origin of fine structure in the photoluminescence spectra of the β-Sialon:Eu^{2+} green phosphor," *Science and Technology of Advanced Materials*, vol. 13, no. 1, p. 015004, 2012.

[94] J. H. Ryu, Y.-G. Park, H. S. Won, S. H. Kim, H. Suzuki, J. M. Lee, C. Yoon, M. Nazarov, and B. Tsukerblat, "Luminescent properties of Ca-α-SiAlON:Eu^{2+} phosphors synthesized by gas-pressured sintering," *Journal of the Electrochemical Society*, vol. 155, no. 4, pp. J99–J104, 2007.

[95] J. Ueda, P. Dorenbos, A. J. Bos, A. Meijerink, and S. Tanabe, "Insight into the thermal quenching mechanism for $Y_3Al_5O_{12}$:Ce^{3+} through thermoluminescence excitation spectroscopy," *Journal of Physical Chemistry C*, vol. 119, no. 44, pp. 25003–25008, 2015.

[96] C. Cozzan, M. J. Brady, N. O'Dea, E. E. Levin, S. Nakamura, S. P. DenBaars, and R. Seshadri, "Monolithic translucent $BaMgAl_{10}O_{17}$:Eu^{2+} phosphors for laser-driven solid state lighting," *AIP Advances*, vol. 6, no. 10, p. 105005, 2016.

[97] C. Lee, C. Zhang, M. Cantore, R. M. Farrell, S. H. Oh, T. Margalith, J. S. Speck, S. Nakamura, J. E. Bowers, and S. P. DenBaars, "4 Gbps direct modulation of 450 nm GaN laser for high-speed visible light communication," *Optics Express*, vol. 23, no. 12, pp. 16232–16237, 2015.

[98] C. Lee, C. Shen, H. M. Oubei, M. Cantore, B. Janjua, T. K. Ng, R. M. Farrell, M. M. El-Desouki, J. S. Speck, S. Nakamura, B. S. Ooi, and S. P. DenBaars, "2 Gbit/s data transmission from an unfiltered laser-based phosphor-converted white lighting communication system," *Optics Express*, vol. 23, no. 23, pp. 29779–29787, 2015.

[99] J. E. Garay, "Current-activated, pressure-assisted densification of materials," *Annual Review of Materials Research*, vol. 40, pp. 445–468, 2010.

[100] R. Chaim, R. Marder-Jaeckel, and J. Z. Shen, "Transparent YAG Ceramics by Surface Softening of Nanoparticles in Spark Plasma Sintering," *Materials Science and Engineering: A*, vol. 429, no. 1-2, pp. 74–78, 2006.

[101] R. Chaim, M. Kalina, and J. Z. Shen, "Transparent yttrium Aluminum Garnet (YAG) Ceramics by Spark Plasma Sintering," *Journal of the European Ceramic Society*, vol. 27, no. 11, pp. 3331–3337, 2007.

[102] N. Frage, S. Kalabukhov, N. Sverdlov, V. Ezersky, and M. P. Dariel, "Densification of Transparent Yttrium Aluminum Garnet (YAG) by SPS Processing," *Journal of the European Ceramic Society*, vol. 30, no. 16, pp. 3331–3337, 2010.

[103] R. T. Marta Suárez, Adolfo Fernández and J. L. Menendez, *Sintering to Transparency of Polycrystalline Ceramic Materials*. InTech Open Access Publisher, 2012.

[104] Y.-I. Kim, K.-B. Kim, M.-J. Jung, and J.-S. Hong, "Combined Rietveld refinement of $BaMgAl_{10}O_{17}:Eu^{2+}$ using X-ray and neutron powder diffraction data," *Journal of Luminescence*, vol. 99, no. 2, pp. 91–100, 2002.

[105] K.-B. Kim, Y.-I. Kim, H.-G. Chun, T.-Y. Cho, J.-S. Jung, and J.-G. Kang, "Structural and optical properties of $BaMgAl_{10}O_{17}:Eu^{2+}$ phosphor," *Chemistry of Materials*, vol. 14, no. 12, pp. 5045–5052, 2002.

[106] C. Lee, C. Shen, C. Cozzan, R. M. Farrell, J. S. Speck, S. Nakamura, B. S. Ooi, and S. P. DenBaars, "Gigabit-per-second white light-based visible light communication using near-ultraviolet laser diode and red-, green-, and blue-emitting phosphors," *Optics Express*, vol. 25, no. 15, pp. 17480–17487, 2017.

[107] E. Kim, S. Unithrattil, I. S. Sohn, S. J. Kim, W. J. Chung, and W. B. Im, "Facile one-step fabrication of 2-layered and 4-quadrant type phosphor-in-glass plates for white LEDs: an insight into angle dependent luminescence," *Optical Materials Express*, vol. 6, no. 3, pp. 804–814, 2016.

[108] L.-F. He, G.-H. Fan, M.-Y. Lei, Z.-L. Lou, S.-W. Zheng, C. Su, Y. Xiao, Z.-W. Chen, and T. Zhang, "Luminescent properties of new $MgAl_2O_4$/CeYAG transparent ceramics for white LED applications," *Chinese Journal of Luminescence*, vol. 2, p. 3, 2013.

[109] L. Shen, Y. Li, and Q. Huang, "Ultrafast fabrication of solid phosphor based white light emitting diodes: From powder synthesis to devices," *Applied Physics Letters*, vol. 103, p. 121908, 2013.

[110] Q. Sai, Z. Zhao, C. Xia, X. Xu, F. Wu, J. Di, and L. Wang, "Ce-doped Al_2O_3-YAG eutectic and its application for white LEDs," *Optical Materials*, vol. 35, no. 12, pp. 2155–2159, 2013.

[111] M. Yoshimura, S.-I. Sakata, H. Iba, T. Kawano, and K. Hoshikawa, "Vertical bridgman growth of Al_2O_3/YAG:Ce melt growth composite," *Journal of Crystal Growth*, vol. 416, pp. 100–105, 2015.

[112] Y. H. Song, E. K. Ji, B. W. Jeong, M. K. Jung, E. Y. Kim, C. W. Lee, and D. H. Yoon, "Design of laser-driven high-efficiency Al_2O_3/YAG:Ce^{3+} ceramic converter for automotive lighting: Fabrication, luminous emittance, and tunable color space," *Dyes and Pigments*, vol. 139, pp. 688–692, 2017.

[113] S. Leyre, E. Coutino-Gonzalez, J. Joos, J. Ryckaert, Y. Meuret, D. Poelman, P. Smet, G. Durinck, J. Hofkens, G. Deconinck, and P. Hanselaer, "Absolute determination of photoluminescence quantum efficiency using an integrating sphere setup," *Review of Scientific Instruments*, vol. 85, no. 12, p. 123115, 2014.

[114] K. Morita, B.-N. Kim, H. Yoshida, K. Hiraga, and Y. Sakka, "Influence of pre-and post-annealing on discoloration of $MgAl_2O_4$ spinel fabricated by spark-plasma-sintering (SPS)," *Journal of the European Ceramic Society*, vol. 36, no. 12, pp. 2961–2968, 2016.

[115] R. T. K. Baker, R. D. Sherwood, and E. G. Derouane, "Further studies of the nickel/graphite-hydrogen reaction," *Journal of Catalysis*, vol. 75, no. 2, pp. 382–395, 1982.

[116] J. Abell, I. Harris, B. Cockayne, and B. Lent, "An investigation of phase stability in the Y_2O_3-Al_2O_3 system," *Journal of Materials Science*, vol. 9, no. 4, pp. 527–537, 1974.

[117] Q. Sai and C. Xia, "Tunable colorimetric performance of Al_2O_3-YAG:Ce^{3+} eutectic crystal by Ce^{3+} concentration," *Journal of Luminescence*, vol. 186, pp. 68–71, 2017.

[118] H. Shi, J. Chen, J. Huang, Q. Hu, Z. Deng, Y. Cao, and X. Yuan, "Preparation and luminescence properties of YAG:Ce phosphor for white LED application via a vacuum sintering method," *Physica Status Solidi (A)*, vol. 211, no. 7, pp. 1596–1600, 2014.

[119] D. E. Zelmon, D. L. Small, and R. Page, "Refractive-index measurements of undoped yttrium aluminum garnet from .4 to 5.0 μm," *Applied Optics*, vol. 37, no. 21, pp. 4933–4935, 1998.

[120] T. W. Kirchstetter, T. Novakov, and P. V. Hobbs, "Evidence that the spectral dependence of light absorption by aerosols is affected by organic carbon," *Journal of Geophysical Research*, vol. 109, no. D21, 2004.

[121] Y. Chen and T. Bond, "Light absorption by organic carbon from wood combustion," *Atmospheric Chemistry and Physics*, vol. 10, no. 4, pp. 1773–1787, 2010.

[122] J. Chen, H. Lan, Y. Cao, Z. Deng, Z. Liu, F. Tang, and W. Guo, "Application of composite phosphor ceramics by tape-casting in white light-emitting diodes," *Journal of Alloys and Compounds Alloys Compd.*, vol. 709, pp. 267–271, 2017.

[123] J. Francl and W. Kingery, "Thermal conductivity: IX, experimental investigation of effect of porosity on thermal conductivity," *Journal of the American Ceramic Society*, vol. 37, no. 2, pp. 99–107, 1954.

[124] V. Leung, A. Lagendijk, T. Tukker, A. Mosk, W. IJzerman, and W. Vos, "Interplay between multiple scattering, emission, and absorption of light in the phosphor of a white light-emitting diode," *Optics Express*, vol. 22, no. 7, pp. 8190–8204, 2014.

[125] Y. Ma, W. Lan, B. Xie, R. Hu, and X. Luo, "An optical-thermal model for laser-excited remote phosphor with thermal quenching," *International Journal of Heat and Mass Transfer*, vol. 116, pp. 694 – 702, 2018.

[126] Y. Yang, S. Zhuang, and B. Kai, "High brightness laser-driven white emitter for Etendue-limited applications," *Applied Optics*, vol. 56, no. 30, pp. 8321–8325, 2017.

[127] N. Trivellin, M. Yushchenko, M. Buffolo, C. De Santi, M. Meneghini, G. Meneghesso, and E. Zanoni, "Laser-based lighting: experimental analysis and perspectives," *Materials*, vol. 10, no. 10, p. 1166, 2017.

[128] E. Dougherty, "Blues clues: researchers cast a little light on the subject of sleep," *Harvard Medicine Magazine*, 2012.

[129] A. Krasnoshchoka, A. Thorseth, C. Dam-Hansen, D. D. Corell, P. M. Petersen, and O. B. Jensen, "Investigation of saturation effects in ceramic phosphors for laser lighting," *Materials*, vol. 10, no. 12, p. 1407, 2017.

[130] R. Lachmayer, G. Kloppenburg, and A. G. Wolf, "Rapid prototyping of reflectors for vehicle lighting using laser activated remote phosphor," in *Proceedings SPIE 9383, Light-Emitting Diodes: Materials, Devices, and Applications for Solid State Lighting XIX*, vol. 938305, 2015.

[131] P. Pust, V. Weiler, C. Hecht, A. Tücks, A. S. Wochnik, A.-K. Henß, D. Wiechert, C. Scheu, P. J. Schmidt, and W. Schnick, "Narrow-band red-emitting $Sr[LiAl_3N_4]:Eu^{2+}$ as a next-generation LED-phosphor material," *Nature Materials*, vol. 13, no. 9, p. 891, 2014.

[132] Z. Lin, H. Lin, J. Xu, F. Huang, H. Chen, B. Wang, and Y. Wang, "Highly thermal-stable warm w-LED based on Ce:YAG PiG stacked with a red phosphor layer," *Journal of Alloys and Compounds*, vol. 649, pp. 661–665, 2015.

[133] Y. Peng, Y. Mou, X. Guo, X. Xu, H. Li, M. Chen, and X. Luo, "Flexible fabrication of a patterned red phosphor layer on a YAG:Ce^{3+} phosphor-in-glass for high-power WLEDs," *Optical Materials Express*, vol. 8, pp. 605–614, Mar 2018.

[134] Y. C. Shen, G. O. Mueller, S. Watanabe, N. F. Gardner, A. Munkholm, and M. R. Krames, "Auger recombination in InGaN measured by photoluminescence," *Applied Physics Letters*, vol. 91, p. 141101, 2007.

[135] K. T. Delaney, P. Rinke, and C. G. Van de Walle, "Auger recombination rates in nitrides from first principles," *Applied Physics Letters*, vol. 94, p. 191109, 2009.

[136] E. Kioupakis, P. Rinke, K. T. Delaney, and C. G. Van de Walle, "Indirect Auger recombination as a cause of efficiency droop in nitride light-emitting diodes," *Applied Physics Letters*, vol. 98, p. 161107, 2011.

[137] J. Iveland, L. Martinelli, J. Peretti, J. S. Speck, and C. Weisbuch, "Direct measurement of Auger electrons emitted from a semiconductor light-emitting diode under electrical injection: identification of the dominant mechanism for efficiency droop," *Physical Review Letters*, vol. 110, p. 177406, 2013.

[138] R. Autrata, P. Schauer, and J. Kvapil, "A single crystal of YAG-new fast scintillator in SEM," *Journal of Physics E: Scientific Instruments*, vol. 11, no. 7, pp. 707–708, 1978.

[139] C. A. Burrus and J. Stone, "Single-crystal fiber optical devices: a Nd:YAG fiber laser," *Applied Physics Letters*, vol. 26, no. 6, pp. 318–320, 1975.

[140] J. E. Geusic, H. M. Marcos, and L. G. Van Uitert, "Laser oscillations in Nd-doped yttrium aluminum, yttrium gallium and gadolinium garnets," *Applied Physics Letters*, vol. 4, no. 10, pp. 182–184, 1964.

[141] C. M. Wong, S. R. Rotman, and C. Warde, "Optical studies of cerium doped yttrium aluminum garnet single crystals," *Applied Physics Letters*, vol. 44, no. 11, pp. 1038–1040, 1984.

[142] G. Zhao, X. Zeng, J. Xu, Y. Xu, and Y. Zhou, "Characteristics of large-sized Ce: YAG scintillation crystal grown by temperature gradient technique," *Journal of Crystal Growth*, vol. 253, no. 1, pp. 290–296, 2003.

[143] W. Becker, *Advanced time-correlated single photon counting techniques*, vol. 81. Springer, 2005.

[144] D. J. Robbins, "The effects of crystal field and temperature on the photoluminescence excitation efficiency of Ce^{3+} in YAG," *Journal of the Electrochemical Society*, vol. 126, no. 9, pp. 1550–1555, 1979.

[145] D. J. Robbins, B. Cockayne, J. L. Glasper, and B. Lent, "The temperature dependence of rare-earth activated garnet phosphors II. a comparative

study of Ce^{3+}, Eu^{3+}, Tb^{3+}, and Gd^{3+} in $Y_3Al_5O_{12}$," *Journal of the Electrochemical Society*, vol. 126, no. 7, pp. 1221–1228, 1979.

[146] D. J. Robbins, B. Cockayne, J. L. Glasper, and B. Lent, "The temperature dependence of rare-earth activated garnet phosphors I. intensity and lifetime measurements on undoped and Ce-doped," *Journal of the Electrochemical Society*, vol. 126, no. 7, pp. 1213–1220, 1979.

[147] D. J. Robbins, B. Cockayne, B. Lent, and J. L. Glasper, "The relationship between concentration and efficiency in rare earth activated phosphors," *Journal of the Electrochemical Society*, vol. 126, no. 9, pp. 1556–1563, 1979.